

Quarterly Technical Report

Solid State Research

1986:2

Lincoln Laboratory

MASSACHUSETTS INSTITUTE OF TECHNOLOGY

LEXINGTON, MASSACHUSETTS



Prepared under Electronic Systems Division Contract F19628-85-C-0002.

Approved for public release; distribution unlimited.

ADA 180779

The work reported in this document was performed at Lincoln Laboratory, a center for research operated by Massachusetts Institute of Technology, with the support of the Department of the Air Force under Contract F19628-85-C-0002.

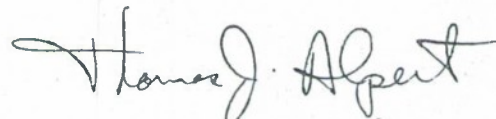
This report may be reproduced to satisfy needs of U.S. Government agencies.

The views and conclusions contained in this document are those of the contractor and should not be interpreted as necessarily representing the official policies, either expressed or implied, of the United States Government.

The ESD Public Affairs Office has reviewed this report, and it is releasable to the National Technical Information Service, where it will be available to the general public, including foreign nationals.

This technical report has been reviewed and is approved for publication.

FOR THE COMMANDER



Thomas J. Alpert, Major, USAF
Chief, ESD Lincoln Laboratory Project Office

Non-Lincoln Recipients

PLEASE DO NOT RETURN

Permission is given to destroy this document
when it is no longer needed.

**MASSACHUSETTS INSTITUTE OF TECHNOLOGY
LINCOLN LABORATORY**

SOLID STATE RESEARCH

QUARTERLY TECHNICAL REPORT

1 FEBRUARY — 30 APRIL 1986

ISSUED 8 SEPTEMBER 1986

Approved for public release; distribution unlimited.

LEXINGTON

MASSACHUSETTS

ABSTRACT

This report covers in detail the solid state research work of the Solid State Division at Lincoln Laboratory for the period 1 February through 30 April 1986. The topics covered are Solid State Device Research, Quantum Electronics, Materials Research, Microelectronics, and Analog Device Technology. Funding is provided primarily by the Air Force, with additional support provided by the Army, DARPA, Navy, SDIO, NASA, and DOE.

TABLE OF CONTENTS

Abstract	iii
List of Illustrations	vii
List of Tables	x
Introduction	xi
Reports on Solid State Research	xv
Organization	xxiii
1. SOLID STATE DEVICE RESEARCH	1
1.1 Intermodulation Distortion in Interferometric Optical Modulators	1
1.2 High-Performance Mass-Transported p-Substrate GaInAsP/InP Buried-Heterostructure Lasers and Their Arrays	4
2. QUANTUM ELECTRONICS	9
2.1 Tuning Characteristics of a Room-Temperature CW Ti:Al ₂ O ₃ Laser	9
2.2 Er:YAG Laser Development	10
2.3 Studies of the Use of LiNbO ₃ in a Lyot Filter System	11
2.4 Spectroscopic Observation of Coupled States in an AlGaAs/GaAs Coupled Double Quantum Well System	13
2.5 Time-Resolved Studies of Photocurrent in a Permeable Base Transistor	17
3. MATERIALS RESEARCH	21
3.1 Flow Visualization Studies for OMVPE Reactor Design	21
3.2 Monolithic GaAs/AlGaAs Diode-Laser/Deflector Devices	26
3.3 Monolithic Integration of GaAs/AlGaAs LEDs and Si MOSFETs	30
3.4 Submicrometer CMOS Devices in Zone-Melting- Recrystallized SOI Films	37
3.5 Residual Infrared Absorption in Ti:Al ₂ O ₃ Crystals	43

4. MICROELECTRONICS	47
4.1 Rapid, Low-Resistance Interconnects by Selective Tungsten Deposition on Laser-Direct-Written Polysilicon	47
4.2 Submicrometer-Gate MESFET with Self-Aligned Ohmic Contacts Using Conventional Lithography	51
4.3 Design of an E-Beam Testable and Restructurable Array Multiplier	55
4.4 Packaging Jig for Whisker-Contacted, Submillimeter-Wave Devices	57
5. ANALOG DEVICE TECHNOLOGY	59
5.1 Superconductive Analog Signal Correlator	59
5.2 Bulk-Acoustic-Wave Holographic-Grating Resonators	62
5.3 Canceler for High-Level Narrowband Interference in a Wideband Channel	65

LIST OF ILLUSTRATIONS

Figure No.		Page
1-1	Analog Optical-Fiber Communication Link Consisting of Constant-Power Optical Source, Interferometric Modulator, Optical Fiber, Detector, and Amplifier	1
1-2	Plot of Fundamental and Intermodulation Product Power Levels as a Function of Electrical Drive Power. Extrapolation to the Intermodulation Intercept Is Shown.	3
1-3	Schematic Drawing of the Transverse Cross-Sectional View of a Mass-Transported p-Substrate GaInAsP/InP Buried-Heterostructure Laser	4
1-4	Light Output vs Current Characteristic of a Mass-Transported p-Substrate GaInAsP/InP BH Laser. The Device Is Mounted Junction Side Down on a Copper Heat Sink.	5
1-5	Threshold Currents and Differential Quantum Efficiencies of Lasers in a Monolithic One-Dimensional Array	6
2-1	Schematic of the Experimental Setup Showing the Ar-Ion Pump Laser and the Three-Mirror Folded Cavity for the Ti:Al ₂ O ₃ Laser	9
2-2	Tuning Characteristics of the Ti:Al ₂ O ₃ Laser. (a) Laser Threshold Power (Incident on the Rod) vs Wavelength. (b) Laser Wavelength(s) for Each Setting of the Lyot Filter, Showing the Two Filter Transmission Branches.	10
2-3	CW Output Power of 1.65-μm Er:YAG Laser as a Function of Input 1.47-μm Laser Pump Power	11
2-4	Lyot Filter Geometry Utilizing the Transverse Electro-Optic Effect	12
2-5	Transmission at 633 nm vs Applied Voltage on the LiNbO ₃ Crystal Using the Configuration Shown in Figure 2-4	13
2-6	Energy Levels of the Lowest Confined Coupled States in the Conduction and Valence Bands of a Symmetric CDQW Structure. For Each Pair of Curves the Higher Energy Level Corresponds to the Antisymmetric State, and the Lower to the Symmetric State. The Labels e, hh, and hl Indicate Electron, Heavy Hole, and Light Hole, Respectively. The Insets Show a Physical Section of the Sample and the Calculated Wavefunctions for the Lowest Electron States in Such Structure. The Energy Levels of the Valence Band Are Inverted.	14

Figure No.		Page
2-7	Luminescence and Excitation Spectra of a Symmetric CDQW at 2 K. (a) and (b) Are Luminescence Spectra at Low Excitation Intensity (<1 W/cm ²) on Log and Linear Scales, Respectively. (c) and (d) Are Excitation Spectra, with Luminescence Monitored at 1528.5 and 1530.5 meV, Respectively, While Excitation Photon Energy Is Varied. Various Structures Are Labeled According to the Scheme Given in Figure 2-6. The Inset Shows Excitation Spectra of Multiple SQWs. Only Two Bound State Peaks, Corresponding to the Heavy- and Light-Hole Excitons, Are Observed.	16
2-8	(a) Schematic of Experimental Setup. (b) PBT Cross Section; the Light Penetrates PBT Through the Window Between the Base and the Collector.	18
2-9	Correlation Signals of Pump and Probe Photocurrents as Detected at the Collector	19
3-1	Schematic Diagram of Apparatus for Gas Flow Visualization	22
3-2	Flow Pattern Obtained for Gas Injection Through a Coaxial Vertical Pipe	23
3-3	Flow Pattern for Gas Injection Through Tangential Inlets	23
3-4	Flow Pattern for Gas Injection Through Tangential Inlets with Disk Rotation of 80 rpm	24
3-5	Flow Pattern for Gas Injection Through a Porous Plug. The Vertical Streaks Are Reflections from the Tube	24
3-6	Flow Pattern for Gas Injection Through Porous Plug for Disk Temperature of 600°C	25
3-7	Procedure for Fabricating Monolithic GaAs/AlGaAs Diode-Laser/Deflector (MLD) Devices	28
3-8	Light Output vs Pulsed Drive Current for (a) Reference Laser with Two Cleaved Facets, (b) Cleaved Facet of MLD Device, (c) Deflector of the Same MLD Device	29
3-9	Intensity of Near-Field Emission Normal to the Surface of a Sample Containing Five MLD Devices	30
3-10	Schematic Cross-Sectional Diagram of a Monolithically Integrated Si MOSFET and GaAs/AlGaAs LED. (The Portion of the MOSFET to the Right of the LED Is Not Shown.)	32
3-11	Optical Micrograph of a GaAs/AlGaAs LED and the Surrounding Si MOSFET	33

Figure No.		Page
3-12	Light Output vs Current Characteristic of an MGS LED	34
3-13	Modulation Characteristics of an MGS LED at (a) 5 MHz and (b) 10 MHz. The Bottom, Middle, and Top Traces Are the Waveforms of the Gate Voltage, Current, and Light Output, Respectively.	35
3-14	Current-Voltage Characteristics of (a) n-Channel Device with $L_{\text{eff}} = 0.8 \mu\text{m}$, and (b) p-Channel Device with $L_{\text{eff}} = 0.7 \mu\text{m}$	36
3-15	Subthreshold Current-Voltage Characteristics of n- and p-Channel Devices with Various Values of L_{eff} . The Drain Bias Voltages Are +3 and -3 V, Respectively.	38
3-16	Threshold Voltage vs Effective Channel Length for n- and p-Channel Devices	39
3-17	Threshold Voltage Distributions for (a) n- and (b) p-Channel Devices with $L_{\text{eff}} = 1.2 \mu\text{m}$. The Standard Deviation Is 38 mV for Both Types of Devices.	40
3-18	(a) Output Waveform of 39-Stage Ring Oscillator with $L_{\text{eff}} = 0.8 \mu\text{m}$ at a Supply Voltage of 5 V. (b) Propagation Delay as a Function of Supply Voltage.	41
3-19	Absorptance Spectra for Light Polarized Parallel to the c (Optic) Axis at Three Locations Along the Length of a Ti:Al ₂ O ₃ Crystal. (a) Ti ³⁺ Absorption Band; (b) Residual Infrared Absorption Band, Plotted on an Expanded Absorptance Scale.	42
3-20	Residual Absorption at 900 nm (α_{res}) vs Ti ³⁺ Absorption at 485 nm (α_{max}) for Ti:Al ₂ O ₃ Crystals	44
4-1	Cross-Sectional Depiction of Selective W Cladding of Laser-Written Poly-Si by the Silicon Reduction of WF ₆	48
4-2	Resistance Reduction Factor R_o/R_f (Ratio of Original to Final Resistance) of p ⁺ Laser-Written Polysilicon Interconnects Undergoing Selective Tungsten Deposition vs Reaction Temperature	49
4-3	Resistance vs Length for Comparable B-Doped Laser-Direct-Written Polysilicon Interconnects Before and After WF ₆ Treatment at 475°C	49
4-4	Fabrication Method for Submicrometer-Gate-Length MESFETs with Self-Aligned Ohmic Contacts	50
4-5	Submicrometer "T"-Shaped Gate with Self-Aligned Ohmic Contact	52

Figure No.		Page
4-6	DC Trace for a $0.5 \times 300\text{-}\mu\text{m}$ Gate MESFET	52
4-7	A $0.5 \times 600\text{-}\mu\text{m}$ Gate MESFET Monolithic Power Amplifier	53
4-8	A 5×5 Baugh-Wooley Array Multiplier	54
4-9	Column Replacement Scheme for an Array Multiplier	56
5-1	Schematic Drawing of Single-Channel Time-Integrating Correlator	60
5-2	Electrical Schematic of Mixer-Integrator Peak-Detector Correlation Cell	60
5-3	Plot of Integrated Resonator Current as a Function of Input Power Levels and Integration Time	61
5-4	Frequency Response of Holographic Acoustic Grating	63
5-5	Limits on Quality Factor Q of a Holographic Acoustic-Grating Resonator Imposed by Propagation Loss (Descending Lines), Length of Grating (for Single-Pass Resonator), and Cavity Length of Resonator (a Grating-Element Reflectivity of 2×10^{-4} Was Assumed)	64
5-6	Block Diagram of the Narrowband Canceler	66
5-7	Predicted Cancellation Ratio vs Interference Level	67
5-8	Power Output of System with a 10-dBm CW Input, Slowly Swept in Frequency: (a) Cancellation Loop Disabled; (b) Loop Enabled	68
5-9	Narrowband Canceler Response to Steps in Frequency and Amplitude (+10-dBm Maximum Input Level)	69

LIST OF TABLES

Table No.		Page
5-1	Characteristics of Bulk-Acoustic Holograms	62

INTRODUCTION

1. SOLID STATE DEVICE RESEARCH

Two-tone intermodulation distortion in interferometric optical waveguide modulators has been analyzed. Peak amplitudes of sinusoidal input voltages must be less than 0.09 V_π in order to maintain greater than 40-dB intermodulation suppression.

Mass-transported GaInAsP/InP buried-heterostructure lasers have been successfully fabricated on p-type InP substrates. The advantages of the p-substrate for low electrical resistance, fabrication simplicity, and improved wafer uniformity have been demonstrated.

2. QUANTUM ELECTRONICS

The output of a CW room-temperature Ti:Al₂O₃ laser has been continuously tuned from 693 to 948 nm. This tuning range is limited by the bandwidth of the cavity mirrors, not by the gain bandwidth of the laser crystal.

Further studies of the Er:YAG laser as a potential energy storage medium for diode laser pumping have demonstrated an internal quantum slope efficiency of 20 percent at moderate pump intensities. Model predictions indicate that much higher efficiencies should be obtainable at higher pump levels.

LiNbO₃ devices utilizing the transverse electro-optic effect are being investigated as intracavity wavelength selectors for fast laser tuning. Initial studies have been conducted concerning optical damage, and operation in the desired wavelength range (0.7 to 0.9 μm) appears feasible.

Spectroscopic observation of coupled states in a double quantum well system has been made. Well-defined coupled states indicate the quality of the samples and raise the possibility of a quantum mechanical transport device.

Time response of the permeable base transistor (PBT) to large-signal ultrafast pulses has been studied. These experiments have established that the PBT can amplify large signals that rise and fall in a time interval at least as fast as 50 ps.

3. MATERIALS RESEARCH

To obtain data for optimizing the design of reactors for growing III-V layers by organometallic vapor phase epitaxy, the gas flow patterns in a vertical reactor tube have been visualized by using a sheet of laser light to illuminate smoke particles of TiO₂ transported through the tube in a stream of He gas. The test results suggest that the preferred approach for growing uniform epilayers with abrupt compositional changes is to combine gas injection through a porous plug with low-pressure operation, which will minimize convective instabilities resulting both from thermal gradients and from switching between gases of different densities, such as arsine and phosphine.

Light emission normal to the surface of a GaAs/AlGaAs wafer has been obtained by fabricating edge-emitting double-heterostructure diode lasers with a monolithic 45° deflector adjacent to one of

the laser facets. The deflector and adjacent facet were formed by ion-beam-assisted etching, while the other facet was cleaved. Diode-laser/deflector devices with two etched laser facets could be used to fabricate monolithic two-dimensional laser arrays.

Fully monolithic integration of GaAs/AlGaAs LEDs and Si MOSFETs connected in series has been achieved for devices fabricated on a wafer prepared by using molecular beam epitaxy to grow GaAs/AlGaAs layers on a Si substrate. By applying a stream of voltage pulses to the MOSFET gate, a LED modulation rate of 10 MHz has been obtained.

CMOS devices with effective channel lengths as short as 0.7 μm have been fabricated in zone-melting-recrystallized silicon-on-insulator films prepared by the graphite-strip-heater technique. Because low-temperature processing was used to minimize dopant diffusion along subboundaries in the films, these devices exhibit low leakage currents ($<0.1 \text{ pA}/\mu\text{m}$), small short-channel effects, and high-speed performance.

For as-grown Ti:Al₂O₃ samples with the lowest residual infrared absorption for a given Ti³⁺ intraatomic absorption, the residual absorption has been found to be proportional to the square of the Ti³⁺ absorption, which peaks at 490 nm. When one of these samples was annealed in an oxygen-argon atmosphere to oxidize some of the Ti³⁺ ions to Ti⁴⁺ ions, the resulting decrease in Ti³⁺ absorption was accompanied by an increase in residual absorption, suggesting that the residual absorption is associated with Ti³⁺-Ti⁴⁺ pairs.

4. MICROELECTRONICS

Polysilicon interconnections were locally deposited on oxide-covered silicon wafers by pyrolysis of silane using a scanned Ar⁺-laser spot, and were subsequently reacted with WF₆ vapor to form a tungsten-silicon composite interconnect by the silicon reduction of WF₆. This process enhances the conductivity of 0.4- μm -thick polysilicon conductors up to 20-fold by formation of a surface tungsten layer having approximately the bulk conductivity value.

A new method for the fabrication of submicron-gatelength GaAs MESFETs with self-aligned ohmic contacts has been demonstrated. This method combines conventional lithography and a recently developed Pd-Ga-Au ohmic contact metallization to achieve device dimensions usually associated with electron-beam lithography.

Testable, restructurable, and fault-tolerant Baugh-Wooley two's-complement array multipliers have been designed. E-beam programmable floating gate devices and e-beam induced currents are used to achieve the testability and restructurability of the circuits.

A packaging jig has been designed and tested for the rapid assembly of whisker-contacted devices, such as quantum wells, for the submillimeter region.

5. ANALOG DEVICE TECHNOLOGY

A superconductive analog signal correlator for 2-GHz-bandwidth input signals has been fabricated and tested. The device includes a Josephson-junction peak detector to measure integrated correlation amplitudes; its measured response shows nearly linear integration of input signals of an approximately 2- μs duration.

Measurements of bulk-acoustic propagation loss and holographic-grating reflection coefficients of iron-doped lithium niobate with iron concentrations from 0.005 to 0.05 percent indicate that the material is adequate for resonators with fundamental frequencies of 2 to 5 GHz and quality factors of 10^5 . A 1.3-GHz resonator with a Q of 4.3×10^3 has been demonstrated.

In a canceler designed for the removal of rapidly changing narrowband interference in a wideband channel, a phase-locked loop (PLL) tracks and regenerates the interference, and a feedback loop is used to adjust the amplitude and phase of the PLL output so that it will, upon summation with the input signal, exactly cancel the interference. Interference suppression of 40 dB and a settling time of 20 μ s have been demonstrated across a 100-MHz bandwidth.

REPORTS ON SOLID STATE RESEARCH

1 February through 30 April 1986

PUBLISHED REPORTS

Journal Articles

JA No.

5739	An Investigation of the Co:MgF ₂ Laser System	P.F. Moulton	IEEE J. Quantum Electron. QE-21, 1582 (1985)
5762	Linewidth Control with Masked Ion Beam Lithography Using Stencil Masks	J.N. Randall E.I. Bromley N.P. Economou	J. Vac. Sci. Technol. B 4, 10 (1986), DTIC AD-A167747
5763	Low-Resistance Ohmic Contacts to p-Type GaAs Using Zn/Pd/Au Metallization	R.C. Brooks C.L. Chen A. Chu L.J. Mahoney J.C. Mavroides M.J. Manfra M.C. Finn	IEEE Electron Device Lett. EDL-6, 525 (1985)
5777	The Contrast of Ion Beam Stencil Masks	J.N. Randall L.A. Stern J.P. Donnelly	J. Vac. Sci. Technol. B 4, 201 (1986), DTIC AD-A167612
5779	Sub-100-nm-Wide, Deep Trenches Defined by Reactive Ion Etching	S.W. Pang J.N. Randall M.W. Geis	J. Vac. Sci. Technol. B 4, 341 (1986), DTIC AD-A167279
5785	The Focused Ion Beam as an Integrated Circuit Restructuring Tool	J. Melngailis* C.R. Musil* E.H. Stevens* M. Utlaut* E.M. Kellogg* R. Post* M.W. Geis R.W. Mountain	J. Vac. Sci. Technol. B 4, 176 (1986)

* Author not at Lincoln Laboratory.

JA No.

5788	Excimer-Laser Etching of Diamond and Hard Carbon Films by Direct Writing and Optical Projection	M. Rothschild C. Arnone D.J. Ehrlich	J. Vac. Sci. Technol. B 4, 310 (1986), DTIC AD-A167438
5790	Hot Jet Etching of GaAs and Si	M.W. Geis N.N. Efremow G.A. Lincoln	J. Vac. Sci. Technol. B 4, 315 (1986), DTIC AD-A167508
5794	Anisotropic Etching of Al by a Directed Cl ₂ Flux	N.N. Efremow M.W. Geis R.W. Mountain G.A. Lincoln J.N. Randall N.P. Economou	J. Vac. Sci. Technol. B 4, 337 (1986), DTIC AD-A167505
5804	Use of Zone-Melting Recrystallization to Fabricate a 3-Dimensional Structure Incorporating Power Bipolar and Field-Effect Transistors	M.W. Geis C.K. Chen R.W. Mountain N.P. Economou W.T. Lindley P.L. Hower*	IEEE Electron Device Lett. EDL-7 , 41 (1986)
5805	Surface Damage on GaAs Induced by Reactive Ion Etching and Sputter Etching	S.W. Pang	J. Electrochem. Soc. 133, 784 (1986)
5812	Laser Etching of 0.4-μm Structures in CdTe by Dynamic Light Guiding	C. Arnone M. Rothschild D.J. Ehrlich	Appl. Phys. Lett. 48 , 736 (1986)
5813	Low Resistance Pd/Ge/Au and Ge/Pd/Au Ohmic Contacts to n-Type GaAs	C.L. Chen L.J. Mahoney M.C. Finn R.C. Brooks A. Chu J.G. Mavroides	Appl. Phys. Lett. 48 , 535 (1986)
5827	Monolithic Integration of Si MOSFETs and GaAs MESFETs	H.K. Choi G.W. Turner B-Y. Tsaur	IEEE Electron Device Lett. EDL-7 , 241 (1986)

* Author not at Lincoln Laboratory.

JA No.

5829	Visible-Laser Photodeposition of Chromium Oxide Films and Single Crystals	C. Arnone M. Rothschild J.G. Black D.J. Ehrlich	Appl. Phys. Lett. 48 , 1018 (1986)
5832	Radiation-Hardened Silicon-on-Insulator Complementary Junction Field-Effect Transistors	B-Y. Tsaur H.K. Choi	IEEE Electron Device Lett. EDL-7, 324 (1986)

Meeting Speeches**MS No.**

6869	A Wideband Packet Radio Based on Hybrid Analog/Digital Signal Processing and Layered Architecture	J.H. Fischer J.H. Cafarella G.T. Flynn C.A. Bouman D.R. Arsenault J.D. Kurtze R.R. Boisvert	In <i>1985 Military Communications Conference Proceedings</i> (IEEE, New York, 1985), p. 369
6957	Wideband Chirp-Transform Adaptive Filter	D.R. Arsenault	In <i>1985 Ultrasonics Symposium Proceedings</i> (IEEE, New York, 1985), pp. 102-107
6960	SAW/FET Programmable Transversal Filter with 100-MHz Bandwidth and Enhanced Programmability	D.E. Oates D.L. Smythe J.B. Green	In <i>1985 Ultrasonics Symposium Proceedings</i> (IEEE, New York, 1985), pp. 124-129
6961	Autocalibration Circuitry for Processing SAW Convolver Outputs	J.H. Fischer	In <i>1985 Ultrasonics Symposium Proceedings</i> (IEEE, New York, 1985), pp. 134-139
6967	Single-Cell Concepts for Obtaining Photovoltaic Conversion Efficiency Over 30%	J.C.C. Fan	In <i>Eighteenth IEEE Photovoltaic Specialists Conference — 1985</i> (IEEE, New York, 1985), pp. 28-32
6970	High-Efficiency Double-Heterostructure AlGaAs/GaAs Solar Cells	R.P. Gale J.C.C. Fan G.W. Turner R.L. Chapman	In <i>Eighteenth IEEE Photovoltaic Specialists Conference — 1985</i> (IEEE, New York, 1985), pp. 296-299

MS No.

7039	Serrodyne Frequency Translation with High Side-Band Suppression	L.M. Johnson C.H. Cox, III	1986 Integrated and Guided- Wave Optics Technical Digest, Atlanta, Georgia, 26-28 February 1986, pp. 56-57
7040	Performance and Reproducibility of Mach-Zehnder Interferometer Arrays in Ti:LiNbO ₃ Operating at Wavelengths from 0.458 to 3.39 μ m	R.H. Rediker T.A. Lind	1986 Integrated and Guided- Wave Optics Technical Digest, Atlanta, Georgia, 26-28 February 1986, p. 64

* * * * *

UNPUBLISHED REPORTS**Journal Articles****JA No.**

5831	You Too Can Present a Paper	D.L. Hovey R. Ponton*	Accepted by Fusion — The Journal of the American Scientific Glassblowers Society
5834	New Capping Technique for Zone-Melting Recrystallization of Silicon-on-Insulator Films	C.K. Chen M.W. Geis M.C. Finn B-Y. Tsaur	Accepted by Appl. Phys. Lett.
5837	Electronic Structure of Deep-Lying Sulfur Centers in Si	W.E. Krag [†] W.H. Kleiner H.J. Zeiger	Accepted by Phys. Rev. B
5838	Transient Transport Mea- surements on Ion Implanted Polymers	B. Wasserman* M.S. Dresselhaus* M. Wolf* J.D. Woodhouse G.E. Wnek*	Accepted by J. Appl. Phys.

* Author not at Lincoln Laboratory.

† Deceased.

JA No.

5845	Magnetic and Optical Measurements on Ti:Al ₂ O ₃ Crystals: Concentration and Absorption Cross Section of Ti ³⁺ Ions	R.L. Aggarwal A. Sanchez R.E. Fahey A.J. Strauss	Accepted by Appl. Phys. Lett.
5846	Room Temperature cw Operation of a Ti:Al ₂ O ₃ Laser	A. Sanchez R.E. Fahey A.J. Strauss R.L. Aggarwal	Accepted by Opt. Lett.
5847	Crystalline Films on Amorphous Substrates by Zone-Melting and Surface-Energy-Driven Grain Growth in Conjunction with Patterning	H.I. Smith* M.W. Geis C.V. Thompson C.K. Chen	Accepted by Materials Research Society
5848	Titanium-Doped Semi-insulating InP Grown by the Liquid-Encapsulated Czochralski Method	G.W. Iseler B.S. Ahern*	Accepted by Appl. Phys. Lett.
5850	Rapid Low Resistance Interconnects by Selective Tungsten Deposition on Laser Direct Written Polysilicon	J.G. Black D.J. Ehrlich J.H.C. Sedlacek A.D. Feinerman* H.H. Busta*	Accepted by IEEE Electron Device Lett.
5851	Monolithic Two-Dimensional Arrays of High-Power GaInAsP/InP Surface-Emitting Diode Lasers	J.N. Walpole Z.L. Liau	Accepted by Appl. Phys. Lett.
5853	A Comparison of Traveling-Wave LiNbO ₃ Optical Couplers and Interferometric Modulators	J.P. Donnelly A. Gopinath	Accepted by IEEE J. Quantum Electron.
5854	Fully Implanted p-Column InP Field-Effect Transistor	J.D. Woodhouse J.P. Donnelly	Accepted by IEEE Electron Device Lett.
5856	Monolithic GaAs/AlGaAs Diode-Laser/Deflector Devices for Light Emission Normal to the Surface	T.H. Windhorn W.D. Goodhue	Accepted by Appl. Phys. Lett.

* Author not at Lincoln Laboratory.

JA No.

5863	Submicrometer CMOS Devices in Zone-Melting-Recrystallized SOI Films	B-Y. Tsaur C.K. Chen	Accepted by IEEE Electron Device Lett.
5868	Laser-Controlled Wet Chemical Etching for Corrective Trimming of Thin Films: Applications to Aluminum	J.Y. Tsao D.J. Ehrlich	Accepted by J. Electrochem. Soc.

Meeting Speeches***MS No.**

6878A	CCD for Image Signal Processing	A.M. Chiang	Seminar, Eastman Kodak, Rochester, New York, 20 March 1986
6922A	Permeable Base Transistors	C.O. Bozler	American Physical Society, Las Vegas, 31 March — 4 April 1986
6935A	GaAs/AlGaAs Diode Lasers on Monolithic GaAs/Si Substrates	T.H. Windhorn G.W. Turner G.M. Metze	
7047A	Monolithic Integration of Si MOSFETs and GaAs MESFETs	H.K. Choi G.W. Turner B-Y. Tsaur	1986 Spring Meeting of the Materials Research Society, Palo Alto, California, 15-18 April 1986
7073	High-Speed Photoconductive Detectors Fabricated in Heteroepitaxial Layers	G.W. Turner V. Diadiuk H.Q. Le H.K. Choi G.M. Metze B-Y. Tsaur	
6984A	Balanced Monolithic Mixer for Use at 44 GHz	B.J. Clifton	IEEE Technical Meeting, Boston Section, Lincoln Laboratory, 17 April 1986
7159	Planar Mixer Arrays for Imaging at Millimeter Wavelengths	J.A. Taylor	

* Titles of Meeting Speeches are listed for information only. No copies are available for distribution.

MS No.

6997A	Reproducible Fabrication of High-Performance GaAs Permeable Base Transistors	M. Hollis K.B. Nichols R.A. Murphy R.P. Gale S. Rabe W.J. Piacentini C.O. Bozler P.M. Smith*	WOCSEMMAD '86, San Francisco, 10-13 February 1986
7066	Large Room Temperature Effects from Resonant Tunneling Through AlAs Barriers	W.D. Goodhue T.C.L.G. Sollner H. Le B.A. Vojak	
7071	Resonant-Tunneling and Coupled-Well Devices	T.C.L.G. Sollner W.D. Goodhue C.A. Correa	
7044	CCD Spatial Light Modulators Using Electroabsorption Effects in Multiple Quantum Wells	B.E. Burke W.D. Goodhue K.B. Nichols	
7071A	Resonant-Tunneling and Coupled-Well Devices	T.C.L.G. Sollner	SPIE Symposium on Non-linear Optics and Applications, Los Angeles, 19-24 January 1986
7094	A Comparison of Neural-Network and Matched-Filter Processing for Detecting Lines in Images	P.M. Grant J.P. Sage	IBM Seminar, Yorktown Heights, New York, 19 March 1986
7095	A Neural-Network Integrated Circuit with Synapses Based on CCD/MNOS Principles	J.P. Sage K. Thompson R.S. Withers	
7128	SAW Technology for Spread-Spectrum Communications	D.R. Arsenault	
7129	CCD-Based Signal Processing for Spread-Spectrum Systems	S.C. Munroe	Workshop on Neural Networks for Computing, Snowbird, Utah, 13-16 April 1986
			AFCEA Tactical Communications Conference, Fort Wayne, Indiana, 22-24 April 1986

* Author not at Lincoln Laboratory.

MS No.

7144	Excimer Laser Projection Patterning With and Without Resists: Submicrometer Etching of Diamond and Diamond-Like Carbon Resists	M. Rothschild C. Arnone D.J. Ehrlich	SPIE '86, Santa Clara, California, 9-14 March 1986
7150A, B	Flow Visualization Studies for Optimization of OMVPE Reactor Design	C.A. Wang S.H. Groves S.C. Palmateer D.W. Weyburne* R.A. Brown*	Third International Conference on Metalorganic Vapor Phase Epitaxy, Pasadena, California, 14-17 April 1986; Seminar, Dept. of Chemical Engineering, MIT, 27 March 1986
7151	Monolithic Two-Dimensional Arrays of High-Power GaInAsP/InP Surface-Emitting Diode Lasers	R.C. Williamson	Electrical Engineering Seminar, Univ. of Central Florida, 26 February 1986
7154	High-Speed Analog Gaussian Convolution for Edge Detection	A. Lattes	Joint Quantum Electronics and Superconductivity Seminar, Univ. of California, Berkeley, 5 March 1986
7156, 7156A	New Material Technologies for Integrated Circuits: Silicon-on-Insulator and Monolithic GaAs/Si	B-Y. Tsaur	VLSI Seminar, MIT, 18 March 1986; Seminar, Univ. of California, Berkeley, 21 April 1986
7162	Submicrometer Patterning by Projected Excimer-Laser-Beam Induced Chemistry	D.J. Ehrlich J.Y. Tsao C.O. Bozler	Seminar, Center for Integrated Electronics, Rensselaer Polytechnic Institute, Troy, New York, 4 March 1986
7191	Crystal Growth by Molecular Beam Epitaxy	A.R. Calawa W.D. Goodhue	Lincoln Laboratory Seminar Series, Howard University, Washington, DC, 4 April 1986

* Author not at Lincoln Laboratory.

ORGANIZATION

SOLID STATE DIVISION

A.L. McWhorter, *Head*
I. Melngailis, *Associate Head*
E. Stern, *Associate Head*
J.F. Goodwin, *Assistant*

P.E. Tannenwald, *Senior Staff*

QUANTUM ELECTRONICS

A. Mooradian, *Leader*
P.L. Kelley, *Associate Leader*

Barch, W.E. Killinger, D.K.
Belanger, L.J. Le, H.
Daneu, V. Menyuk, N.
DeFeo, W.E. Sanchez-Rubio, A.
Feldman, B. Sharpe, K.A.
Hancock, R.C. Sullivan, D.J.
Harrison, J.* Tong, F.
Jeys, T.H. Zaykowski, J.J.
Johnson, B.C.*

ELECTRONIC MATERIALS

A.J. Strauss, *Leader*
B-Y. Tsaur, *Assistant Leader*
H.J. Zeiger, *Senior Staff*

Anderson, C.H., Jr. Kolesar, D.F.
Button, M.J. Krohn, L., Jr.
Chen, C.K. Mastromattei, E.L.
Choi, H.K. Nitishin, P.M.
Connors, M.K. Pantano, J.V.
Delaney, E.J. Tracy, D.M.
Eglash, S.J. Turner, G.W.
Fahey, R.E. Wang, C.A.
Finn, M.C. Windhorn, T.H.
Iseler, G.W.

APPLIED PHYSICS

R.C. Williamson, *Leader*
D.L. Spears, *Assistant Leader*
T.C. Harman, *Senior Staff*
R.H. Rediker, *Senior Staff*

Anderson, K.K.* Palmateer, S.C.
Aull, B.F. Plonko, M.C.
Betts, G.E. Reeder, R.E.
Chan, S.K.* Tsang, D.Z.
Cox, C.H., III Lind, T.A.
DeMeo, N.L., Jr. McBride, W.F.
Diadiuk, V. Metze, G.M.
Donnelly, J.P. Molter, L.A.*
Ferrante, G.A. O'Donnell, F.J.
Walpole, J.N.
Whitaker, N.*
Woodhouse, J.D.
Yap, D.*
Yee, A.C.

* Research Assistant

ANALOG DEVICE TECHNOLOGY

R.W. Ralston, *Leader*
R.S. Withers, *Assistant Leader*

Anderson, A.C.	Flynn, G.T.	Macropoulos, W.
Arsenault, D.R.	Grant, P.M.*	Marden, J.A.
Boisvert, R.R.	Green, J.B.	Munroe, S.C.
Brogan, W.T.	Holtham, J.H.	Oates, D.E.
Denneno, A.P.	Kernan, W.C.	Sage, J.P.
Dilorio, M.S.	Koulman, W.A.	Slattery, R.L.
Dolat, V.S.	Lattes, A.L.	Thompson, K.E.†
Fischer, J.H.	Lichtenwalner, D.J.†	Wong, S.†
Fitch, G.L.	Macedo, E.M., Jr.	

MICROELECTRONICS

W.T. Lindley, *Leader*
D.J. Ehrlich, *Assistant Leader*
B.B. Kosicki, *Assistant Leader*
R.A. Murphy, *Assistant Leader*

Astolfi, D.K.	Geis, M.W.	Oliver, S.†
Bales, J.W.†	Goodhue, W.D.	Paczuski, M.†
Bennett, P.C.	Gray, R.V.	Pang, S.W.
Black, J.G.	Hollis, M.A.	Parker, C.D.
Bozler, C.O.	Huang, J.C.M.	Pichler, H.H.
Brown, E.R.	Lax, B.§	Rabe, S.
Burke, B.E.	LeCoz, Y.L.†	Rathman, D.D.
Calawa, A.R.	Lincoln, G.A., Jr.	Reinold, J.H.
Chen, C.L.	Lysczarz, T.M.	Rothschild, M.
Chiang, A.M.	Mahoney, L.J.	Sedlacek, J.H.C.
Clifton, B.J.	Maki, P.A.	Smythe, D.L., Jr.
Daniels, P.J.	Manfra, M.J.	Sollner, T.C.L.G.
Doran, S.P.	Matthews, R.	Taylor, J.A.†
Durant, G.L.	McGonagle, W.H.	Utarro, R.S.
Efremow, N.N., Jr.	Melngailis, J.§	Vera, A.
Felton, B.J.	Mountain, R.W.	Wilde, R.E.
Gajar, S.†	Nichols, K.B.	Young, E.

* Visiting

† Research Assistant

‡ Staff Associate

§ Part Time

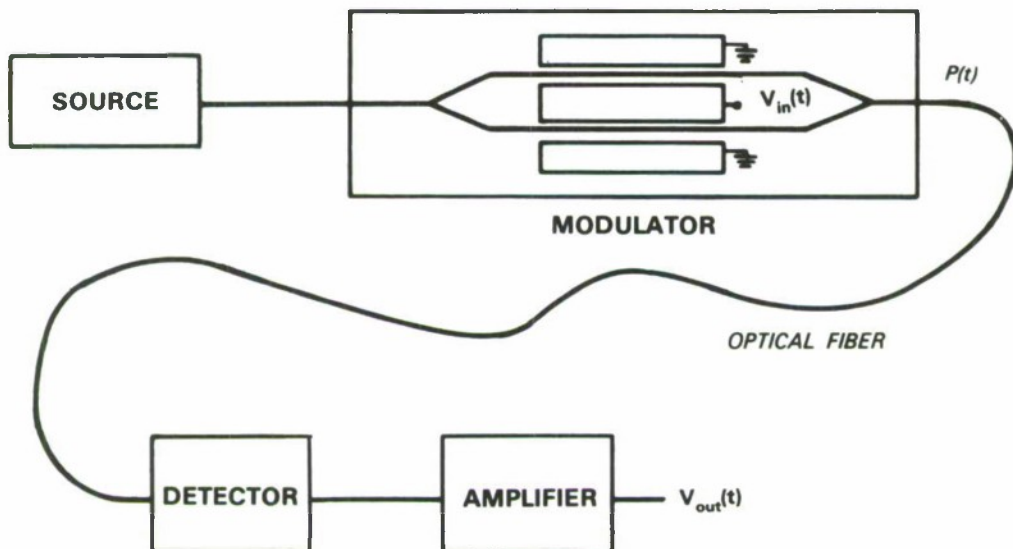
1. SOLID STATE DEVICE RESEARCH

1.1 INTERMODULATION DISTORTION IN INTERFEROMETRIC OPTICAL MODULATORS

Analog optical-fiber communication links are being actively developed for many applications in radar and telemetry systems. One attractive scheme for implementing such analog links is to employ a constant-power optical source with a high-speed external modulator. Guided-wave optical modulators with bandwidths as high as 16 GHz have been demonstrated.^{1,2} However, the dynamic range of analog links employing these modulators can be limited by modulator nonlinearities. An experimental and theoretical study of harmonic distortion in optical waveguide modulators has been previously reported.³ In many systems though, particularly those operating over a narrow fractional bandwidth, intermodulation distortion will be the limiting factor in achieving wide dynamic range. Here, we present the results of a theoretical analysis of two-tone intermodulation distortion in interferometric waveguide modulators.

The analog link being considered is illustrated in Figure 1-1. It contains a single-mode channel-waveguide Mach-Zehnder interferometric modulator which is driven by an input voltage V_{in} and operated with a phase bias of approximately $\pi/2$ such that the power out of the modulator, $P(t)$, is approximately linear in V_{in} . The system output voltage V_{out} is proportional to $P(t)$ and is given by the relation

$$V_{out}(t) = V_o \{ \sin [\phi(t) + \phi_E] + 1 \} \quad (1-1)$$



76607-1

Figure 1-1. Analog optical-fiber communication link consisting of constant-power optical source, interferometric modulator, optical fiber, detector, and amplifier.

where $\phi(t)$ is the applied phase difference between the two arms of the device, and ϕ_E is the phase bias error. It is also assumed that the phase difference $\phi(t)$ is linearly proportional to the modulator drive voltage $V_{in}(t)$ and is given by

$$\phi(t) = \frac{\pi V_{in}(t)}{V_\pi} \quad (1-2)$$

where V_π is equal to the voltage variation required for maximum on-off modulation. The nonlinearities and consequent distortions analyzed here are associated with the sinusoidal nature of the system response. Although this analysis is focused on Mach-Zehnder interferometers, the results apply to any system with a sinusoidal transfer function.

To analyze two-tone intermodulation distortion, we assume that the input voltage consists of two simultaneous equal-amplitude sinusoidal signals which result in a phase modulation

$$\phi(t) = \phi_m(\sin \omega_1 t + \sin \omega_2 t) \quad (1-3)$$

If the output of the analog link is filtered to block the dc component, then the output voltage can be written in series form as

$$V_{out}(t) = \sum_{k=0}^{\infty} V_{k,0} (\sin k\omega_1 t + \sin k\omega_2 t) + \sum_{k=1}^{\infty} \sum_{\ell=1}^{\infty} V_{k\ell} [\sin (k\omega_1 + \ell\omega_2) t + \sin (k\omega_1 - \ell\omega_2) t] \quad (1-4)$$

where the relative values of the coefficients $V_{k\ell}$ are a function of the drive-signal amplitude $\phi_m(t)$. The first and second summations correspond to harmonic and intermodulation distortion, respectively. The harmonic distortion occurs at integral multiples of ω_1 and ω_2 and can be removed by filtering in any system which operates over less than an octave bandwidth. The dominant intermodulation components of $V_{out}(t)$ are represented by the coefficients $V_{1,2} = V_{2,1}$. If $\omega_1 \approx \omega_2$, the dominant intermodulation frequencies $2\omega_1 - \omega_2$ and $2\omega_2 - \omega_1$ will be close to the drive frequencies. These intermodulation components cannot always be removed by filtering if we allow ω_1 and ω_2 to assume any value in the bandwidth of the system.

The amplitude coefficients $V_{k\ell}$ are determined by combining Equations (1-1) and (1-3) and expanding the result in a Bessel-function series. The amplitude terms $V_{1,0}$ for the fundamentals, $V_{1,2}$ for the dominant intermodulation signals, $V_{2,0}$ for the second harmonics, and $V_{3,0}$ for the third harmonics are then given by the expressions

$$\begin{aligned} V_{1,0} &= 2V_o J_1(\phi_m) J_0(\phi_m) \cos \phi_E \\ V_{1,2} &= 2V_o J_1(\phi_m) J_2(\phi_m) \cos \phi_E \\ V_{2,0} &= 2V_o J_2(\phi_m) J_0(\phi_m) \sin \phi_E \\ V_{3,0} &= 2V_o J_3(\phi_m) J_0(\phi_m) \cos \phi_E \end{aligned}$$

where J_n is the n^{th} -order Bessel function. These results show that in analog links with over an octave bandwidth, where second-harmonic products cannot be filtered out, the phase bias error ϕ_E must be kept close to zero. Conversely, third-order intermodulation products cannot always be filtered out and these are insensitive to ϕ_E when $\phi_E \approx 0$.

The output power of the link at the fundamental and intermodulation frequencies as a function of normalized drive power is shown in Figure 1-2 by plotting $20 \log (|V_{k\ell}|/V_0)$ vs $20 \log (2\phi_m/\pi)$ for $V_{1,0}$ and $V_{1,2}$ assuming $\phi_E = 0$. For low input drive power there is a factor-of-3 difference in slope between the two curves, which is expected for this third-order intermodulation process. Extrapolation to the intermodulation intercept point is also shown and occurs when $\phi_m = 162^\circ$. These results can be used to determine the upper end of the dynamic range in systems limited by intermodulation distortion. For example, suppression of third-order intermodulation products to a level 40 dB below the fundamental requires that ϕ_m be restricted to a level more than 20 dB below 162° or, equivalently, $\phi_m \leq 16.2^\circ$, which corresponds to an input voltage peak amplitude of $0.09 V_\pi$ for each sinusoidal input.

L.M. Johnson

R.C. Williamson

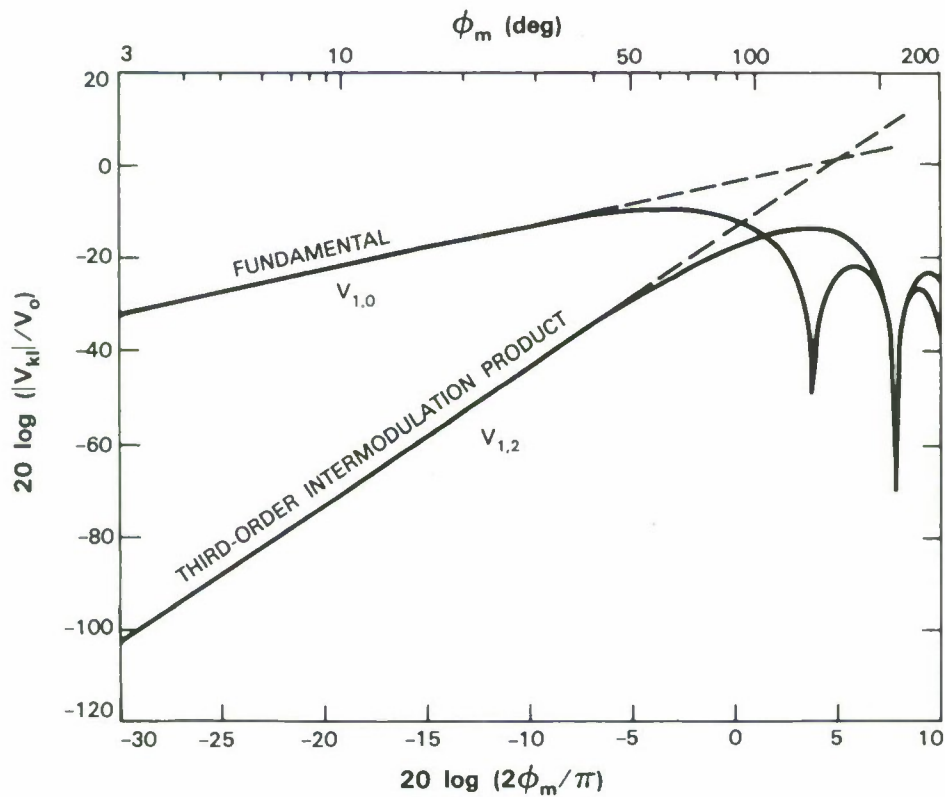


Figure 1-2. Plot of fundamental and intermodulation product power levels as a function of electrical drive power. Extrapolation to the intermodulation intercept is shown.

1.2 HIGH-PERFORMANCE MASS-TRANSPORTED p-SUBSTRATE GaInAsP/InP BURIED-HETEROSTRUCTURE LASERS AND THEIR ARRAYS

The use of p-type InP substrates for GaInAsP/InP buried-heterostructure (BH) lasers offers several advantages over n-type substrates, including low series resistance and fabrication simplicity, and recently such devices with very high output powers have been reported.^{4,5} Here, we report the successful fabrication of mass-transported p-substrate BH lasers (Figure 1-3) and one-dimensional monolithic laser arrays, with low series resistance, low threshold currents, high quantum efficiencies, and good uniformity across the array.

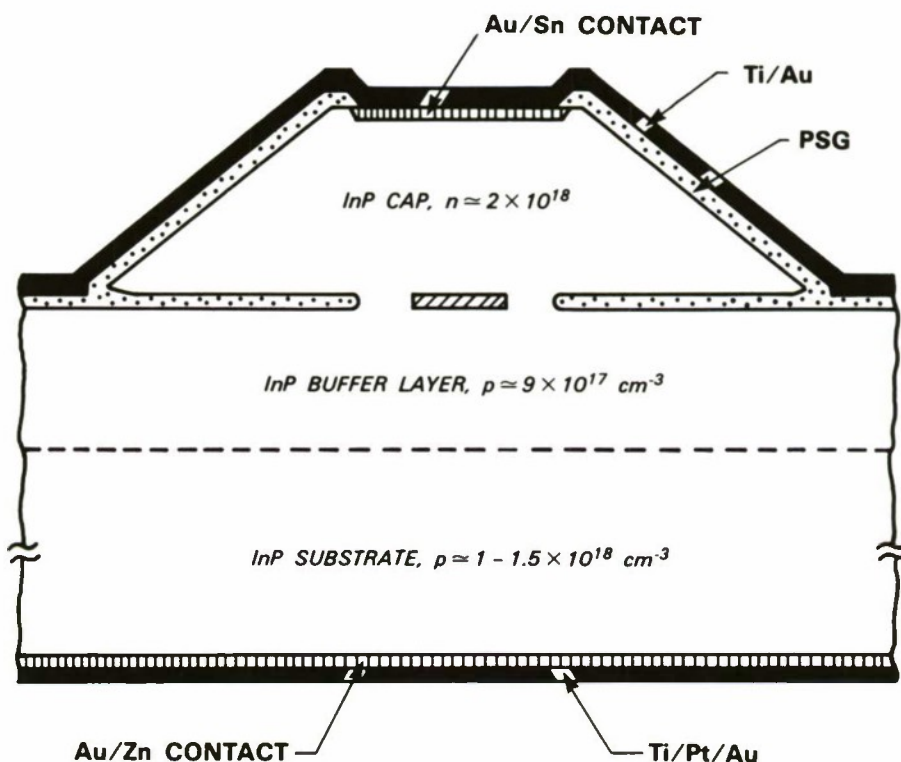


Figure 1-3. Schematic drawing of the transverse cross-sectional view of a mass-transported p-substrate GaInAsP/InP buried-heterostructure laser.

76607-3

The device fabrication is similar to that previously described,⁶ including selective chemical etching and mass transport on LPE-grown double-heterostructure wafers, except for the use of p-substrates and narrow ($\leq 1 \mu\text{m}$) transported regions. High yield of good devices has been obtained with CW threshold currents as low as 5.5 mA, differential quantum efficiencies as high as 29 percent per facet, and with typical series resistance values of 4.2Ω for $350\text{-}\mu\text{m}$ -long devices. This series resistance is close to the calculated⁷ spreading resistance in the substrate ($p \approx 1.5 \times 10^{18} \text{ cm}^{-3}$), indicating that the large-area p-contact indeed has a very small resistance. The present low resistance represents a considerable improvement over the previous case of a 4×4 array of

p-substrate surface-emitting lasers⁸ and is due to an improved ohmic contact fabrication procedure. Room-temperature CW output power greater than 30 mW per facet has been achieved, as shown in Figure 1-4. It is worth noting that this device has a maximum quantum efficiency of 48 percent (both facets) at 84 mA and a maximum power efficiency of 36 percent at 47 mA. Similar devices fabricated with narrow contact pads have shown small-signal modulation bandwidths as large as 16 GHz (see Reference 9).

One-dimensional arrays have been fabricated in the form of long, cleaved bars on which lasers with individual contact pads are spaced 127 μm apart. Initial results on a bar of 18 lasers show 15 of them with 10.5- to 16.2-mA threshold currents and differential quantum efficiencies in the range of 21 to 29 percent per facet (see Figure 1-5).

Z.L. Liau
J.N. Walpole
L.J. Missaggia

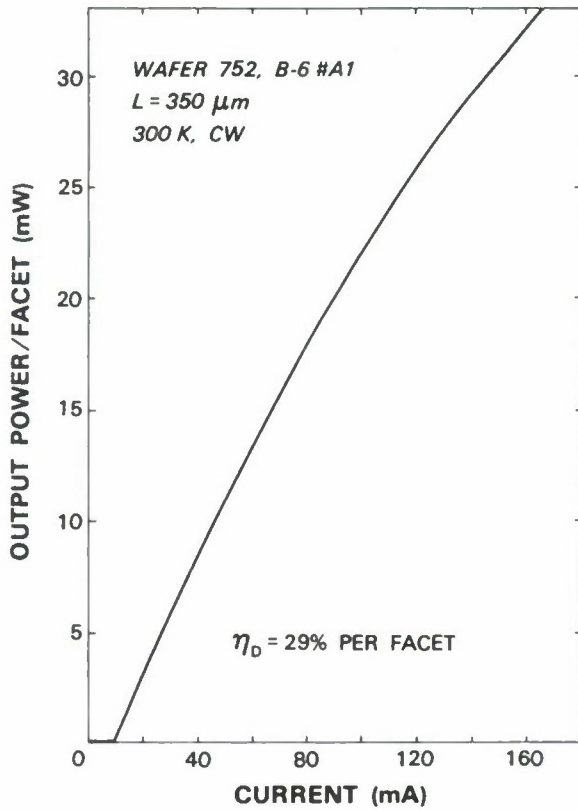


Figure 1-4. Light output vs current characteristic of a mass-transported p-substrate GaInAsP/InP BH laser. The device is mounted junction side down on a copper heat sink.

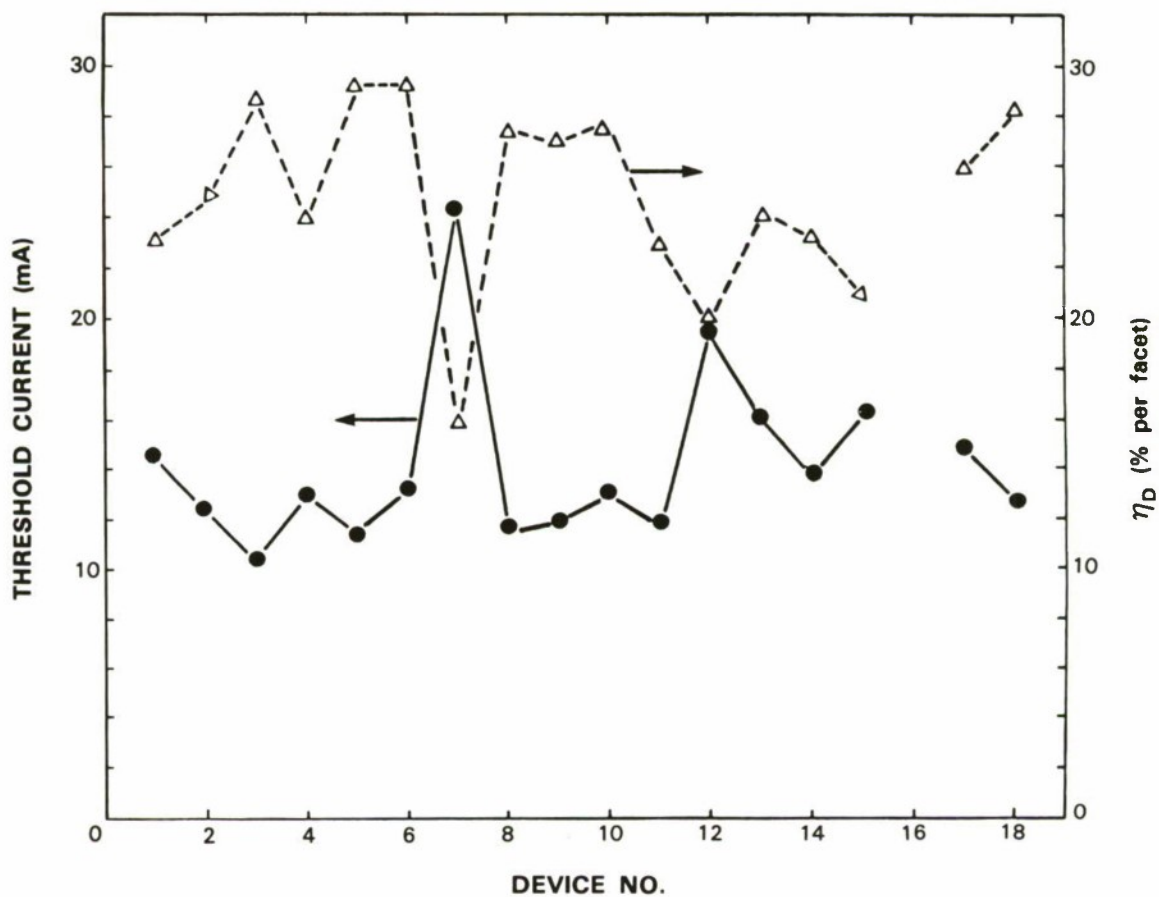


Figure 1-5. Threshold currents and differential quantum efficiencies of lasers in a monolithic one-dimensional array.

75607-5

REFERENCES

1. R.A. Becker, Appl. Phys. Lett. **45**, 1168 (1984), DTIC AD-A150629.
2. R.C. Alferness, S.K. Korotky, L.L. Buhl, and M.D. Divino, Electron. Lett. **20**, 354 (1984).
3. C.H. Bulmer and W.K. Burns, IEEE J. Lightwave Technol. LT-**2**, 512 (1984).
4. Y. Nakano, K. Takahei, Y. Noguchi, Y. Suzuki, H. Nagai, and K. Nawata, Electron. Lett. **17**, 782 (1981).
5. See, for example, K. Imanaka, H. Horikawa, A. Matoba, Y. Kawai, and M. Sakuta, Appl. Phys. Lett. **45**, 282 (1984).
6. Z.L. Liau, J.N. Walpole, and D.Z. Tsang, IEEE J. Quantum Electron. QE-**20**, 855 (1984), DTIC AD-A149328.
7. Solid State Research Report, Lincoln Laboratory, MIT (1985:4), pp. 6-10.
8. *Ibid.* (1986:1), pp. 1-4.
9. D.Z. Tsang and Z.L. Liau, unpublished.

2. QUANTUM ELECTRONICS

2.1 TUNING CHARACTERISTICS OF A ROOM-TEMPERATURE CW Ti:Al₂O₃ LASER

In our previous report,¹ we described the CW operation of a Ti:Al₂O₃ laser at room temperature. A maximum output power of 1.6 W was obtained at 770 nm, near the peak of the gain profile, when the Brewster-cut laser rod was pumped with 12 W of incident radiation from a multi-line argon-ion laser. We have now demonstrated continuous tuning of this room-temperature CW Ti:Al₂O₃ laser from 693 to 948 nm. Tunable pulsed operation of a Ti:Al₂O₃ laser, using a pulsed dye laser as the pump source, has been reported previously.² As shown in Figure 2-1, the Ti:Al₂O₃ laser rod is placed at the waist of an astigmatically compensated three-mirror cavity, and the pump radiation is injected through the folding mirror. Tuning is accomplished by a three-plate intracavity Lyot filter, and the laser output is observed with a 0.1-nm-resolution grating spectrometer. In initial experiments, tuning was limited to the range from 715 to 825 nm by the bandwidth of the concave coupling mirror, which reaches its minimum transmission of 0.7 percent at 765 nm.

75607-6

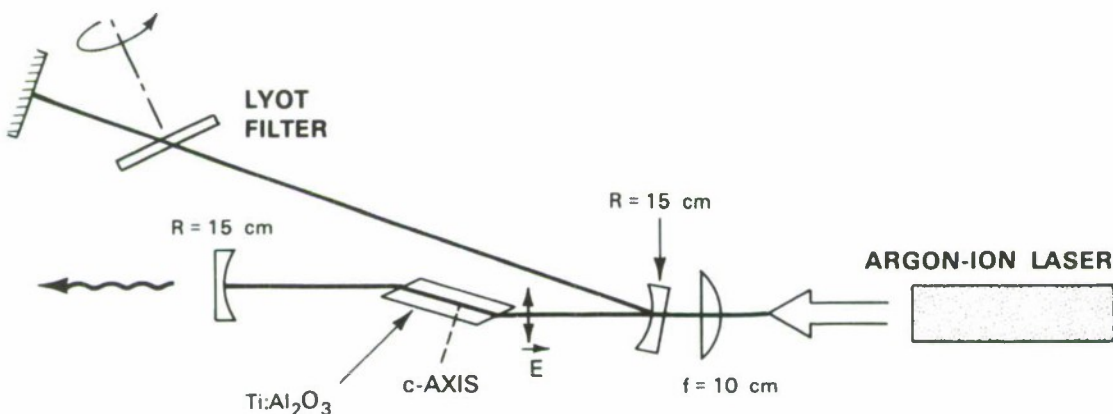


Figure 2-1. Schematic of the experimental setup showing the Ar-ion pump laser and the three-mirror folded cavity for the Ti:Al₂O₃ laser.

In subsequent studies, all three cavity mirrors had broadband, highly reflecting dielectric coatings, and the laser radiation was coupled out by a near-Brewster intracavity plate. For this configuration, tuning was limited to the range from 705 to 915 nm by branch jumping of the Lyot filter. Finally, an intracavity prism was added to prevent branch jumping, extending laser emission from 693 to 948 nm. In this case the tuning range was limited by the bandwidth of the cavity mirrors, not by the bandwidth of the Ti:Al₂O₃ crystal. It is therefore expected that the tuning range would be extended by using cavity optics with larger bandwidth.

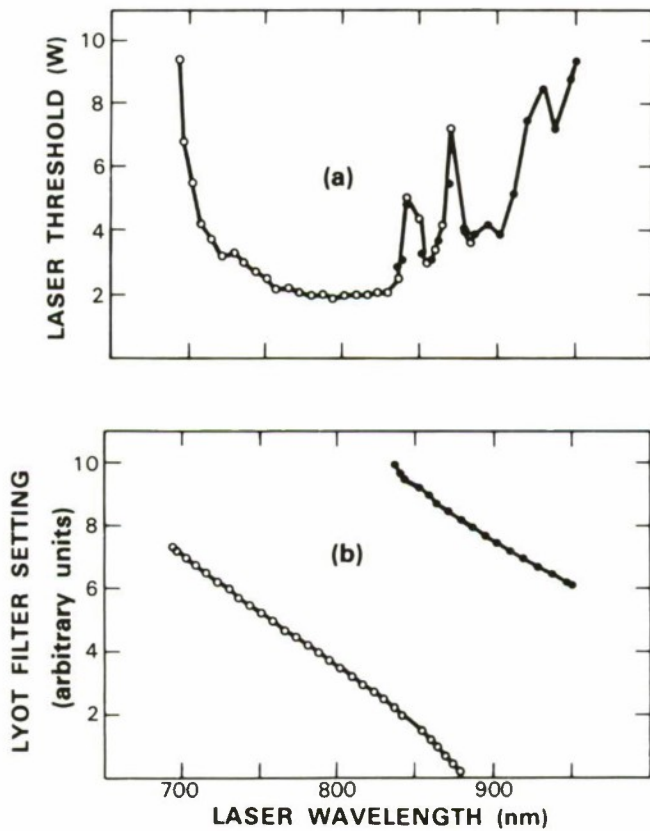


Figure 2-2. Tuning characteristics of the Ti:Al₂O₃ laser. (a) Laser threshold power (incident on the rod) vs wavelength. (b) Laser wavelength(s) for each setting of the Lyot filter, showing the two filter transmission branches.

Figure 2-2(a) shows the laser threshold as a function of wavelength for the final configuration. The spikes at long wavelengths can be attributed to the characteristics of the cavity mirrors. Within the laser tuning range, the Lyot filter exhibits the two transmission branches shown in Figure 2-2(b), which is a plot of the laser wavelength(s) obtained for each setting of the filter. In the range where the filter transmission is double valued, the laser wavelength was determined by the setting of the intracavity prism.

A. Sanchez
R.E. Fahey

A.J. Strauss
R.L. Aggarwal

2.2 Er:YAG LASER DEVELOPMENT

The 1.65-μm Er:YAG laser is being studied as a potential energy storage medium for 1.47-μm diode laser pumping and has been successfully operated with this pump and output wavelength combination as reported in the previous Solid State Research Report. Recent laser experiments using a 29-cm confocal laser cavity, 77 K cooled Er:YAG laser crystal, and a tunable

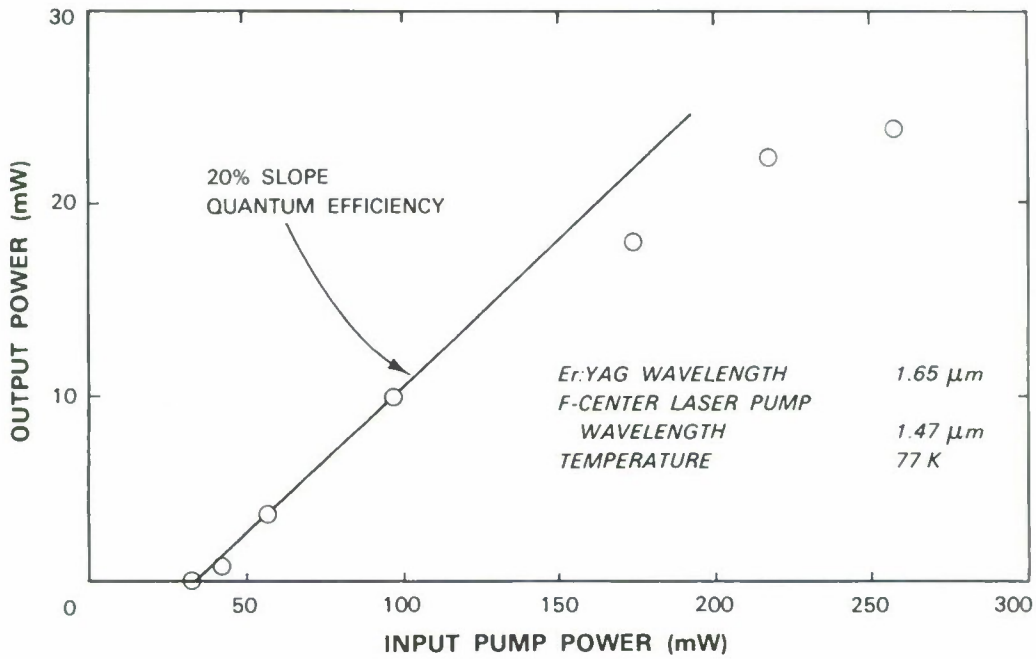


Figure 2-3. CW output power of 1.65- μm Er:YAG laser as a function of input 1.47- μm laser pump power.

1.47- μm F-center pump laser have yielded laser efficiency data as shown in Figure 2-3. The internal quantum slope efficiency is 20 percent and the laser threshold is approximately 45 mW; maximum laser pump intensities are of the order of 50 to 100 W/cm². Preliminary modeling of the operation of a Er:YAG laser has been made, including the effects of absorption, excited state lifetimes, and parasitic upconversion as a function of temperature and pump intensity. The predictions appear to be in reasonable agreement with the experimental data for 77 K operation, but indicate that parasitic upconversion may be a limiting factor for laser operation at higher temperatures. Further experiments are being conducted to better characterize laser performance at these higher temperatures.

D.K. Killinger

2.3 STUDIES OF THE USE OF LiNbO₃ IN A LYOT FILTER SYSTEM

Current experiments on fast tuning for the frequency-agile laser are based on crystals utilizing the transverse, rather than longitudinal, electro-optic effect. The device geometry is shown in Figure 2-4. This represents one stage of the Lyot filter; the final device is expected to require three stages. We are presently investigating the crystal LiNbO₃ which has the advantage, compared with KD*P, of being non-hygroscopic and generally easier to handle and process and, because a cell is not needed to protect the crystal from ambient air, involves fewer optical interfaces. For a wave traveling along the natural optic axis as shown in Figure 2-4, the electro-optic

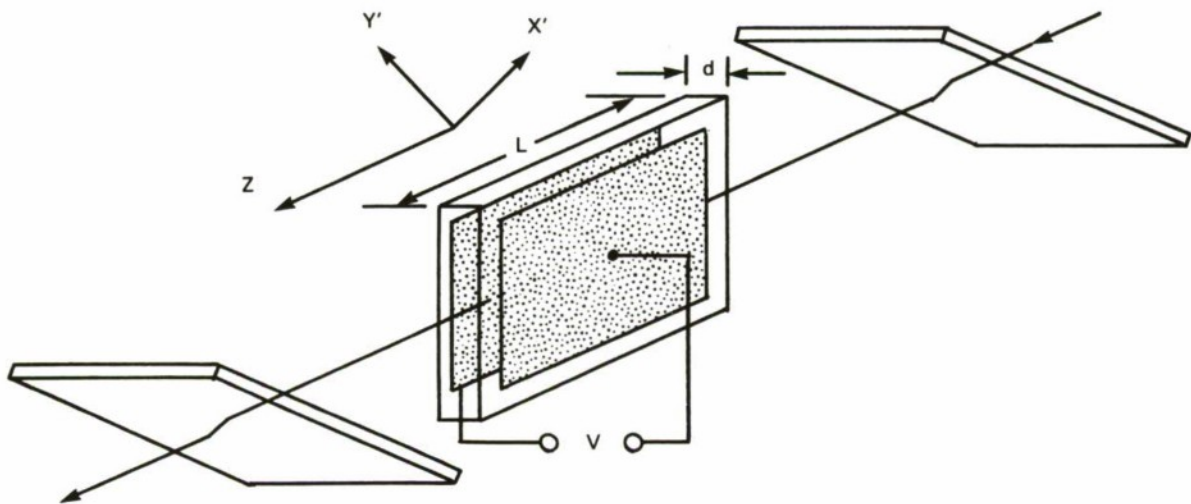


Figure 2-4. Lyot filter geometry utilizing the transverse electro-optic effect.

effect induces a birefringence between the two components of the optical field at $\pm 45^\circ$ to the preferred polarizer transmission. With the geometry of the figure, the relative retardation between two waves polarized along X',Y' is

$$\Phi_r = \frac{2nr_{22}n_o^3}{\lambda} \left(\frac{VL}{d} \right) \quad (2-1)$$

for one pass through the crystal. The geometrical factor L/d, typical of transverse-effect electro-optic devices, permits sizable retardations with reasonable applied voltages. The crystals used have L = 25 mm, d = 1 mm; Figure 2-5 shows the electro-optic transmission characteristic at 633 nm using sheet polarizers.

Several crystals have been procured and end-polished according to the geometry of Figure 2-4, and one set of three crystals has also been antireflection coated for less than 0.2-percent reflectivity at 633 nm. These crystals will be used for intracavity tuning experiments with a dye laser using, for example, DCM as the active dye. Initial attempts at inserting one LiNbO₃ device into a Ti:Al₂O₃ laser cavity have not yet succeeded, as the reflection loss at the operating wavelength (4-percent surface, $\lambda = 775$ nm) does not permit lasing. Antireflection coatings centered in the Ti:Al₂O₃ tuning range are being procured.

One crucial issue for devices using LiNbO₃ is that of optical damage (photorefractive effect) induced by the laser beam. Experiments have been performed, using a dye laser as a tunable polarization-modulated source, to assess the importance of bulk photorefractive effects in LiNbO₃ at the wavelengths of interest. In the yellow-green range (rhodamine 6G dye), optical damage precludes the intracavity use of LiNbO₃ devices, as the transmitted beam is distorted by light-induced refractive index changes. On the other hand, for extreme red or near-IR wavelengths the

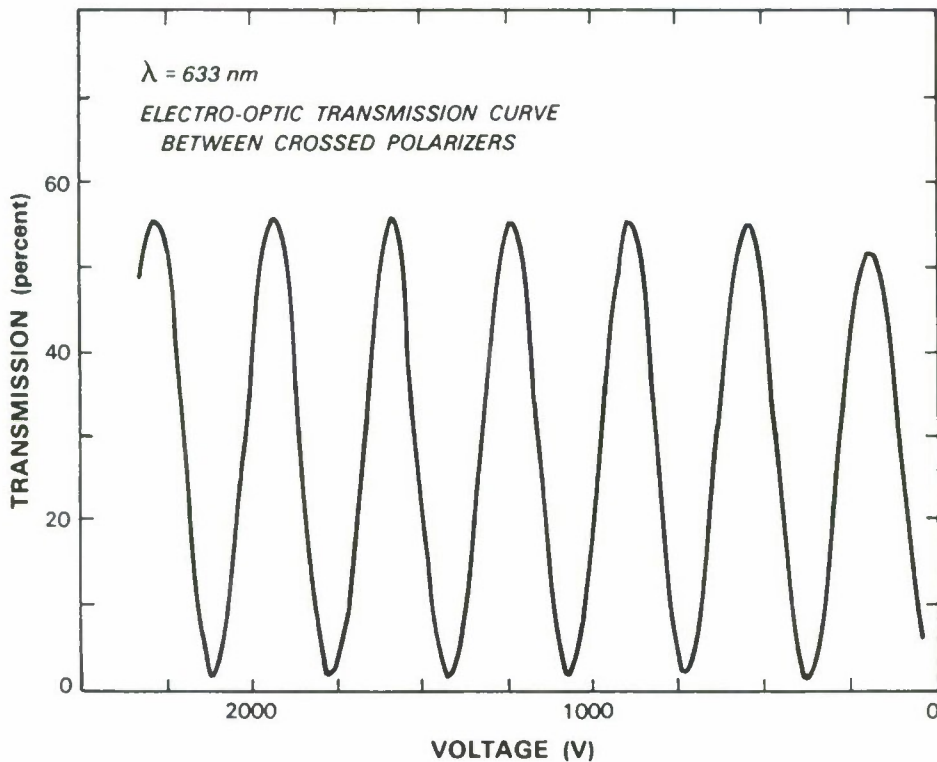


Figure 2-5. Transmission at 633 nm vs applied voltage on the LiNbO_3 crystal using the configuration shown in Figure 2-4.

optical damage seems to be limited to an additional, light-induced birefringence, which would imply a wavelength shift for a Lyot-type device. This could be corrected in the final design, where the operating wavelength is determined by comparison with a (tunable) reference cavity and electro-optic feedback. Considerable further study is required of this issue.

V. Daneu

2.4 SPECTROSCOPIC OBSERVATION OF COUPLED STATES IN AN $\text{AlGaAs}/\text{GaAs}$ COUPLED DOUBLE QUANTUM WELL SYSTEM

The interest in semiconductor heterostructures is to a large part aimed at a new class of devices that exploits the quantum nature of carriers in microscopic environments. In a realistic physical system, carriers occupying such states exhibit quantum behavior only when the inhomogeneous potential of an imperfect crystal does not perturb these states sufficiently to cause extensive mixing. Certain device applications, such as opto-electronic modulators, require wave functions with large spatial extent for maximal modulation effects. However, if carriers in such a structure suffer sufficiently strong scattering, the performance as a modulator will be degraded. In comparison with the single quantum well (SQW), the coupled double quantum well (CDQW)

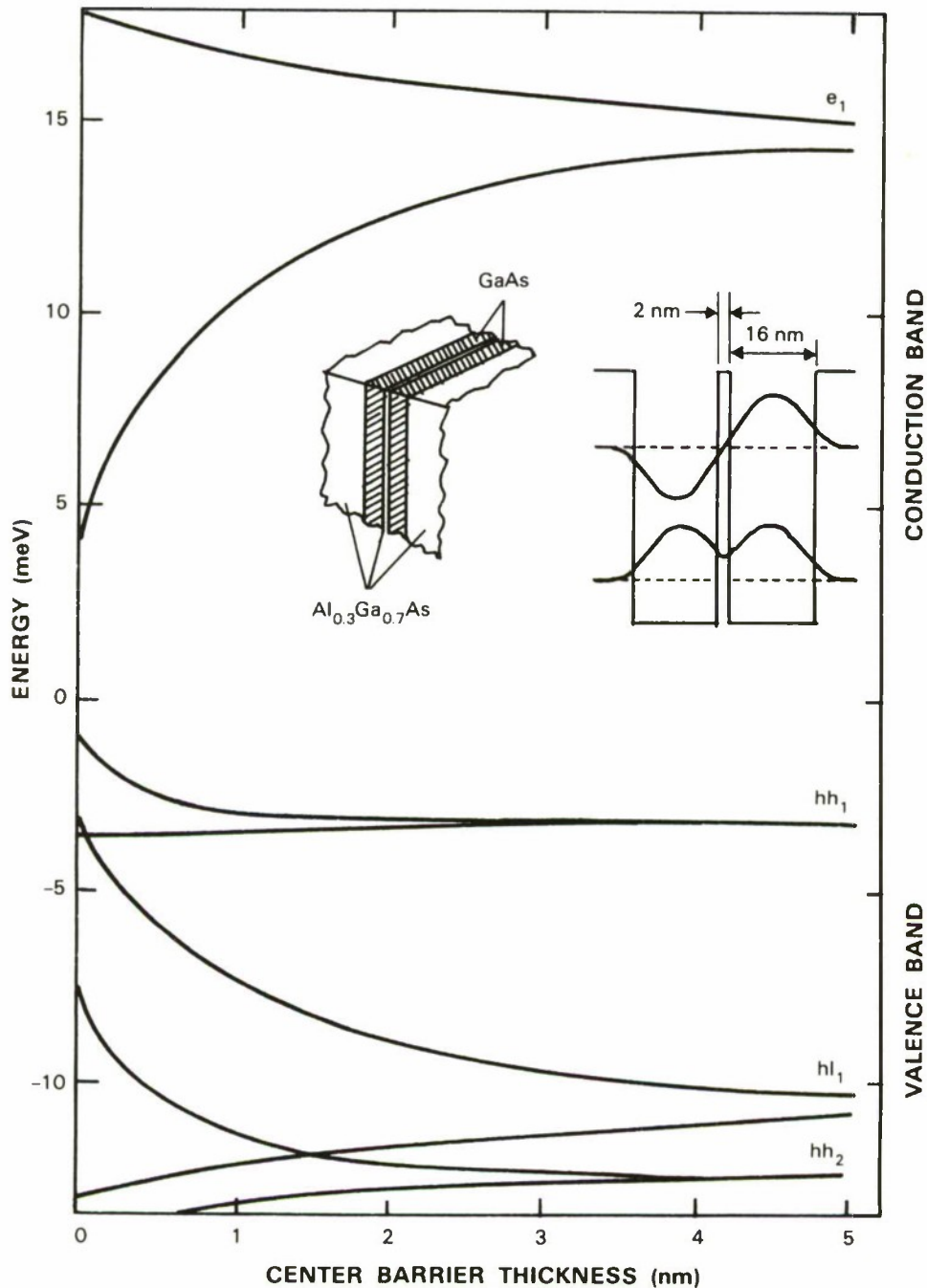


Figure 2-6. Energy levels of the lowest confined coupled states in the conduction and valence bands of a symmetric CDQW structure. For each pair of curves the higher energy level corresponds to the antisymmetric state, and the lower to the symmetric state. The labels e , hh , and hl indicate electron, heavy hole, and light hole, respectively. The insets show a physical section of the sample and the calculated wavefunctions for the lowest electron states in such structure. The energy levels of the valence band are inverted.

offers confined states with much more extended wave functions. In a CDQW structure, two SQWs are placed sufficiently close to each other that the quantized states are coherent in both wells and form coupled states. However, for a CDQW to be useful, the coupled states must be free of scattering that prevents quantum adiabatic transitions under rapid modulation of an external field. Such states also must be spectroscopically well defined.

We report the growth and observation of an AlGaAs/GaAs CDQW structure that exhibits clear evidence of coupled quantum states. The CDQW structure is about 34 nm in width. Experimental measurements indicate the high quality of the samples and raise the realistic possibility of devices based on the CDQW.

The sample depicted in the inset of Figure 2-6 is grown by MBE and is studied using luminescence and excitation spectroscopy. The wave functions in each of the QWs are coupled to form new states whose spatial extent overlaps both wells. For a symmetric CDQW, the inversion symmetry causes one-dimensional symmetric and antisymmetric states indicated by S and A, respectively. The wavefunctions of the two states for the CDQW model described are shown in the second inset of Figure 2-6. With the use of the effective mass approximation, the energy levels of the lowest coupled states for conduction band and valence bands are calculated and plotted. The levels are shown relative to the bottom of the respective bands. The individual well widths are kept constant and only the thickness of the center barrier is varied. In the conduction band the levels are denoted by e, while in the valence band the levels hh and hl refer to the heavy and the light holes, respectively. The heavy- and light-hole coupling is neglected in the calculation.

The spectroscopic results at a temperature of 2 K are shown in Figure 2-7; (a) and (b) are luminescence spectra on log and linear scales, respectively. The peak labeled (e_1^S , hh_1^S) is the well-known feature resulting from the radiative decay of the heavy-hole exciton that is formed using an electron in the lowest conduction band state and a heavy hole in the lowest valence band state. In the SQW structure, the next excited state is the light-hole exciton (e_1 , hl_1). For comparison, the inset of Figure 2-7 shows two excitation spectra of a multi-SQW sample. Curve (c') shows the (e_1 , hh_1) exciton 1S state and its continuum; curve (d') shows the (e_1 , hl_1) exciton 1S state. The CDQW excitation spectra (c) and (d) in Figure 2-7 are distinctly different and exhibit a much richer structure. Various peaks are labeled according to the level scheme given in Figure 2-6. Curve (c) is an excitation spectrum obtained with luminescence monitored at 1528.5 meV, a feature associated with impurity states. Curve (d) was obtained with light monitored at 1530.5 meV, the center of the heavy-hole exciton (e_1^S , hh_1^S) line. The similarity between (c) and (d) confirms the homogeneity in the origin of these resonances. It should be noted that if the two SQWs were not coupled, such results would not be obtained. If the two lowest energy features at 1530.5 and 1534.1 meV arose from the heavy-hole excitons in two uncoupled wells whose widths differed, the excitation spectrum based on the luminescence of the line at 1530.5 meV would not show any strong resonance at 1534.1 meV, since the absorption of excitation radiation at this transition would occur in the SQWs that are completely separate from the one being monitored. The fact that the same features appear in different excitation spectra indicates that they arise from the same system. On the other hand, even if the two SQWs were

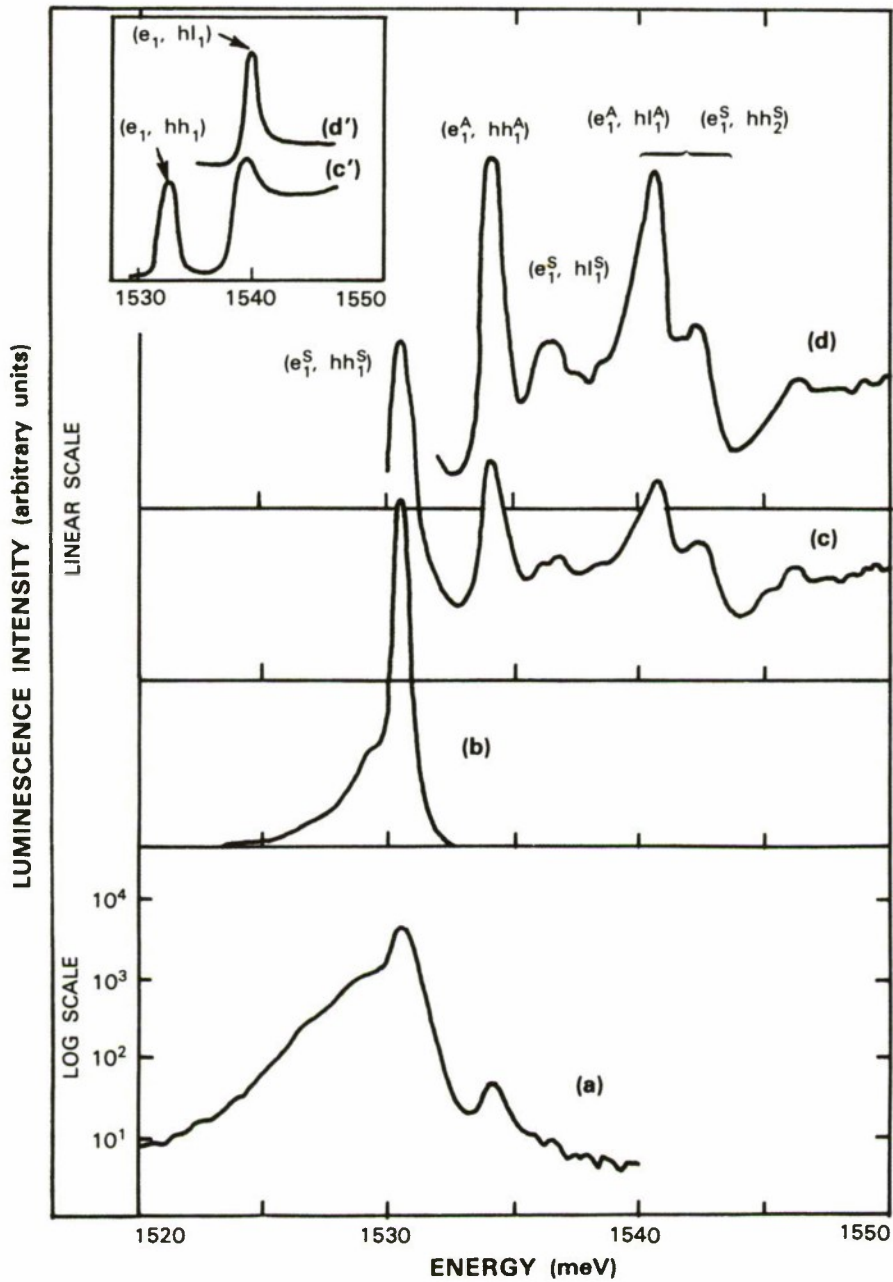


Figure 2-7. Luminescence and excitation spectra of a symmetric CDQW at 2 K. (a) and (b) are luminescence spectra at low excitation intensity ($<1 \text{ W/cm}^2$) on log and linear scales, respectively. (c) and (d) are excitation spectra, with luminescence monitored at 1528.5 and 1530.5 meV, respectively, while excitation photon energy is varied. Various structures are labeled according to the scheme given in Figure 2-6. The inset shows excitation spectra of multiple SQWs. Only two bound state peaks, corresponding to the heavy- and light-hole excitons, are observed.

coupled but carriers suffered strong scattering by a random potential in the center barrier, i.e., the coherence of the wave functions did not extend over both wells, the result would be a continuum in energy, namely, a band between the (e_1^S , hh_1^S) and (e_1^A , hh_1^A) lines. Thus, the clear resolution of these two sharp lines indicates the quality of the sample for observing coupled QW effects.

This work is in an exploratory stage. Studies of carrier transport properties and time-resolved measurements of relaxation between coupled states are in progress. More complex structures, such as asymmetric coupled QWs for fast opto-electronic applications and three-coupled-well systems for memory applications, are currently planned.

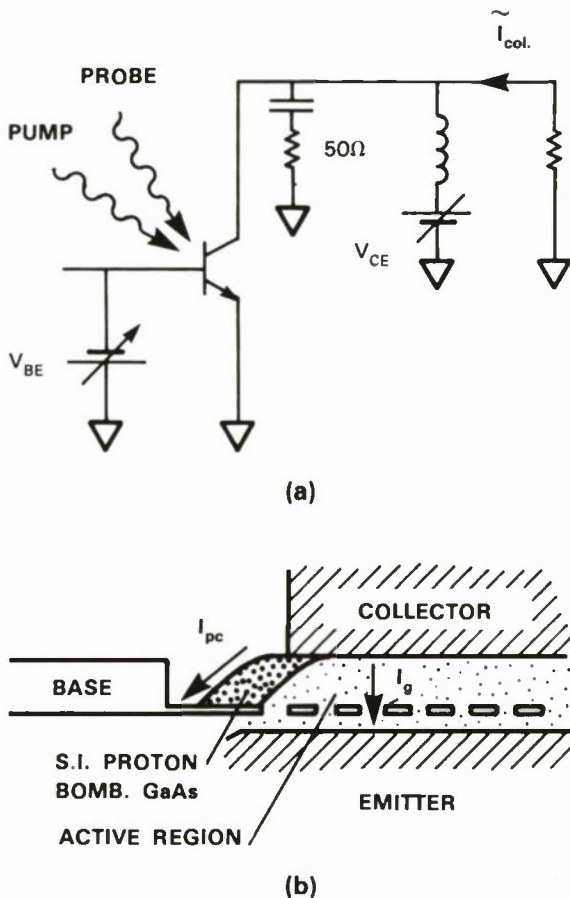
H.Q. Le
J.J. Zaykowski
W.D. Goodhue

2.5 TIME-RESOLVED STUDIES OF PHOTOCURRENT IN A PERMEABLE BASE TRANSISTOR

We have explored the potential of the permeable base transistor (PBT) as a fast opto-electronic device by measuring the speed of PBT response to current induced by picosecond laser pulses. The pulses were used to illuminate and generate carriers in the active region of a PBT, as shown in Figure 2-8. A pump and probe technique was employed with an optical energy per pulse of ≈ 20 pJ. The PBT collector current was monitored, and the correlation between pump and probe photocurrents was measured as a function of their relative time delay.

The results indicate that in the present configuration there are two components of photocurrent in the PBT. One fast component is due to the photoconductive response of the semi-insulating proton-bombarded GaAs overgrown between the base and the collector. This current (I_{pc}), which occurs outside the active region, is essentially parasitic and saturable. The other component, occurring within the active region, induces a gain in the collector-emitter current. The opposite behaviors of these two components are shown in the correlation measurement given in Figure 2-9. When the PBT was biased in an off-state, the negative I_{pc} correlation dominated. There also appeared to be a slower component, which was also due to a saturable base-collector photoconductive current, but occurring in the active region. When the PBT was turned on with low gain, a small gain current I_g appeared with a positive correlation sign and the parasitic component I_{pc} became most pronounced. Under increasing gain conditions, the growth of I_g correlation relative to that of I_{pc} became more and more evident. While the presence of I_{pc} is not desirable, its observation in this case serves a useful purpose. With two components of opposite signs, the evidence of gain in PBT photocurrent, as opposed to the well-known saturation behavior of photoconductive switches, is clearly established. To interpret the correlation results, we assume I_{pc} to be proportional to the optically generated carrier density n and the collector-base voltage V . Then the correlation signal is

$$I_{pc}(\tau) \propto \int n(t) [V(t - \tau) + V(t + \tau)] dt \quad (2-2)$$



75607-13

Figure 2-8. (a) Schematic of experimental setup. (b) PBT cross section; the light penetrates PBT through the window between the base and the collector.

where τ is the time delay between pump and probe excitations. Assuming the temporal behavior of $V(t)$ follows that of $n(t)$ (see Reference 3) and can be roughly approximated as an exponential decay, then, from the observed FWHM of $\langle I_{pc}(\tau) \rangle \approx 20$ ps, we can infer the temporal response of $V(t)$ to be ≈ 10 ps. This time scale is consistent with the typical photoconductive temporal response of radiation-damaged semiconductors.³

For the gain current, a phenomenological model leads to the correlation signal

$$\langle I_g(\tau) \rangle \propto \frac{dG}{di_{BE}} \int I_{CE}(t) [i_{BE}(t + \tau) + i_{BE}(t - \tau)] dt \quad (2-3)$$

where I_{CE} and i_{BE} are the collector-emitter and base-emitter currents, respectively. The former is the amplified signal of the latter. dG/di_{BE} is the derivative of the gain vs i_{BE} ; if the PBT is biased such that $dG/di_{BE} > 0$, a positive signal results. If we assume that $I_{CE}(t)$ is very fast and closely follows the exponential decay of $i_{BE}(t)$, a temporal response ≈ 50 ps is obtained from the

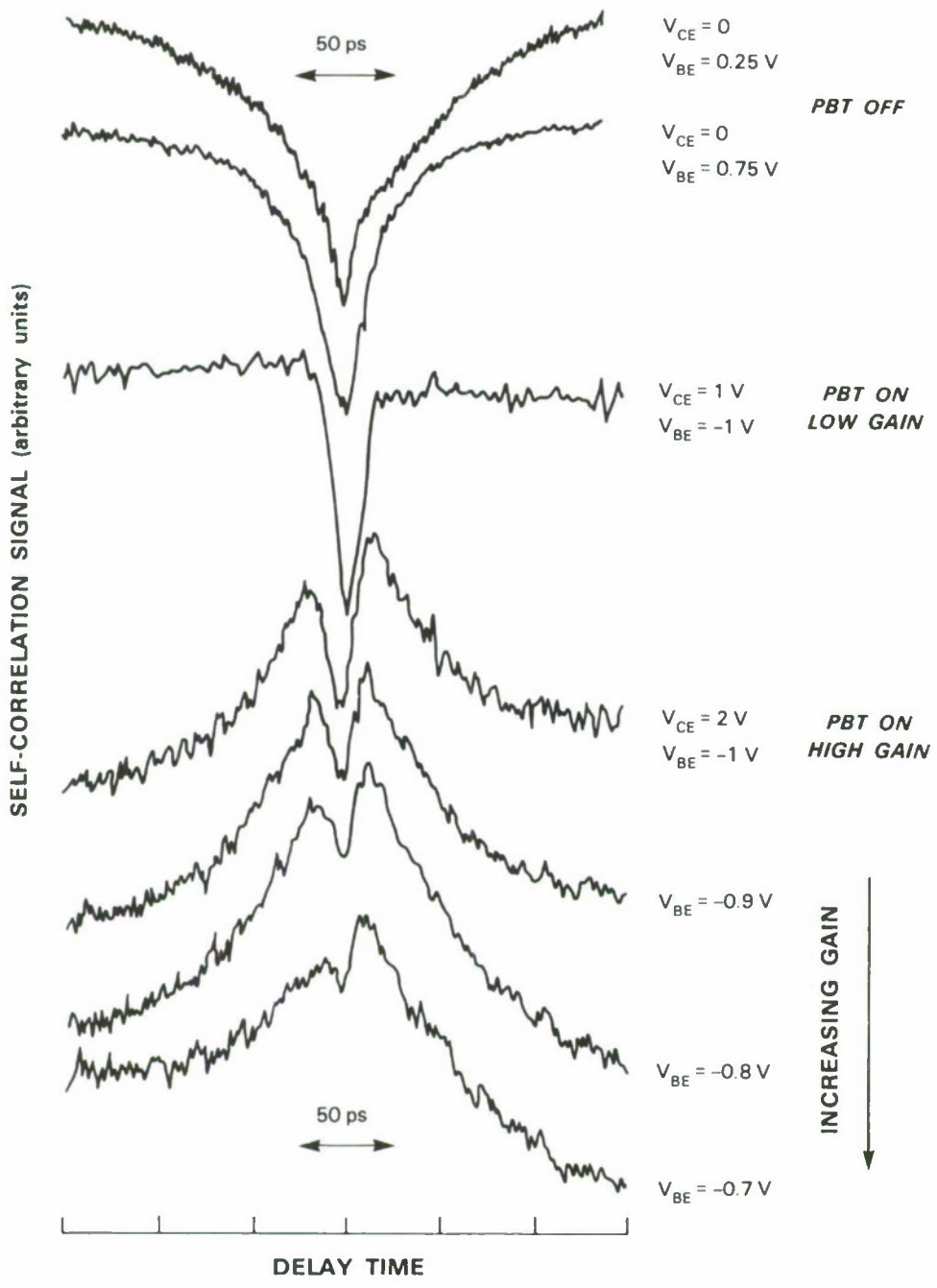


Figure 2-9. Correlation signals of pump and probe photocurrents as detected at the collector.

measured signals. This value is quite consistent with the observed photoconductive response of the typical high-quality n-type GaAs (see Reference 4) that makes up the PBT active region. It appears that this intrinsic response time limits the testing of PBT speed. Along with these two components of photocurrent, a small, much slower component with a nanosecond time scale also was observed. We believe this is due to the long-lived minority carriers from photoionization of deep traps and defects in the tungsten-GaAs interface.

While the PBT was not tested to its limit in speed, this study establishes that PBT can amplify signals which rise and fall in a time interval at least as fast as 50 ps. Also, compared with most photodiodes, the relatively high sensitivity of the PBT due to the gain process promises that the device could be a useful detector.

H.Q. Le
C.O. Bozler
R.H. Mathews

REFERENCES

1. Solid State Research Report, Lincoln Laboratory, MIT (1986:1), pp. 11-12.
2. P.F. Moulton, J. Opt. Soc. Am. B 3, 125 (1986).
3. C.H. Lee, Ed. *Picosecond Optoelectronic Devices* (Academic Press, New York, 1984).
4. V. Diadiuk, G.W. Turner, and H.Q. Le (unpublished).

3. MATERIALS RESEARCH

3.1 FLOW VISUALIZATION STUDIES FOR OMVPE REACTOR DESIGN

Reproducible growth of laterally uniform epilayers that have abrupt interfaces and can be made thin enough for quantum well and superlattice structures is necessary for many electronic and optoelectronic applications. Deposition of epilayers by organometallic vapor phase epitaxy (OMVPE) is usually limited by mass transport of reactants to the substrate. Consequently, epilayer quality is determined largely by gas dynamics in the reactor. For epilayer uniformity, the thickness of the boundary layer at the substrate should be uniform, so that deposition occurs at the same rate for all points on the substrate. For interface abruptness, the flow field in the reactor should be free of any laminar vortices in order to minimize gas residence times. In this investigation gas flow visualization achieved by light scattering from TiO_2 particles has been utilized to obtain data for optimizing the design and operation of OMVPE reactors in order to meet these two criteria. The test results suggest that the preferred approach is to combine gas injection through a porous plug with low-pressure operation.

The experimental apparatus is shown schematically in Figure 3-1. The vertical quartz tube, 10-cm i.d., incorporates a 6.7-cm-diam. RF-heated rotating graphite susceptor disk. The distance between the disk and the gas inlet is 15 cm. Three means have been used for gas injection: (a) a vertical 6-mm pipe inlet coaxial with the tube, (b) four equally spaced inlets tangential to the tube, and (c) a radial inlet above a porous plug, 7.6 cm in diameter, formed by metal screens.

Gas flow patterns are made visible by illuminating TiO_2 particles that are generated by the reaction of TiCl_4 and H_2O and then transported through the reactor in a stream of He carrier gas. Vertical and horizontal cross sections through the tube are illuminated with a sheet of light formed by directing the beam of a 5-mW He-Ne laser through a cylindrical lens. The intensity of scattered light is proportional to the local concentration of TiO_2 particles.

The effect of the method of gas injection on the flow field was studied for isothermal gas flow, with and without disk rotation. For injection through the porous plug, changes in flow patterns that resulted from heating the disk to 600°C, or from switching from one injected gas to another, were studied at atmospheric pressure and at reduced pressure.

The most common method of gas injection in OMVPE reactors utilizes a coaxial inlet pipe. Figure 3-2 shows a cross-sectional photograph of the gas flow pattern at room temperature obtained when this method was used with a He flow of 2 lpm and a tube pressure of 1 atm. An inertial jet extends from the inlet to the disk, showing that the flow is not fully developed. The gas flows outward radially across the disk and strikes the side of the tube to produce vortices between the top of the tube and the disk. These vortices persist when the smoke is turned off and result in gas residence times of many minutes. A high degree of radial nonuniformity and grading between epilayers would be expected from this type of flow.

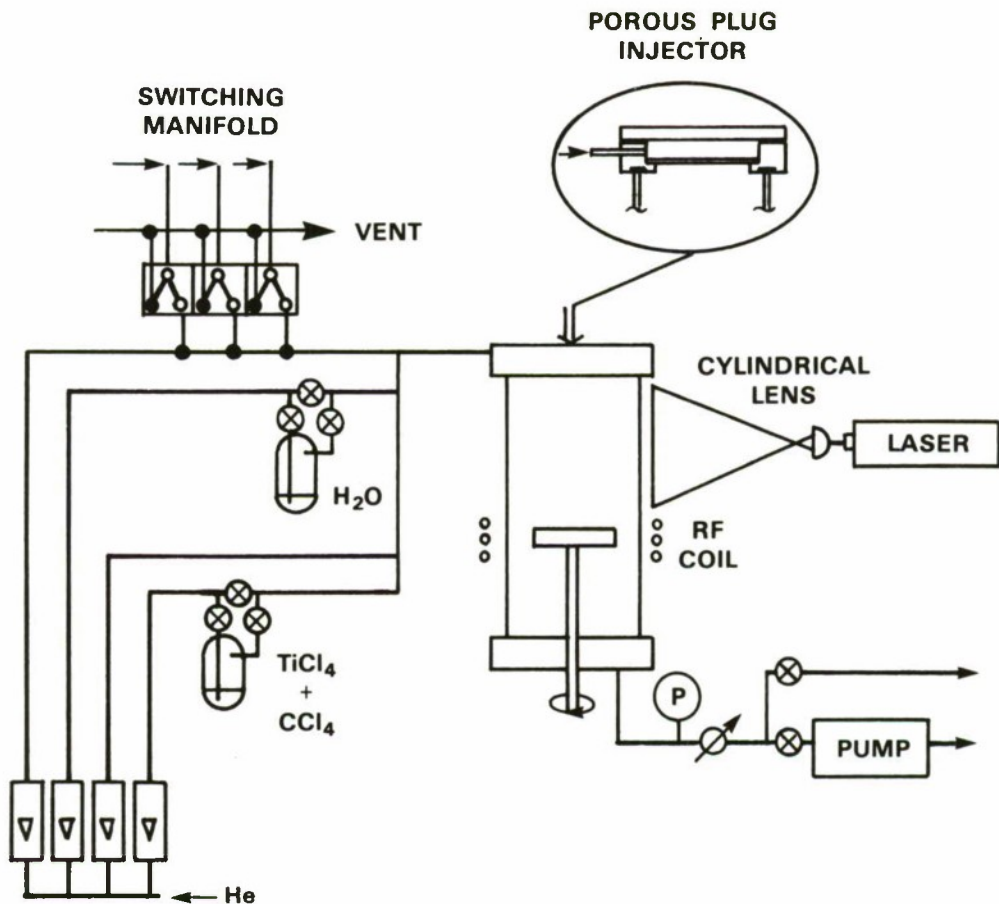


Figure 3-1. Schematic diagram of apparatus for gas flow visualization.

Injection through tangential inlets was employed to introduce swirl to the gas, increasing its path length and dissipating the momentum of the inlet stream. A steady-state pattern recorded at room temperature and 1 atm for a flow rate of 10 lpm is shown in Figure 3-3. Although the flow is fully developed at the disk surface, variations in smoke concentration in the vicinity of the disk indicate that the gas is not well mixed. The flow can be made laminar at the disk surface by rotating the disk at 80 rpm (Figure 3-4), but the formation of a vortex at the top of the tube results in long gas residence times.

Gas injection through a radial inlet above a porous plug resulted in uniform flow over a large cross section of the tube (as shown in Figure 3-5, which was obtained at room temperature and 1 atm for a flow rate of 10 lpm). Gas enters with a diameter equal to that of the plug and velocity nearly independent of diameter. The uniform density of smoke particles indicates that the gas is uniformly mixed. The time elapsed before laminar flow reached the disk was approximately 4 to 5 s, while 5 to 6 s were required for clearing the tube after the smoke was turned off. These times are comparable to the transit time calculated from the average velocity of the gas in the tube.

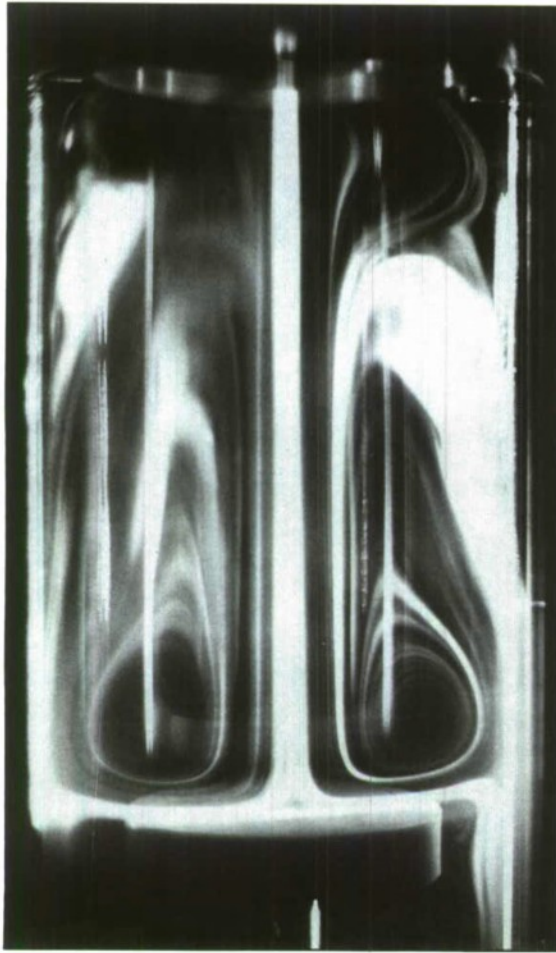


Figure 3-2. Flow pattern obtained for gas injection through a coaxial vertical pipe.



Figure 3-3. Flow pattern for gas injection through tangential inlets.



Figure 3-4. Flow pattern for gas injection through tangential inlets with disk rotation of 80 rpm.

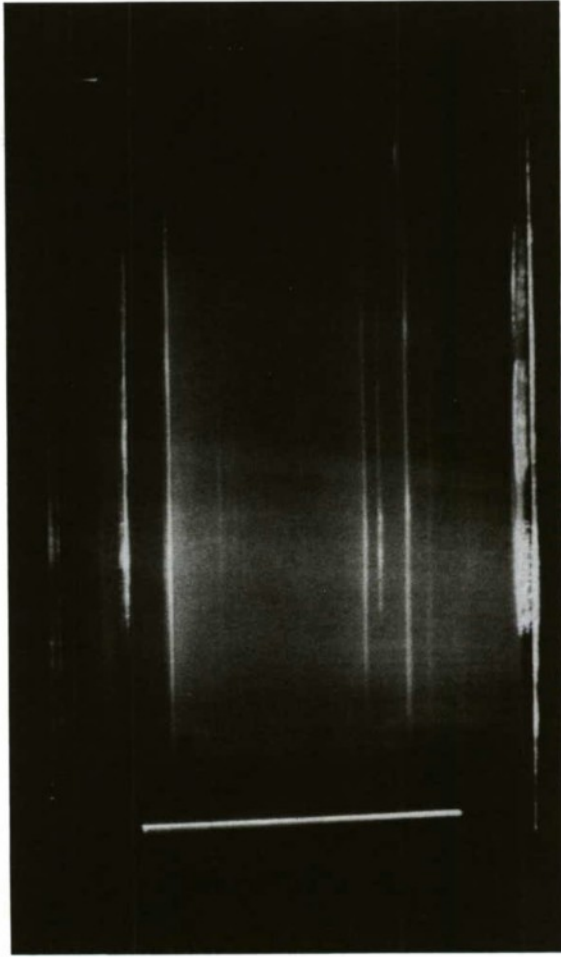


Figure 3-5. Flow pattern for gas injection through a porous plug. The vertical streaks are reflections from the tube.

75607-19

75607-18

The effect of heating the susceptor disk was studied for gas injection at 10 lpm through the porous plug. A steady-state pattern observed at 1 atm for a disk temperature of 600°C is shown in Figure 3-6. Because of thermal convection, the flow is very complicated. All evidence of thermal convection disappeared when the pressure was lowered below 0.3 atm, and laminar flows like those observed at room temperature were sustained.

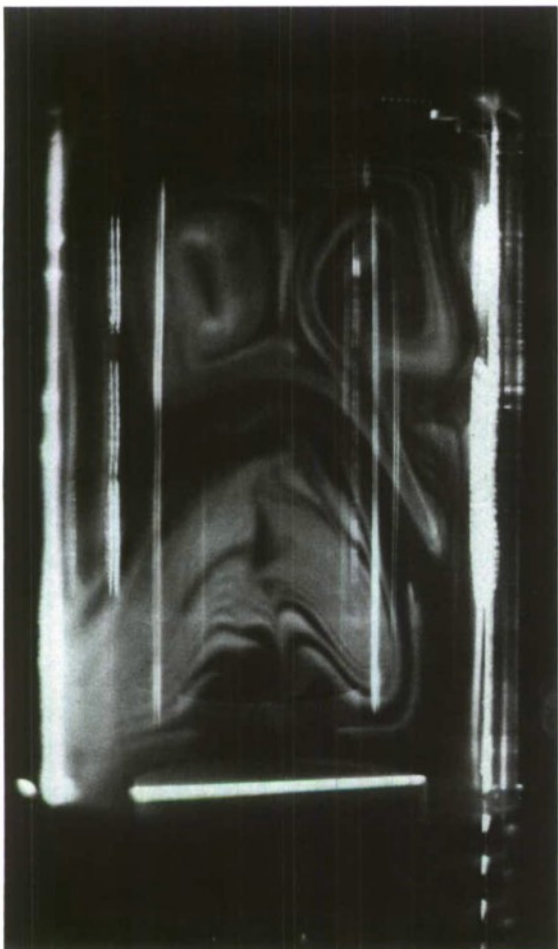


Figure 3-6. Flow pattern for gas injection through porous plug for disk temperature of 600°C.

75607-20

In other experiments using injection through the porous plug but with the susceptor disk at room temperature, we investigated the effect of switching from one injected gas to another of different density. At atmospheric pressure such switching can produce transient flow patterns, similar in complexity to those obtained by thermal convection, that persist for many seconds before uniform flow is restored. In a typical experiment, a stream of He gas containing TiO₂ particles was injected into the reactor tube at a constant rate of 10 lpm. An additional 60-ccpm He stream was injected into the reactor through the switching manifold (see Figure 3-1), which has very low

deadspace, and a 60-ccpm flow of N₂ was simultaneously directed through the manifold to a vent line (not shown in Figure 3-1). After the flow became uniform, as shown by the observation of a pattern similar to that in Figure 3-5, the two 60-ccm flows were interchanged, with the He directed to the vent and the N₂ injected into the reactor tube. After a few seconds (the transit time between the manifold and the reactor), a pattern comparable to that in Figure 3-6 was developed. The pattern varied with time, again becoming uniform after about 30 s.

Instabilities of the type described result from convection that takes place during the period following switching when the composition of the gas in the tube has not yet become uniform, if the gas density increases with increasing distance from the bottom of the tube. We estimate that such instabilities will occur in our test system when switching produces an increase of about 5 percent or more in the density of the gas mixture injected into the reactor. In the growth of III-V epilayers, the density changes resulting from the switching of Group III organometallic compounds are generally less than 5 percent. However, significantly larger changes can result from switching the Group V hydrides. For example, to grow In_{0.47}Ga_{0.53}As on InP under typical growth conditions, the required switch from PH₃ to AsH₃ would increase the injected gas density by about 15 percent. In a reactor of the design used in our tests, a change of this magnitude might be expected to produce instabilities that would result in the formation of a graded interface. It should be possible to minimize such instabilities, as well as those due to thermal convection, by operation at reduced pressure.

C.A. Wang
S.C. Palmateer
S.H. Groves

3.2 MONOLITHIC GaAs/AlGaAs DIODE-LASER/DEFLECTOR DEVICES

Considerable effort is currently being directed toward the development of semiconductor diode laser arrays. Although most of this effort is devoted to linear arrays of edge-emitting GaAs/AlGaAs lasers, two-dimensional arrays will be needed to meet the power and area requirements for such applications as the pumping of large solid-state lasers. Composite two-dimensional arrays could be fabricated by stacking and joining separate linear arrays of edge-emitting diode lasers. An attractive alternative is to form monolithic arrays of devices that emit laser radiation normal to the wafer surface. Several types of surface-emitting GaAs/AlGaAs and GaInAsP/InP diode lasers have been reported, but their efficiencies are too low to be of practical interest.

A more promising approach to the fabrication of monolithic two-dimensional arrays is to use devices formed by coupling edge-emitting diode lasers with external mirrors that deflect the radiation from one or both of the laser facets by 90°. Liau and Walpole¹ have recently demonstrated monolithic diode-laser/deflector (MLD) devices that combine a GaInAsP/InP laser with a parabolic 45° deflector adjacent to one facet. The deflector and both facets are formed by a mass transport process.² Unfortunately, such a mass transport process is not known for AlGaAs. We report here the use of an ion-beam-assisted-etching (IBAE) technique³ to fabricate GaAs/AlGaAs MLD devices with a planar 45° deflector adjacent to one of the laser facets.

The MLD devices were fabricated on a wafer with an AlGaAs/GaAs/AlGaAs double heterostructure prepared by using organometallic chemical vapor deposition⁴ on a (100) Si-doped GaAs substrate. The fabrication procedure is shown schematically in Figure 3-7. The IBAE technique was used to etch grooves 2 μm wide, on 400- μm centers, parallel to a (110) cleavage plane. Pyrolytically deposited phosphosilicate glass (PSG) served as an etch mask during this procedure. The PSG was then removed with buffered HF, and another layer of PSG was deposited to cover the top surface of the wafer as well as the bottom and vertical sidewalls of the grooves [Figure 3-7(a)]. Windows 2.5 μm wide were opened in the PSG immediately adjacent to the grooves [Figure 3-7(b)]. The deflectors [Figure 3-7(c)] were formed by IBAE carried out with the wafer mounted at an angle of 45° with respect to the incident ion beam. Next, 4- μm -wide stripe contact windows on 250- μm centers, oriented normal to the grooves, were opened in the PSG over the full length of the wafer. The wafer was thinned to ~75 μm , and AuSn was deposited on the substrate side to provide the n contact. A film of CrAu was deposited by angle evaporation on the top side to coat the deflectors and provide the p contacts through the 4- μm stripe windows [Figure 3-7(d)]. The wafer was cleaved into bars, each containing a single row of diode lasers with one cleaved facet and one etched facet, together with a 45° deflector adjacent to the etched facet [Figure 3-7(d)]. The bars were diced into samples containing from one to five MLD devices.

Samples with laser cavity lengths from 125 to 390 μm were evaluated during pulsed (60-ns, 4-kHz) operation at low output power. Figure 3-8 shows the light vs current curves for the optical output emitted from (a) one of the two cleaved facets of a reference laser from the same wafer used for MLD devices, (b) the cleaved facet of an MLD device, and (c) the 45° deflector of the same device. In comparison to state-of-the-art GaAs/AlGaAs diode lasers, the reference laser has a higher threshold current and lower efficiency because the material quality is lower and the simplest type of double heterostructure was used in these initial experiments. The threshold current is higher for the MLD laser than for the reference laser because the etched facet is inferior to the cleaved facets.

The near-field emission normal to the surface of samples with multiple MLD devices was observed with a densitometric infrared camera. Figure 3-9 shows the intensity profile for a sample containing five devices with a laser cavity length of 125 μm . At this current level, all the devices were operating at about twice threshold with very similar output intensities.

In order to obtain MLD devices suitable for two-dimensional arrays, several design modifications will be needed. The lasers must obviously have two etched facets. Preferably, each facet should have an adjacent deflector; to focus the radiation emitted normal to the surface, the deflectors should be parabolic rather than planar. In addition, significant changes will be required in the processing procedures. The principal reason for the reduction in performance of the MLD devices compared with the reference lasers is the surface roughness of the etched facets and deflectors, which exhibit vertical striations produced mainly because the PSG etch masks did not have smooth edges. It should be possible to obtain much smoother surfaces by improving the masks and optimizing the IBAE process parameters. We believe that it will be feasible to obtain MLD devices comparable in performance to state-of-the-art edge-emitting GaAs/AlGaAs lasers. There

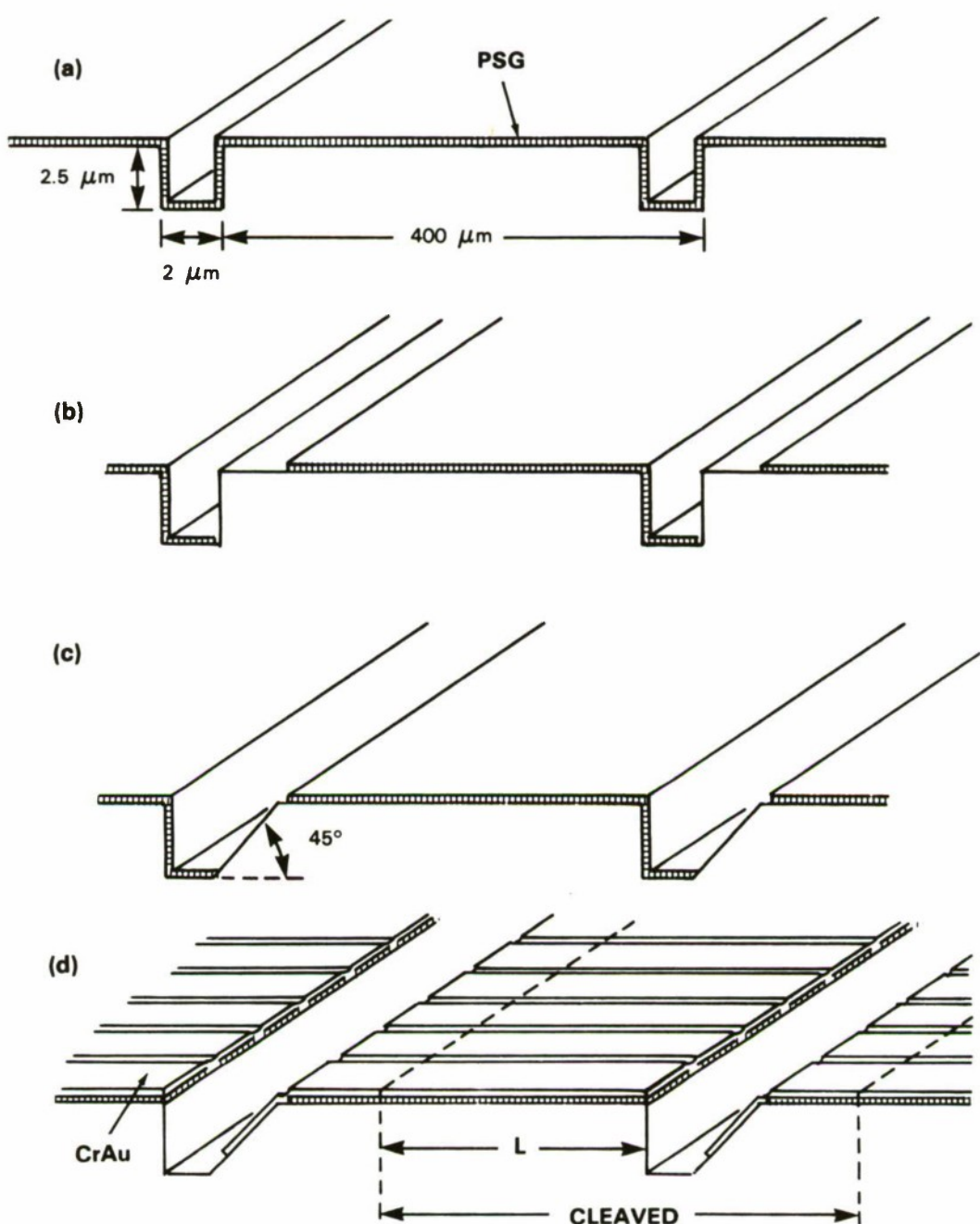


Figure 3-7. Procedure for fabricating monolithic GaAs/AlGaAs diode-laser/deflector (MLD) devices.

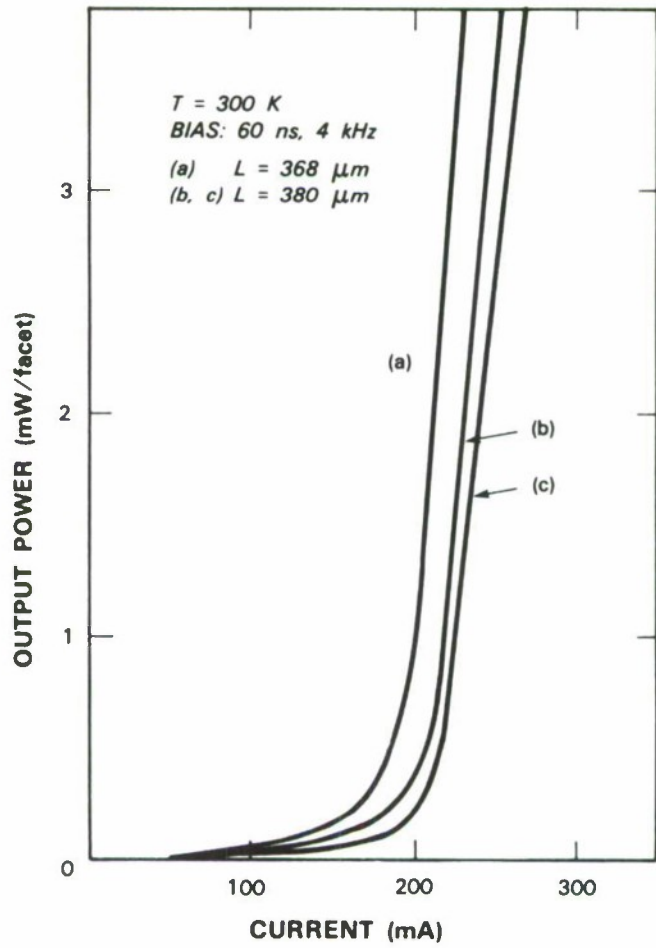


Figure 3-8. Light output vs pulsed drive current for (a) reference laser with two cleaved facets, (b) cleaved facet of MLD device, (c) deflector of the same MLD device.

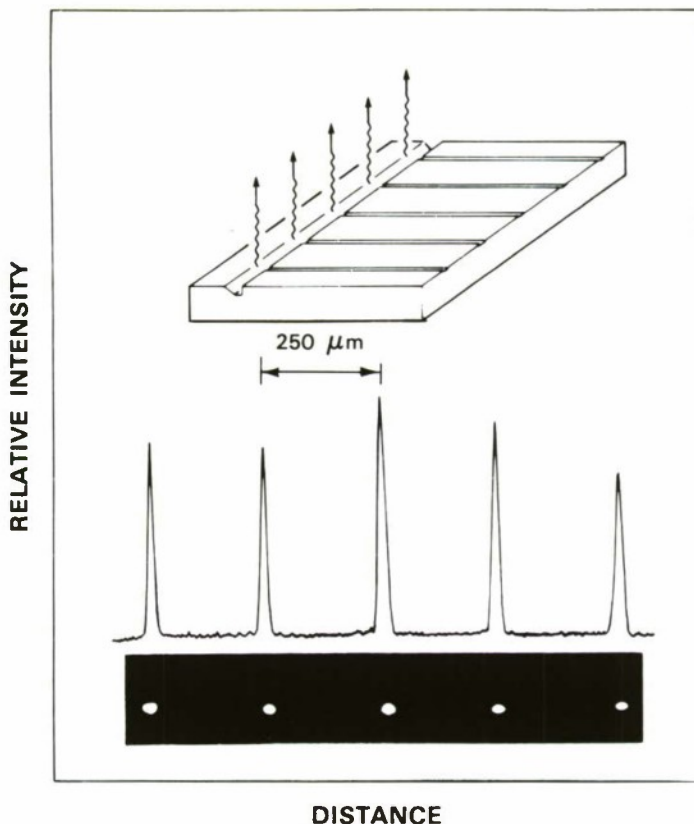


Figure 3-9. Intensity of near-field emission normal to the surface of a sample containing five MLD devices.

should be no difficulty in fabricating such MLD devices with sufficient packing density to obtain high-power-density monolithic two-dimensional arrays.

T.H. Windhorn
W.D. Goodhue

3.3 MONOLITHIC INTEGRATION OF GaAs/AlGaAs LEDs AND Si MOSFETs

Monolithic GaAs/Si (MGS) integration is attractive because Si VLSI circuits can be complemented by GaAs/AlGaAs optoelectronic components and high-speed electronic circuits. We recently demonstrated the fabrication, on the same MGS wafer, of GaAs MESFETs and Si MOSFETs with characteristics comparable to those of devices fabricated on separate GaAs and Si wafers.⁵ We report here the monolithic integration of GaAs/AlGaAs double-heterostructure

LEDs and Si MOSFETs on an MGS wafer prepared by using molecular beam epitaxy to grow GaAs/AlGaAs layers on a Si substrate.

Figure 3-10 is a schematic diagram of the device structure in cross section. Each LED is surrounded by a ring-type MOSFET. The cathode of the LED is in contact through the Si substrate with the drain of the MOSFET, so that the two devices are connected in series. This is the first time that GaAs and Si devices have been interconnected monolithically. An LED modulation rate of 10 MHz has been achieved by applying a stream of voltage pulses to the MOSFET gate.

The sequence of processing steps is as follows. A layer of thermal oxide is grown on a 1- to 3- Ω -cm p Si wafer oriented 3° off (100) toward (111). The SiO_2 is etched to form openings of $200 \times 400 \mu\text{m}$ where LEDs are to be fabricated. A high dose of arsenic ions is implanted to form n⁺ islands by converting the surface of the Si within the openings. Around each n⁺ island, a standard poly-Si gate process is used to fabricate a Si MOSFET, except for contact openings and final metallization. The MOSFET drain is in contact with the n⁺ island. Chemical vapor deposition is used to cover the entire wafer with successive layers of SiO_2 and Si_3N_4 to protect the MOSFET structures during GaAs epitaxy and subsequent LED processing.

Openings are etched in the $\text{Si}_3\text{N}_4/\text{SiO}_2$ to expose the n⁺ Si islands. Molecular beam epitaxy is employed to deposit the following series of layers for the LEDs: 3- μm n⁺ GaAs buffer, 0.5- μm n Al_{0.3}Ga_{0.7}As, 0.4- μm p GaAs active, 0.5- μm p Al_{0.3}Ga_{0.7}As, and 0.25- μm n⁺ GaAs cap. The material grown on the bare Si islands is monocrystalline, while that on the $\text{Si}_3\text{N}_4/\text{SiO}_2$ is polycrystalline. The polycrystalline material is removed by etching. Octagonal mesas for LEDs are formed in the monocrystalline GaAs/AlGaAs islands by etching down to the n⁺ GaAs buffer. Plasma-enhanced chemical vapor deposition is used to deposit SiN_x over the entire wafer. Contact openings for both MOSFETs and LEDs are etched in the nitride/oxide layer. Metallization is performed by evaporating Al on the MOSFETs and Ni/Ge/Au and Cr/Au, respectively, on the cathode and anode of the LEDs. Contacts to the MOSFET drain and LED cathode, although not utilized in joint operation of the two devices, are made in order to permit the characteristics of each device to be measured separately.

Figure 3-11 is an optical micrograph showing a completed GaAs/AlGaAs LED surrounded by a Si MOSFET. The MGS MOSFETs have normal transistor characteristics, which are about the same as the characteristics of control MOSFETs fabricated on a separate Si wafer.

The MGS LEDs have negligible leakage current and a breakdown voltage of about 16 V, the same as the value obtained for control devices fabricated on a GaAs substrate. At low forward bias voltages, both the MGS and control LEDs have an ideality factor close to 2, indicating that recombination is the dominant mechanism of current flow. However, at a given bias voltage the current is about 50 times higher for the MGS devices than for the control devices. This implies that the minority carrier lifetime is much shorter for the MGS GaAs/AlGaAs layers than for the control layers.

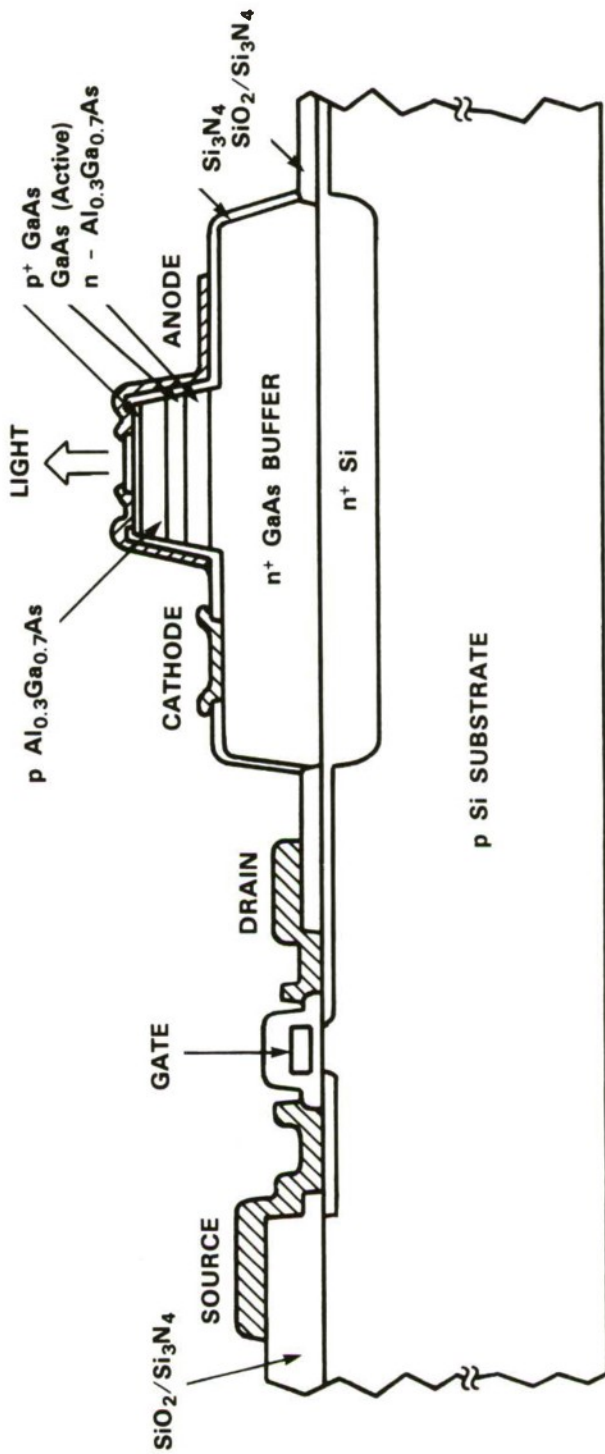


Figure 3-10. Schematic cross-sectional diagram of a monolithically integrated Si MOSFET and GaAs/AlGaAs LED. (The portion of the MOSFET to the right of the LED is not shown.)

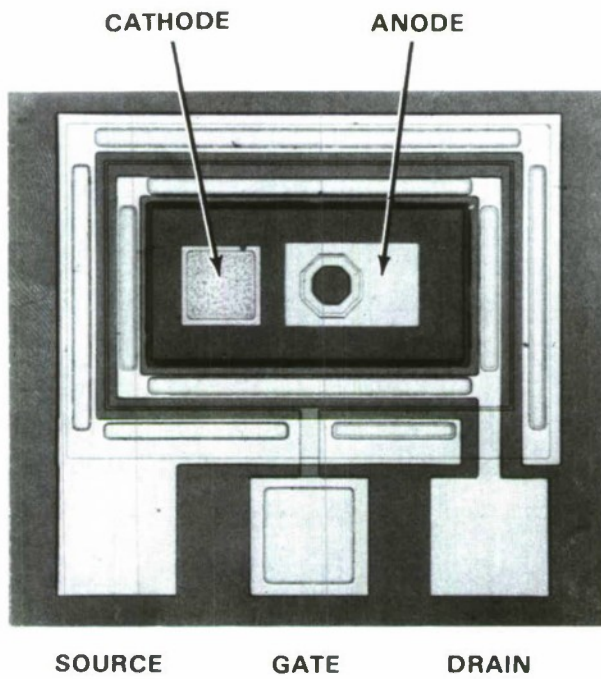


Figure 3-11. Optical micrograph of a GaAs/AlGaAs LED and the surrounding Si MOSFET.

Figure 3-12 shows the light output vs dc current characteristic for an MGS LED. At 100 mA the output is about $6.5 \mu\text{W}$, which is 10 to 15 percent of the output from control devices. The MGS LEDs have a nonuniform near-field pattern with many dark spots, while the pattern for the control LEDs is uniform.

To investigate the modulation of the MGS LED, a stream of voltage pulses was applied to the MOSFET gate with the LED anode biased at 5 V. Figure 3-13(a-b) shows the waveforms of the gate voltage pulses, LED current, and light output. At a pulse repetition rate of 5 MHz, the light output pulses are widely separated. At a rate of 10 MHz, there is not much separation between them. Although the light output closely follows the current, there is considerable delay and distortion in the current waveform compared with the voltage waveform. It can be concluded that the modulation rate is limited not by the carrier lifetime of the LED but by the speed of the Si MOSFET in charging and discharging the drain/cathode capacitance. It should be possible to achieve much higher modulation rates by scaling down the MOSFET dimensions, reducing the LED series resistance, and reducing the drain/cathode capacitance.

H.K. Choi
G.W. Turner

T.H. Windhorn
B-Y. Tsaur

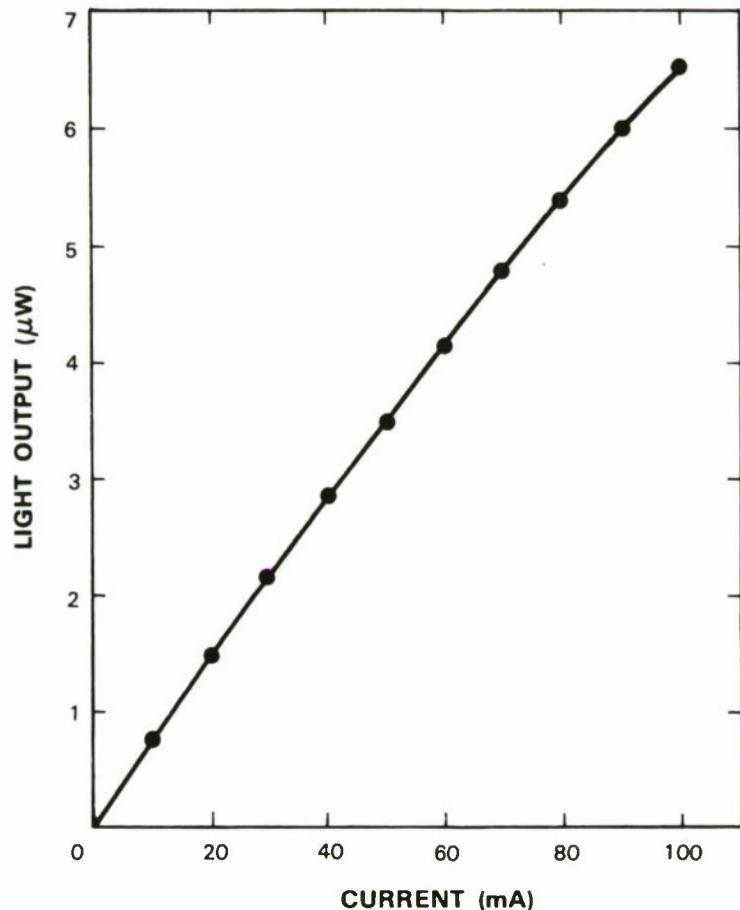
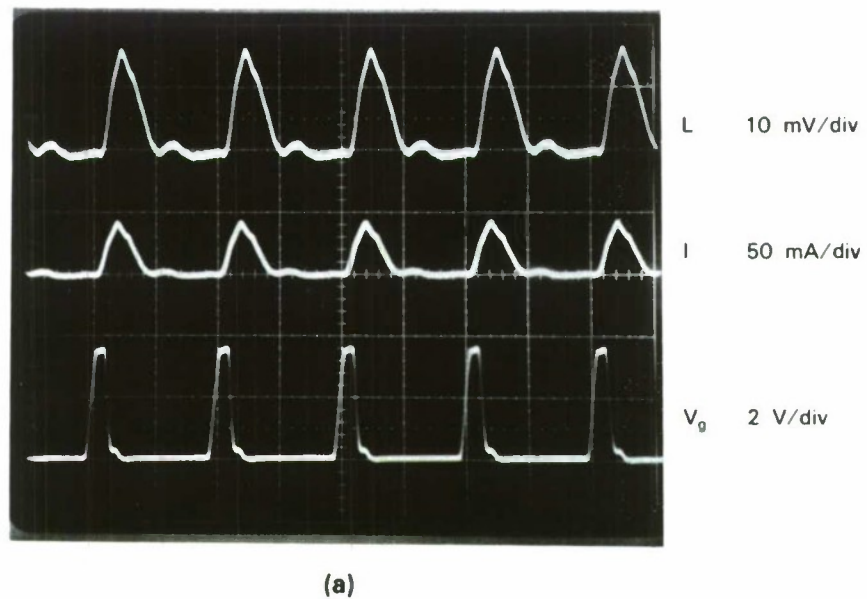
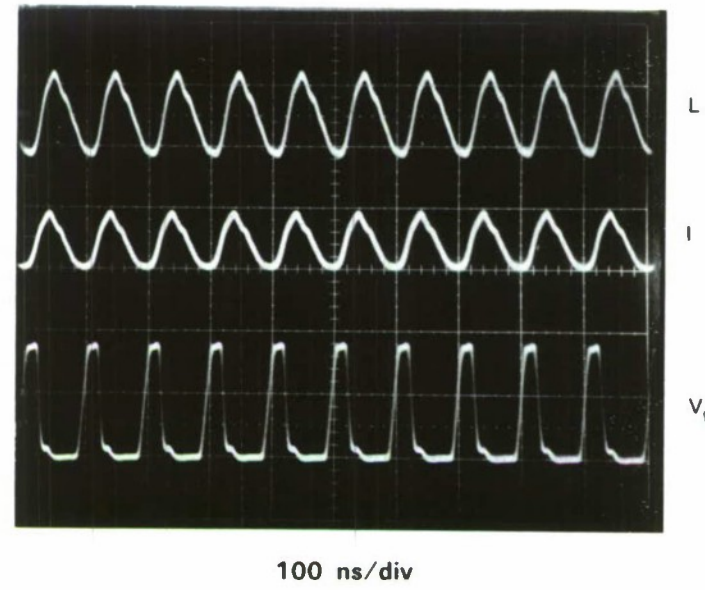


Figure 3-12. Light output vs current characteristic of an MGS LED.



(a)



100 ns/div

(b)

74217.3

Figure 3-13. Modulation characteristics of an MGS LED at (a) 5 MHz and (b) 10 MHz. The bottom, middle, and top traces are the waveforms of the gate voltage, current, and light output, respectively.

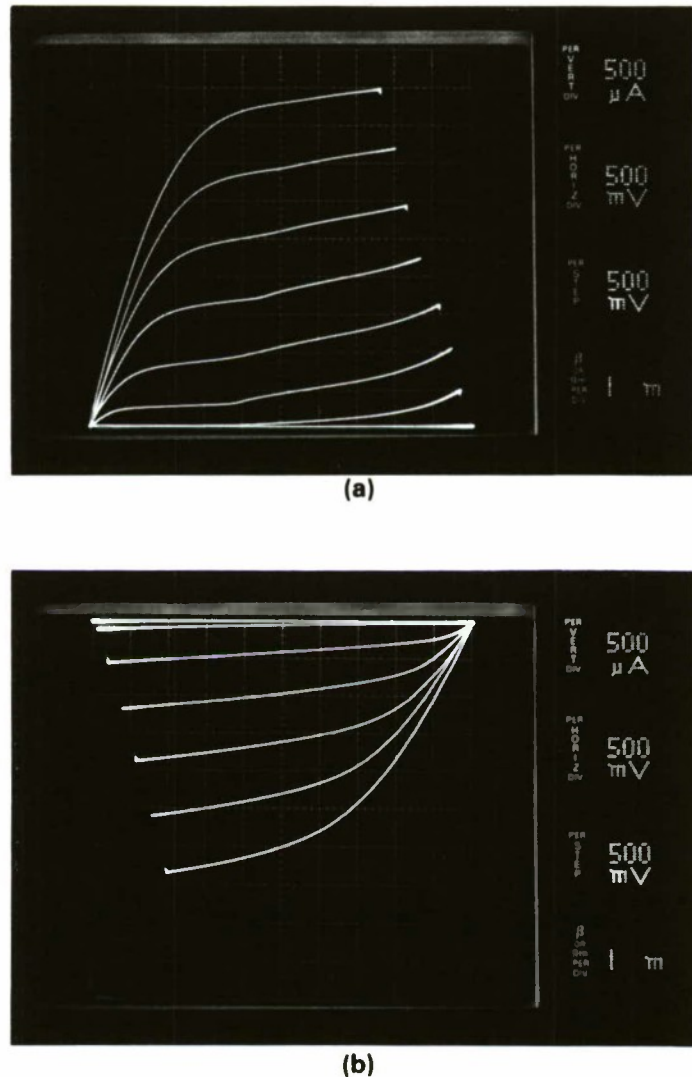


Figure 3-14. Current-voltage characteristics of (a) n-channel device with $L_{eff} = 0.8 \mu m$, and (b) p-channel device with $L_{eff} = 0.7 \mu m$.

3.4 SUBMICROMETER CMOS DEVICES IN ZONE-MELTING-RECRYSTALLIZED SOI FILMS

Extensive efforts are currently being directed toward the development of silicon-on-insulator (SOI) technologies for VLSI applications. Using zone-melting-recrystallized (ZMR) SOI films prepared by the graphite-strip-heater technique,⁶ in which subboundaries (low-angle grain boundaries) are the principal defects, we have recently fabricated fully functional CMOS 1K static RAMs and 1.2K gate arrays with good operating characteristics. Subboundaries apparently have no significant impact on the operation of these circuits, which have minimum feature sizes of 3 to 4 μm . However, there has been concern that subboundaries may degrade the characteristics of devices with submicrometer dimensions. One possibility is that enhanced dopant diffusion could occur along the subboundaries, causing an increase in transistor leakage current and even shorting between source and drain.

In the present work we have used a conventional poly-Si gate process to fabricate submicrometer CMOS transistors and 39-stage ring oscillators in 0.3- μm -thick SOI films prepared by ZMR on Si substrates coated with a 1.5- μm -thick SiO_2 layer. Low-temperature processing was employed to minimize enhanced dopant diffusion along subboundaries. Good device characteristics have been obtained, although the threshold-voltage variation is greater than for bulk Si control devices. The LOCOS process was used for device isolation. The devices have n^+ poly-Si gate electrodes and source and drain regions formed by ion implantation followed by annealing at temperatures below 850°C. The gate oxide thickness is 25 nm, and the gate widths for n- and p-channel devices are 25 and 40 μm , respectively. For comparison, control devices of the same design were fabricated in bulk Si.

Figure 3-14(a-b) shows the current-voltage characteristics of n- and p-channel SOI devices with effective channel lengths of 0.8 and 0.7 μm , respectively. Both devices have well-behaved characteristics. Their maximum field effect mobilities are 550 and 260 $\text{cm}^2/\text{V}\cdot\text{s}$, respectively, which are comparable to the values for the bulk Si control devices. The effective channel length (L_{eff}) is equal to the nominal source-drain spacing minus the distance of lateral dopant diffusion between the source and drain. The diffusion distance has been found by measuring the characteristics of transistors with the same gate width but various gate lengths. The diffusion distances for the n- and p-channel SOI devices are 0.4 and 0.5 μm , respectively. These values, although larger than the values of 0.3 and 0.35 μm measured for the corresponding control devices, are not sufficient to cause significant degradation of the transistor characteristics.

Figure 3-15 shows the subthreshold current-voltage characteristics of typical n- and p-channel transistors with various values of L_{eff} . The leakage currents are less than 0.1 $\text{pA}/\mu\text{m}$ channel width, nearly independent of L_{eff} . The dependence of threshold voltage on L_{eff} is shown in Figure 3-16. The decrease in threshold voltage with decreasing L_{eff} , the so-called short-channel effect, is small for both n- and p-channel devices.

To assess threshold-voltage uniformity, measurements were made on transistors randomly selected from a 3-in wafer. The threshold voltage distributions for 62 n-channel and 62 p-channel

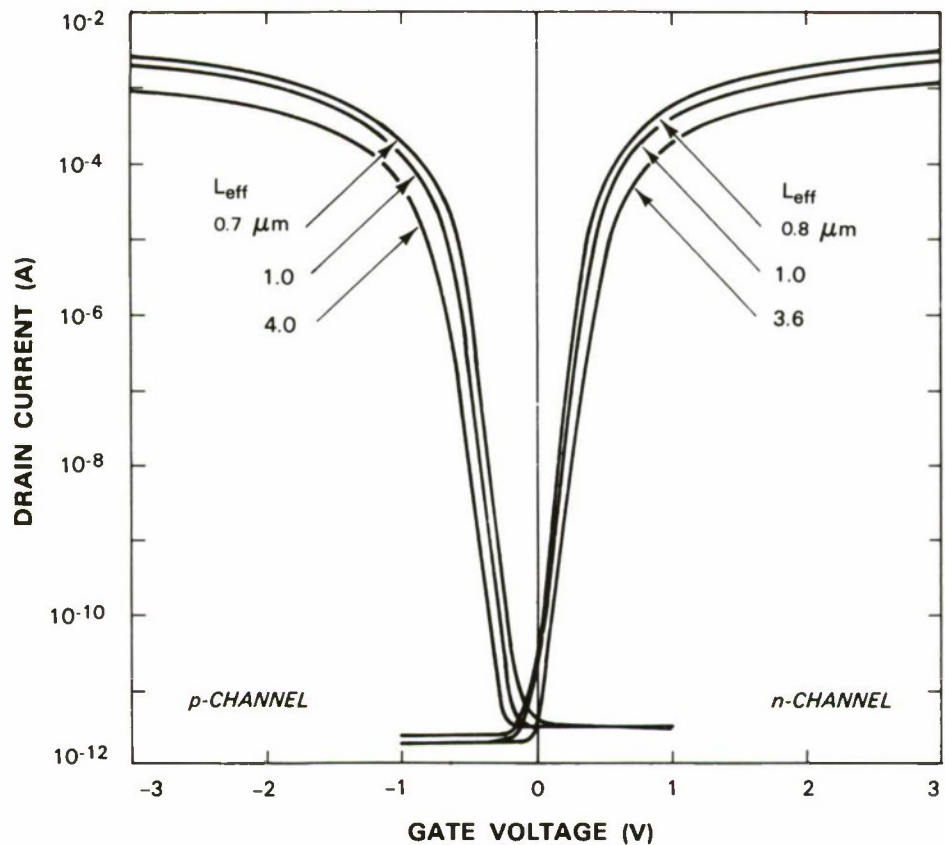


Figure 3-15. Subthreshold current-voltage characteristics of n- and p-channel devices with various values of L_{eff} . The drain bias voltages are +3 and -3 V, respectively.

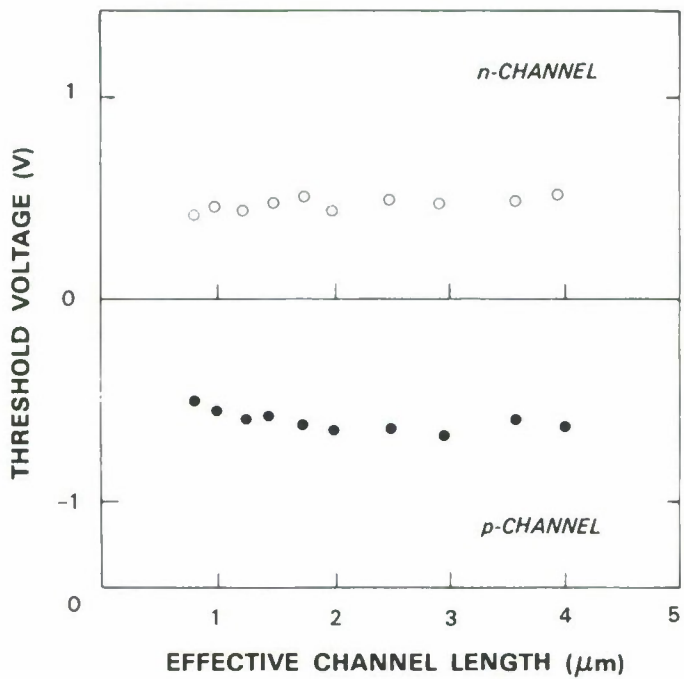


Figure 3-16. Threshold voltage vs effective channel length for *n*- and *p*-channel devices.

devices with $L_{\text{eff}} = 1.2 \mu\text{m}$ are shown in Figures 3-17(a) and (b), respectively. For each type of device the standard deviation is 38 mV, about twice the value observed for the bulk Si control devices. The increase in threshold voltage variation may have resulted from the presence of sub-boundaries in the SOI film. For many digital circuits operated with a 5-V supply voltage, the observed variation would be quite acceptable. For submicrometer VLSI circuits requiring lower supply voltages, however, the variation would need to be decreased.

Figure 3-18(a) shows the output waveform of a 39-stage SOI ring oscillator ($L_{\text{eff}} = 0.8 \mu\text{m}$, fan in/out = 1) for a supply voltage of 5 V. The propagation delay per stage is 95 ps. In Figure 3-18(b), the propagation delay is plotted as a function of supply voltage for three ring oscillators with different values of L_{eff} . The delay times are 30- to 40-percent smaller than those of bulk Si control devices. The higher speed of the SOI devices is attributed to the reduced parasitic capacitance of the SOI structure.

Submicrometer CMOS devices have recently been fabricated in SOI materials prepared by oxidation of porous Si (Reference 7), laser recrystallization,⁸ and oxygen implantation,⁹ and also in improved SOS material.¹⁰ The submicrometer devices that we have fabricated in ZMR SOI films are generally comparable in performance to those fabricated in the other materials, although direct comparisons are not feasible because of differences in device processing and dimensions. However, the source-drain diffusion and threshold-voltage variation are greater for the ZMR devices, probably because of the presence of subboundaries. By improving the ZMR

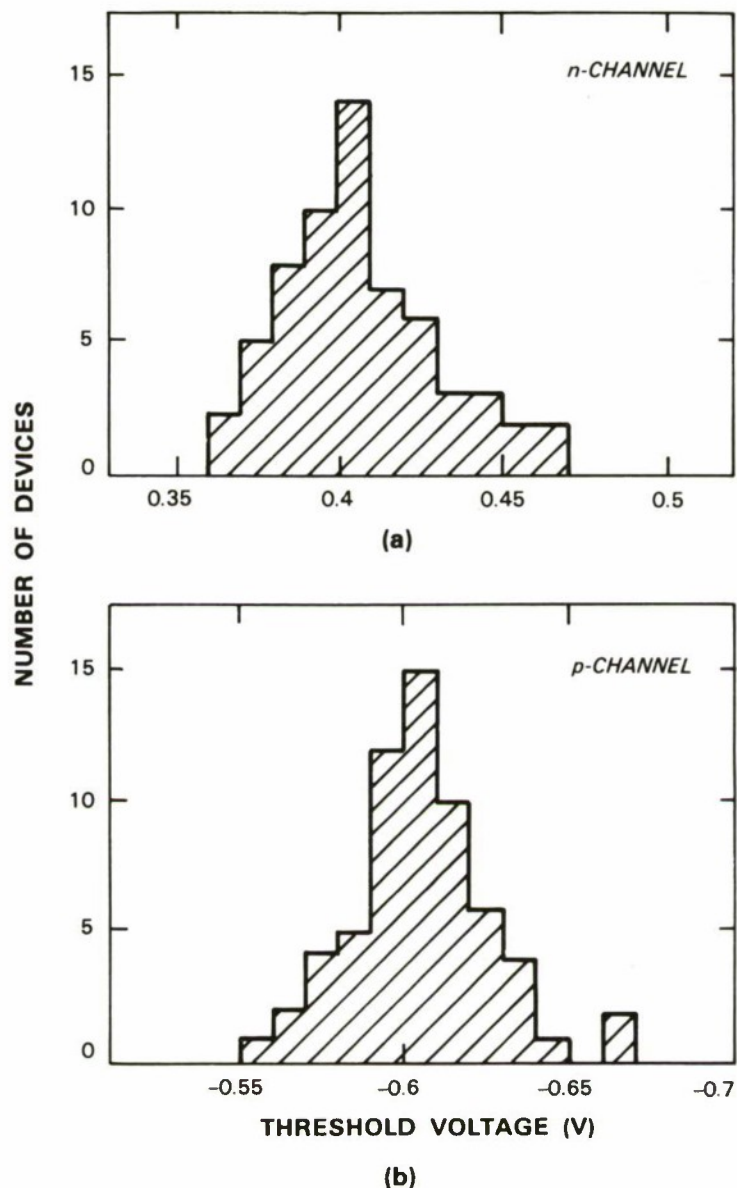
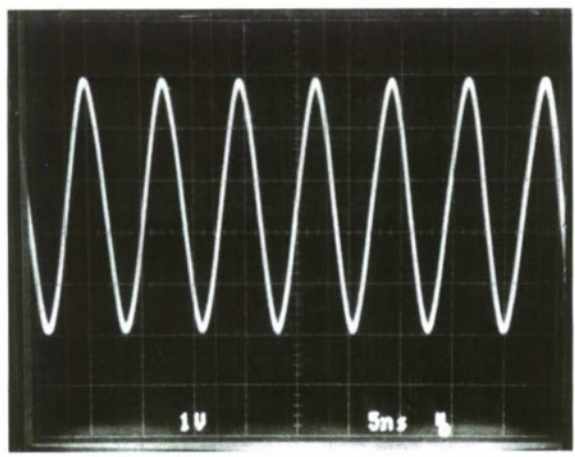
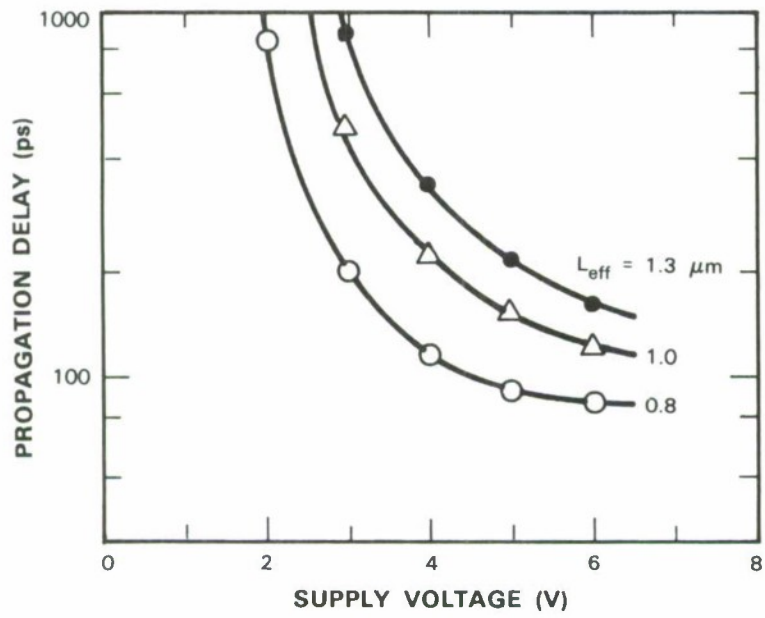


Figure 3-17. Threshold voltage distributions for (a) n- and (b) p-channel devices with $L_{eff} = 1.2 \mu m$. The standard deviation is 38 mV for both types of devices.



(a)



(b)

Figure 3-18. (a) Output waveform of 39-stage ring oscillator with $L_{eff} = 0.8 \mu m$ at a supply voltage of 5 V. (b) Propagation delay as a function of supply voltage.

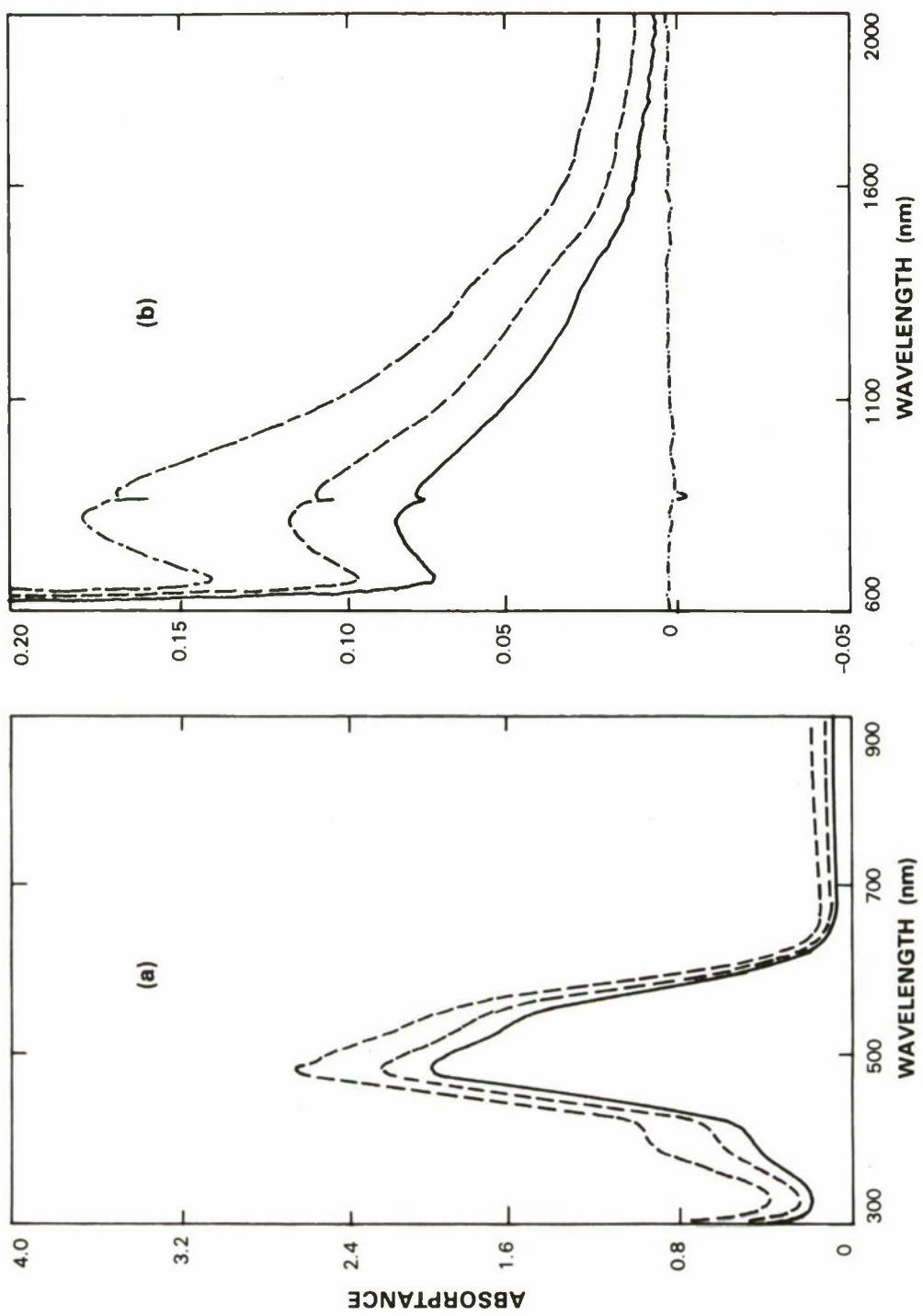


Figure 3-19. Absorptance spectra for light polarized parallel to the c (optic) axis at three locations along the length of a $\text{Ti:Al}_2\text{O}_3$ crystal. (a) Ti^{3+} absorption band; (b) residual infrared absorption band, plotted on an expanded absorptance scale.

processing technique, we have recently obtained ZMR films with large subboundary-free areas.¹¹ We anticipate that devices fabricated in subboundary-free ZMR films will be fully adequate for high-performance integrated circuits.

B-Y. Tsaur
C.K. Chen

3.5 RESIDUAL INFRARED ABSORPTION IN Ti:Al₂O₃ CRYSTALS

The performance of Ti:Al₂O₃ lasers is generally impaired by an infrared absorption of unknown origin that occurs in the laser output wavelength region. We have previously described¹² a gradient-freeze technique for growing Ti:Al₂O₃ crystals with sufficiently low residual absorption to permit the fabrication of lasers exhibiting room-temperature CW operation over a tuning range between 693 and 948 nm (see Section 2.1 on p. 9). In this report we present data relating the intensities of the residual absorption and the absorption due to the Ti³⁺ laser ions. These data support a model¹³ that attributes the residual absorption to Ti³⁺-Ti⁴⁺ pairs.

Measurements of absorptance ($-\log I/I_o$, where I is the transmitted intensity and I_o the incident intensity) as a function of wavelength for light polarized parallel to the c (optic) axis have been made with a spectrophotometer at a number of positions along the length of polished longitudinal sections cut from two as-grown Ti:Al₂O₃ crystals. Figure 3-19(a) shows the spectra obtained for the Ti³⁺ absorption band at three positions on Crystal A. The absorptance increases with increasing distance from the seed end because the Ti³⁺ concentration increases in this direction. Figure 3-19(b) shows the corresponding spectra for the residual band, which are plotted on a greatly expanded intensity scale. The residual intensity also increases with distance from the seed end. These results have been used to obtain the data shown as open triangles in Figure 3-20, where the absorption coefficient (α_{res}) at 900 nm in the residual absorption band is plotted on a log-log scale against the coefficient (α_{max}) at 485 nm, the peak of the Ti³⁺ band. The data obtained from spectrophotometer measurements at five positions on a section from Crystal B are shown as open circles. The data fit two parallel straight lines, one for each crystal, with a slope of 2. For a given value of α_{max} , the value of α_{res} is about 60-percent greater for Crystal A than for Crystal B. For a laser rod cut from a crystal designated as C, α_{max} was found by spectrophotometer measurements, and an upper limit was found for the residual absorption at 770 nm by analyzing the laser threshold and slope efficiency to determine the round-trip cavity loss.¹⁴ The point obtained in this manner, represented by the open square in Figure 3-20, falls close to the straight line obtained for Crystal B. For this sample, α_{res} is less than 1 percent of α_{max} .

In a recent study we have shown that α_{max} is proportional to the Ti³⁺ concentration, which was determined by measuring the magnetization of Ti:Al₂O₃ samples as a function of temperature and magnetic field.¹⁴ The data of Figure 3-20 therefore show that α_{res} increases linearly with the square of the Ti³⁺ concentration. This relationship indicates that the residual absorption is due to an absorbing species composed of two members, one of which might be a Ti³⁺ ion. The possibility that the absorbing species is a Ti³⁺-Ti³⁺ pair is ruled out because in this case α_{res}

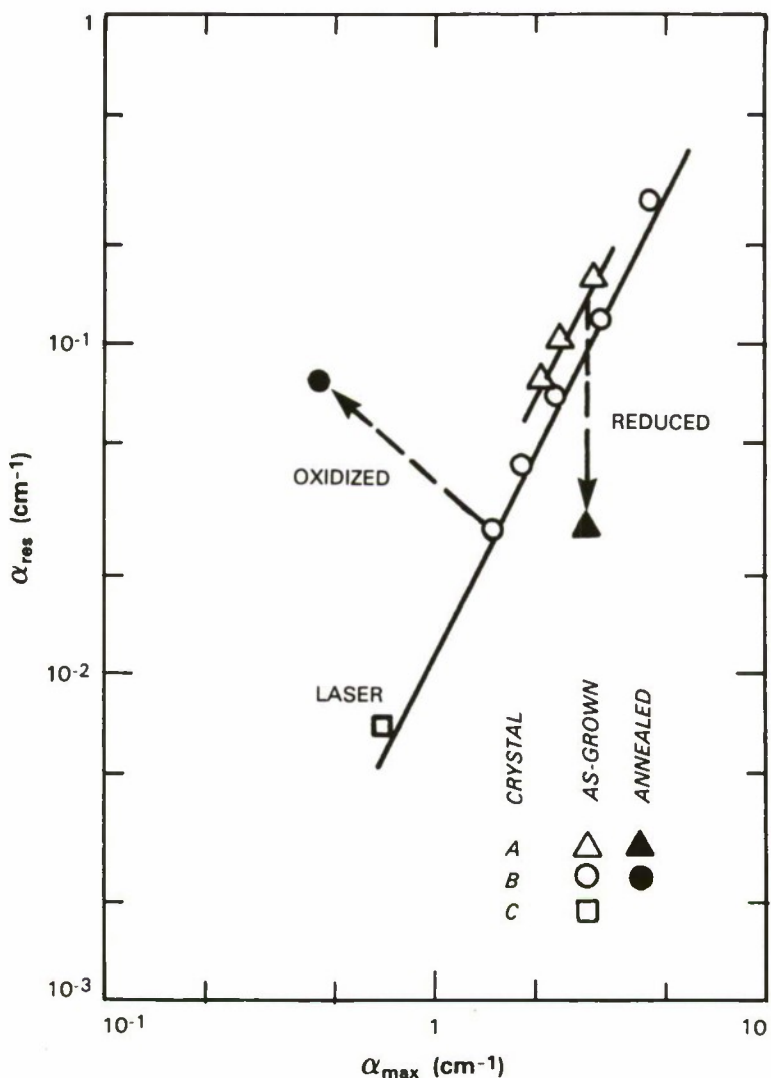


Figure 3-20. Residual absorption at 900 nm (α_{res}) vs Ti^{3+} absorption at 485 nm (α_{max}) for $Ti:Al_2O_3$ crystals.

would be a single-valued function of α_{max} . This prediction is inconsistent with the difference observed between the sets of data for the as-grown Crystals A and B, and even more so with the results shown in Figure 3-20 for two annealed samples. One of these, cut from Crystal B, was annealed in Ar gas containing 10-ppm O₂. This treatment decreased α_{max} by more than a factor-of-3 while increasing α_{res} by almost as much. The other sample, from Crystal A, was annealed in Ar gas containing about 15-percent H₂, causing α_{res} to decrease by almost a factor-of-6 without a significant change in α_{max} .

The data of Figure 3-20 suggest that the residual absorption is due to Ti^{3+} - Ti^{4+} pairs, as proposed by Jorgenson.¹³ In this case, α_{res} will be proportional to $(\alpha_{\text{max}})^2$ as long as the $\text{Ti}^{3+}/\text{Ti}^{4+}$ concentration ratio is constant. According to this model, the difference between the results for as-grown Crystals A and B can be attributed to a difference in their $\text{Ti}^{3+}/\text{Ti}^{4+}$ ratios. For a fixed total concentration of Ti ions, α_{res} will have its maximum value when the Ti^{3+} and Ti^{4+} concentrations are equal, and it will disappear when either Ti^{3+} or Ti^{4+} becomes zero. We believe that for our as-grown crystals the fraction of Ti^{3+} ions is not far from one. In this case, partial oxidation of Ti^{3+} ions to Ti^{4+} ions, while reducing α_{max} , can increase the concentration of Ti^{3+} - Ti^{4+} pairs and therefore increase α_{res} , as observed for the sample that was annealed in Ar-O₂. On the other hand, partial reduction of the Ti^{4+} ions to Ti^{3+} ions can produce a significant reduction in pair concentration, and therefore in α_{res} , without a significant increase in Ti^{3+} concentration and α_{max} , as observed for the sample that was annealed in Ar-H₂. We are carrying out additional annealing experiments in order to test the Ti^{3+} - Ti^{4+} pair model. Regardless of the mechanism, the substantial reduction in residual absorption achieved by Ar-H₂ annealing should result in significantly improved laser performance.

A. Sanchez
R.E. Fahey

A.J. Strauss
R.L. Aggarwal

REFERENCES

1. Z.L. Liau and J.N. Walpole, *Appl. Phys. Lett.* **46**, 115 (1985), DTIC AD-A151425.
2. Z.L. Liau, J.N. Walpole, and D.Z. Tsang, *Appl. Phys. Lett.* **44**, 945 (1984), DTIC AD-A147996.
3. G.A. Lincoln, M.W. Geis, S. Pang, and N.N. Efremow, *J. Vac. Sci. Technol. B* **1**, 1043 (1983), DTIC AD-A147828.
4. Spire Corporation, Bedford, Massachusetts.
5. H.K. Choi, G.W. Turner, and B-Y. Tsaur, *IEEE Electron Device Lett.* **EDL-7**, 241 (1986).
6. C.K. Chen, M.W. Geis, H.K. Choi, B-Y. Tsaur, and J.C.C. Fan, in Proc. Symposium on Energy Beam-Solid Interactions and Transient Thermal Processing, MRS Fall Meeting, 1984, p. 613.
7. K. Anzai, F. Otoi, M. Ohnishi, and H. Kitabayashi, *IEDM Technical Digest* (1984), p. 796.
8. A.J. Auberton Herve, J.P. Joly, P. Jeuch, J. Gautier, and J.M. Hode, *IEDM Technical Digest* (1984), p. 808.
9. K. Hashimoto, T.I. Kamins, K.M. Cham, and S.Y. Chiang, *IEDM Technical Digest* (1985), p. 672.
10. D.C. Mayer, P.K. Vasudev, A.E. Schmitz, and R.E. Kastris, *IEDM Technical Digest* (1985), p. 676.
11. Solid State Research Report, Lincoln Laboratory, MIT (1986:1), pp. 15-16; *Appl. Phys. Lett.* (to be published).
12. *Ibid.* (1985:4), pp. 19-21.
13. C.K. Jorgenson, quoted by P.F. Moulton, *J. Opt. Soc. Am. B* **3**, 125 (1986).
14. R.L. Aggarwal, A. Sanchez, R.E. Fahey, and A.J. Strauss, *Appl. Phys. Lett.* **48**, 1345 (1986).

4. MICROELECTRONICS

4.1 RAPID, LOW-RESISTANCE INTERCONNECTS BY SELECTIVE TUNGSTEN DEPOSITION ON LASER-DIRECT-WRITTEN POLYSILICON

Polysilicon interconnections were locally deposited on oxide-covered silicon wafers by pyrolysis of silane using a scanned Ar⁺-laser spot. These were reacted subsequently with WF₆ vapor to form a tungsten-silicon composite interconnect by the silicon reduction of WF₆. The conductivity of 0.4-μm-thick polysilicon conductors was enhanced up to 20-fold by formation of a surface tungsten layer having approximately the bulk conductivity value. When this tungsten-silicon composite is applied as interconnect for a 2-μm-design-rule CMOS gate array circuit, a 10-fold improvement in speed is expected due to the conductivity increase. This is the fastest process yet reported for direct-write interconnects with near-metallic conductivity.

Polysilicon interconnect lines¹ were deposited on oxide-coated silicon substrates to serve as a template for the selective tungsten substitution by the reduction² of an ambient WF₆ vapor. In order to facilitate electrical probing of the interconnect structures, special test patterns were fabricated. Regular arrays of probe contact pads (50 μm square) were patterned on silicon wafers which were previously coated with 1 μm of CVD-SiO₂. The pad patterns were formed of aluminum, with an overcoat of p⁺-polysilicon which was furnace annealed to assure good contact. In a SiH₄ ambient atmosphere at 200 Torr the interconnect lines were written by scanning the sample cell in the focus of an optical microscope through which the 488-nm light of an argon-ion laser was directed. Incident laser power was nominally 0.4 to 0.6 W, and the scanning speed of the computer-controlled stage was 2.5 mm/s. The polysilicon lines were approximately 2 μm wide and 400 nm thick. Interconnect lengths ranged from 100 μm up to 2.4 mm. Lines were written as either intrinsic or p⁺-polysilicon, the latter by pyrolysis of a B₂H₆/SiH₄ mixture.

After electrical testing, the interconnect wafers were prepared for the WF₆ treatment by a procedure developed to leave an oxide layer of optimal thickness on the surface of the laser-deposited polysilicon. It has been observed that the latter course of the silicon reduction of WF₆ depends critically on the thickness of the oxide on the sample before the reaction.^{3,4}

The samples were then exposed to a WF₆/Ar ambient at 0.625 Torr total pressure, where the WF₆ comprises 4 percent of the total 350-cm³/min reactor flow. The selective deposition reaction (see Figure 4-1) forms tungsten on silicon by the silicon reduction of WF₆:



In our experiments the temperature was varied from 320°C to 475°C. This reaction occurs selectively on silicon, while either not affecting or slightly etching SiO₂ (see Reference 5). The reaction is self-limiting, as the deposited tungsten acts as a barrier to further WF₆ interaction with the underlying silicon. The reaction time was fixed at 6 min, which is long enough to allow the reaction to go to completion, but too short to obtain significant "tunneling" of W particles⁶ into the bulk of the silicon. The wafers were allowed to cool in the furnace before removal to prevent oxidation of the fresh W layer.

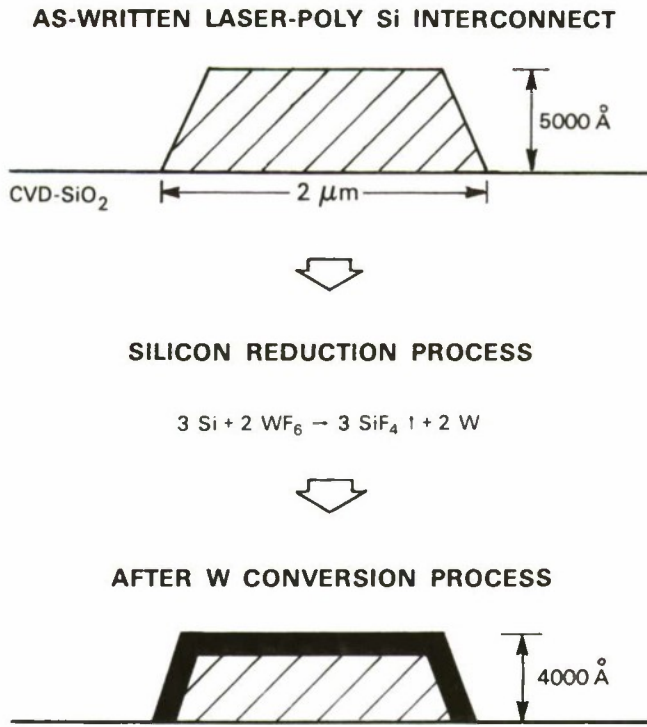


Figure 4-1. Cross-sectional depiction of selective W cladding of laser-written poly-Si by the silicon reduction of WF_6 .

Figure 4-2 shows the resistance reduction factor as a function of reaction temperature; the conductivity of the 0.4- μm -thick interconnects is improved by up to a factor-of-20 because of the silicon reduction reaction. Each point on this figure includes the results of the various interconnect lengths tested, as discussed below. Note that the conductivity enhancement increases to the highest temperature in our study; the presence of Al contact pads does not allow higher reaction temperatures.

Taking the highest of these points ($475^\circ C$), we plot in Figure 4-3 the interconnect resistance before and after the Si reduction reaction, as a function of interconnect length. No intercept shift or nonlinearity is seen in this plot, nor in related plots under different temperatures. In the case of initially undoped polysilicon, the original resistivity is too high to be accurately measured, but the WF_6 -treated lines attain similar conductivities as their p^+ -doped counterparts for comparable line lengths and furnace temperatures. This confirms that the temperature dependence of conductivity improvement obtained by the WF_6 treatment pertains to the effects of that treatment alone, and is not a side effect such as an annealing effect in the original laser-deposited structures.

Rutherford backscattering spectra (RBS) have been taken in order to obtain information on the location and metallurgy of the tungsten and polysilicon layers. This analysis reveals that a top layer contains only tungsten, followed by a gradual transition to a W/Si mixture, becoming

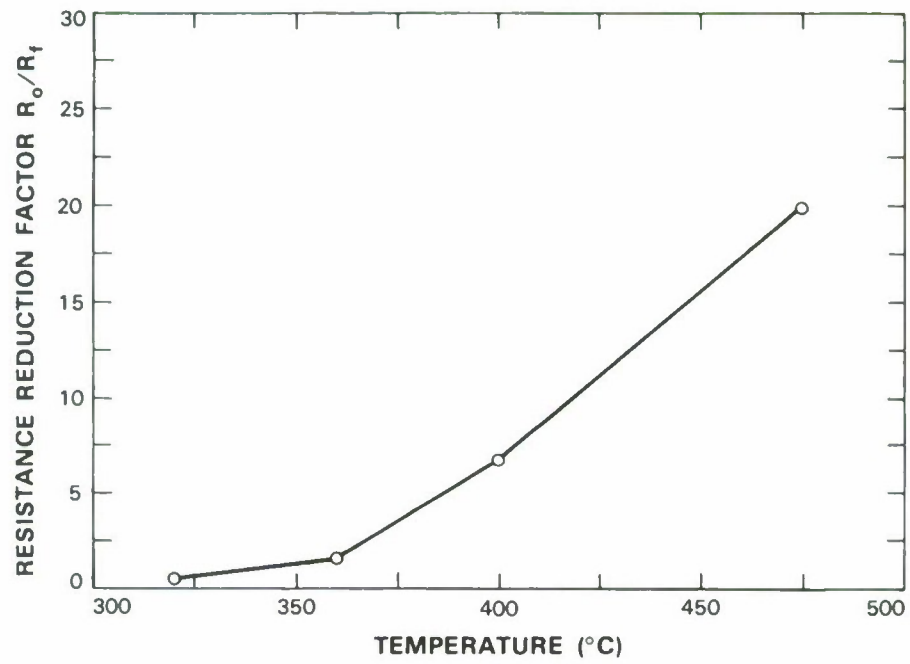


Figure 4-2. Resistance reduction factor R_o/R_f (ratio of original to final resistance) of p^+ laser-written polysilicon interconnects undergoing selective tungsten deposition vs reaction temperature.

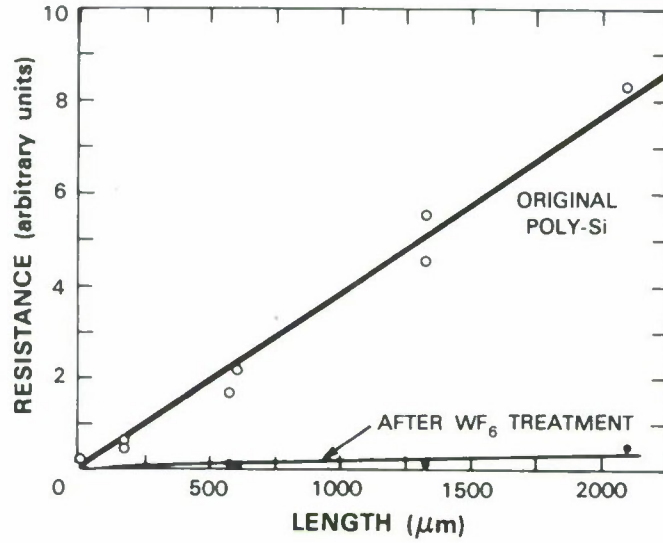


Figure 4-3. Resistance vs length for comparable B-doped laser-direct-written polysilicon interconnects before and after WF_6 treatment at $475^\circ C$.

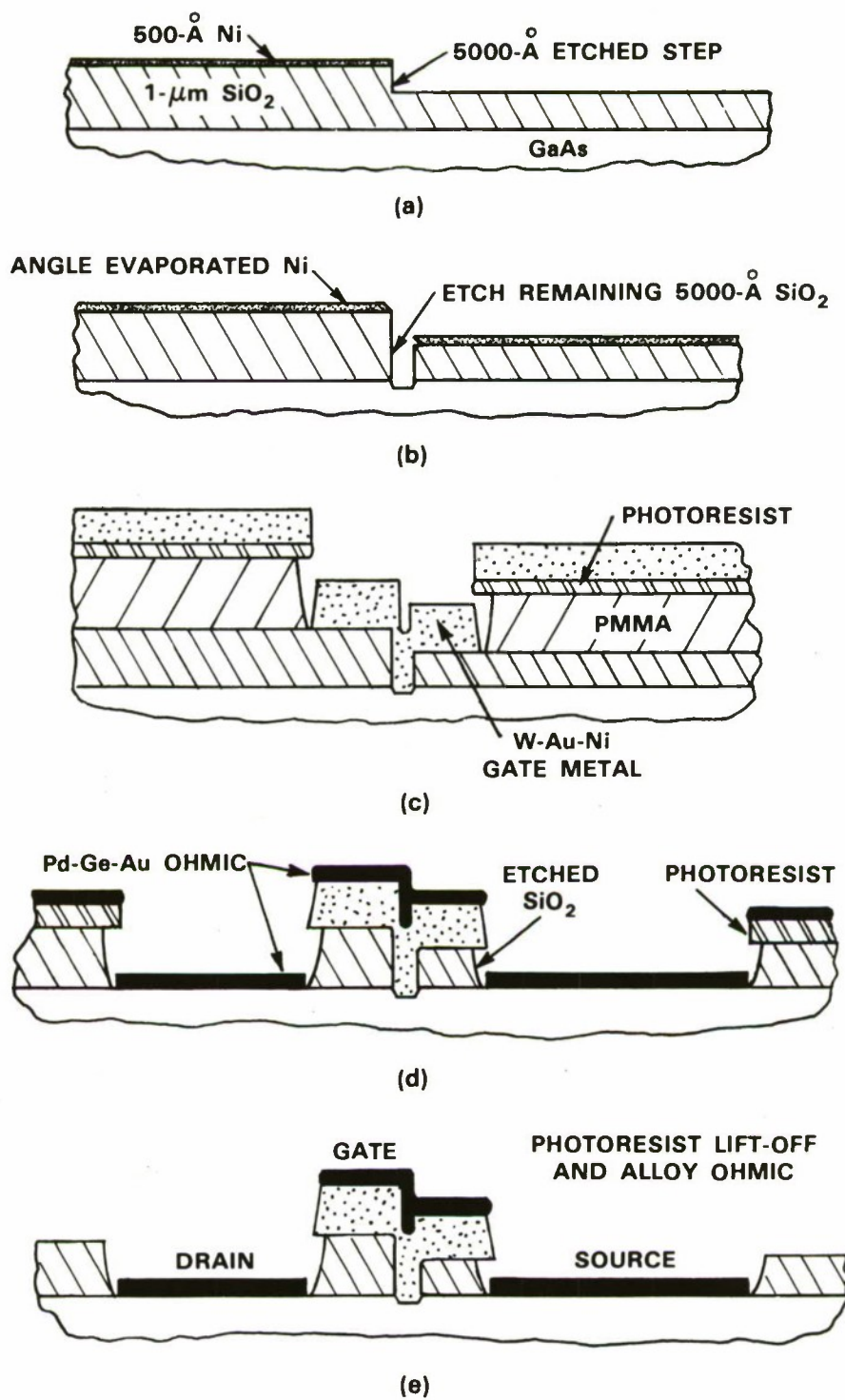


Figure 4-4. Fabrication method for submicrometer-gate-length MESFETs with self-aligned ohmic contacts.

all silicon farther into the sample. No detectable oxygen is observed. These observations were corroborated by Auger electron spectroscopy. In both the RBS and Auger analyses, no tungsten appears in the oxide region away from the laser-polysilicon. Cross-sectional SEM observation of the WF₆-treated laser-written interconnects reveals a distinct interface approximately 100 nm beneath the surface, which corresponds to the thickness of the tungsten layer ascertained by RBS and Auger techniques. This interface is readily observed without the application of staining or preferential etching.

A simple calculation allows one to estimate the bulk resistivity of the new tungsten layer. If the original laser-written p⁺ polysilicon has thickness t_o and resistivity ρ_o , then, after the silicon reduction of WF₆, we consider two layers: a tungsten layer with thickness and resistivity t_w and ρ_w , and the remaining polysilicon with thickness $t_o - 2t_w$. By summing the parallel resistances of these two layers (using our 475°C result from Figure 4-2), we obtain $\rho_o/\rho_w = 78$. Thus with $\rho_o \approx 500 \mu\Omega\text{-cm}$, $\rho_w \approx 6.4 \mu\Omega\text{-cm}$, which is very close to the bulk value of 5.6 $\mu\Omega\text{-cm}$.

This is the fastest process yet reported for direct-write interconnects with near-metallic conductivity. As device dimensions are scaled down, the requirements for greater metallization conductivity become more severe. A simple analysis⁷ demonstrates that, for CMOS gate arrays, the device speed and interconnect delays are comparable factors in determining overall circuit performance in the case of polysilicon (5- μm design rule, 10-mm² chip area). For any significant reduction in device geometry, the interconnect conductivity's contribution becomes more pronounced. For example, a 2- μm -design-rule gate array circuit metallized with polysilicon would be about 10 times slower than with selectively clad tungsten/silicon interconnects. With the combination of rapid (2.5-mm/s) direct writing and the reduction of WF₆, discretionary wiring of prototype gate arrays with tight design rules is feasible.

J.G. Black A.D. Feinerman[†]
D.J. Ehrlich H.H. Busta[‡]
J.H.C. Sedlacek

4.2 SUBMICROMETER-GATE MESFET WITH SELF-ALIGNED OHMIC CONTACTS USING CONVENTIONAL LITHOGRAPHY

The use of conventional lithography to define submicrometer-gate-length MESFETs could be a cost-effective alternative to electron-beam writing. For this reason, we are employing conventional lithography in the fabrication of submicrometer-gate-length MESFETs that are required in a millimeter-wave transceiver module which is presently under development.

The MESFET fabrication sequence is shown in Figure 4-4. The etched step in the SiO₂ layer [Figure 4-4(a)] and shadow evaporation of Ni [Figure 4-4(b)] are used to define the active gate

[†] Department of Physics and Astronomy, Northwestern University, Evanston, IL 60621.

[‡] Gould Research Center, Rolling Meadows, IL 60008.

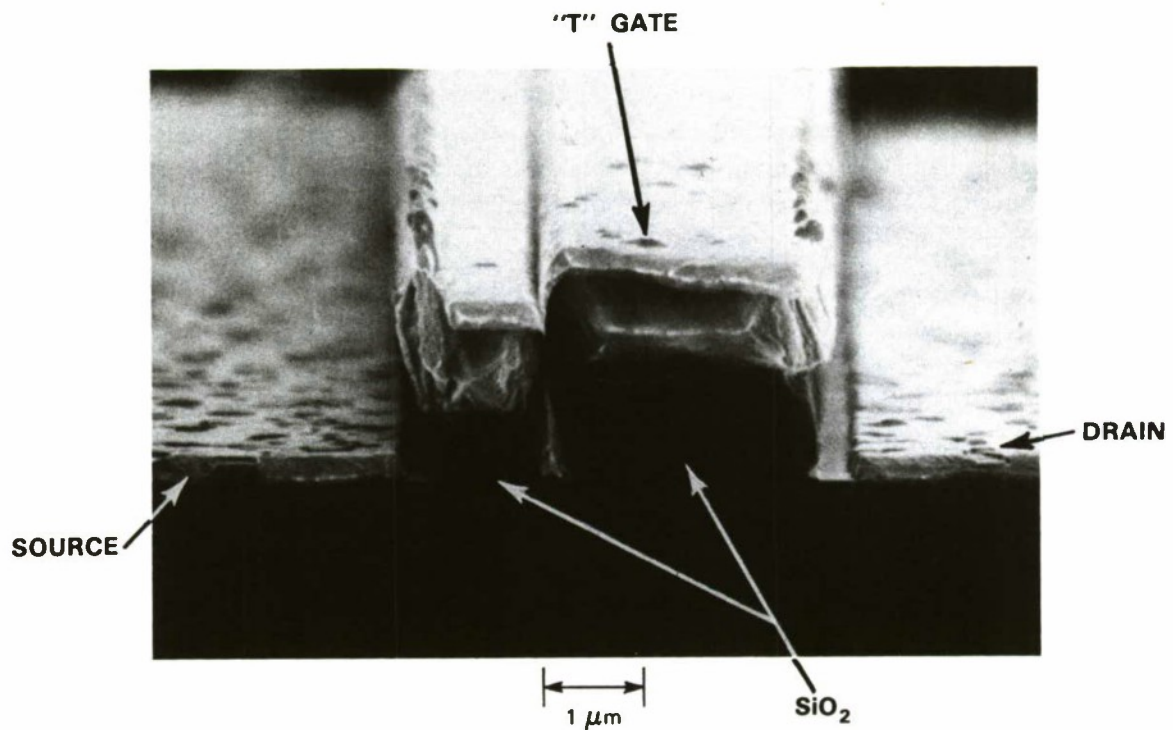


Figure 4-5. Submicrometer "T"-shaped gate with self-aligned ohmic contact.

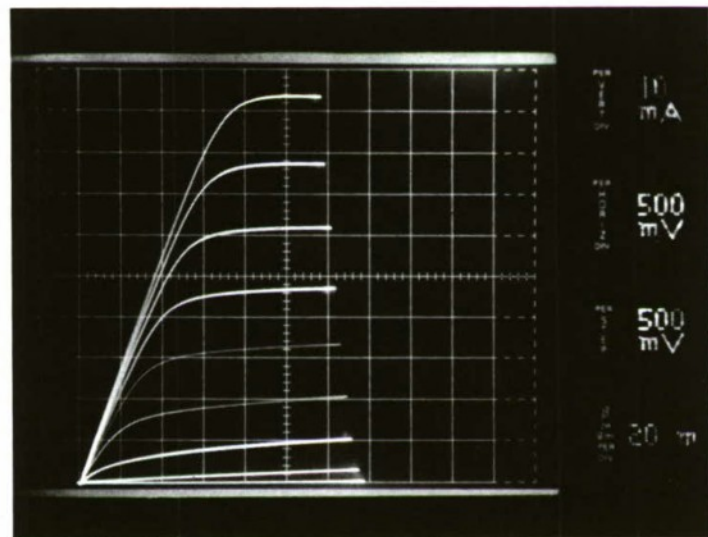


Figure 4-6. DC trace for a $0.5 \times 300\text{-}\mu\text{m}$ gate MESFET.

length. The refractory W/Au Schottky-barrier gate metal is aligned over the exposed GaAs [Figure 4-4(c)] and extends onto the SiO_2 on either side to form a "T"-shaped cross section upon photoresist lift-off. This low-resistance gate configuration also acts to define the source-to-drain spacing during the self-aligned ohmic contact metal deposition [Figure 4-4(d)].

The ohmic contact metallization used is the recently developed Pd-Ge-Au system.⁸ This metallization yields a much smoother topography than Ni-Ge-Au systems, thus reducing the incidence of gate to ohmic short circuits.

The scanning electron micrograph in Figure 4-5 shows the cross section of the gate region of a monolithic power amplifier MESFET fabricated by this method. The gate shown is 0.5 μm in length; however, the same process has been employed to provide longer or shorter gate lengths.

Typical dc characteristics of the MESFET and RF test results of the monolithic power amplifier are shown in Figures 4-6 and 4-7, respectively. The dc trace is for a 300- μm -wide gate section. For the power amplifier at 16 GHz, 6 dB of maximum available gain was measured. The continued development of input and output matching circuits for the amplifier and the device process should increase the gain of this amplifier and make it comparable to devices defined by electron-beam lithography.

L.J. Mahoney C.L. Chen A. Gopinath	D.J. Burrows P.L. Cociani
--	------------------------------

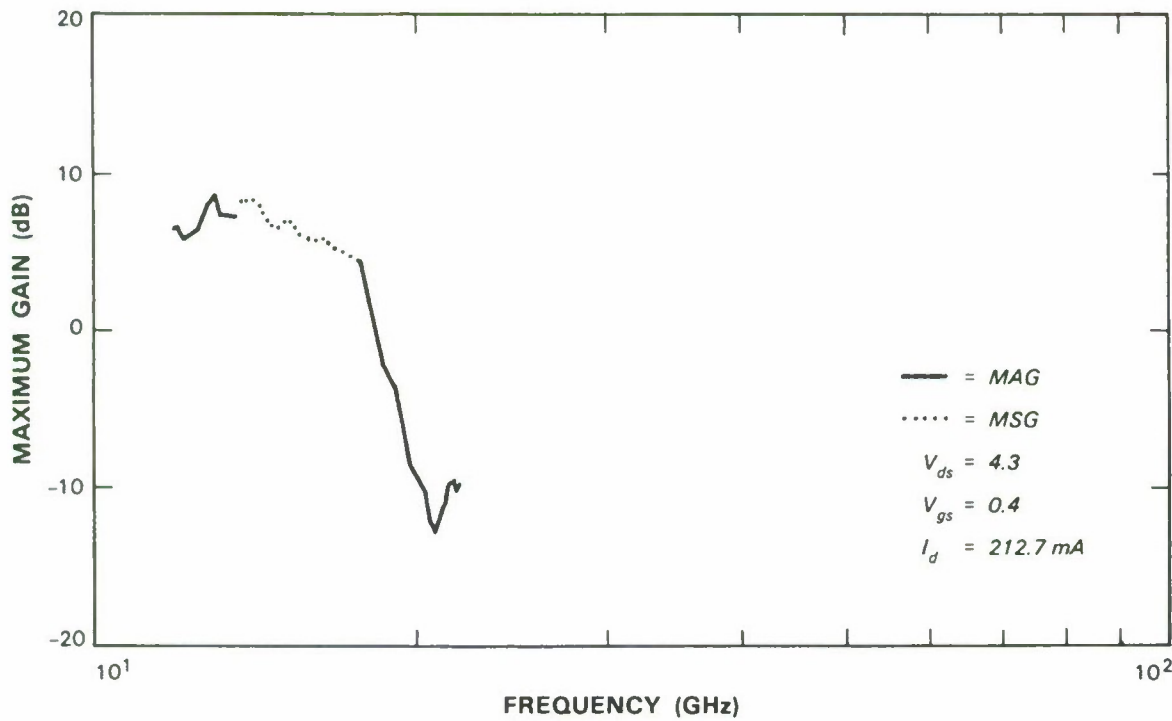


Figure 4-7. A 0.5 \times 600- μm gate MESFET monolithic power amplifier.

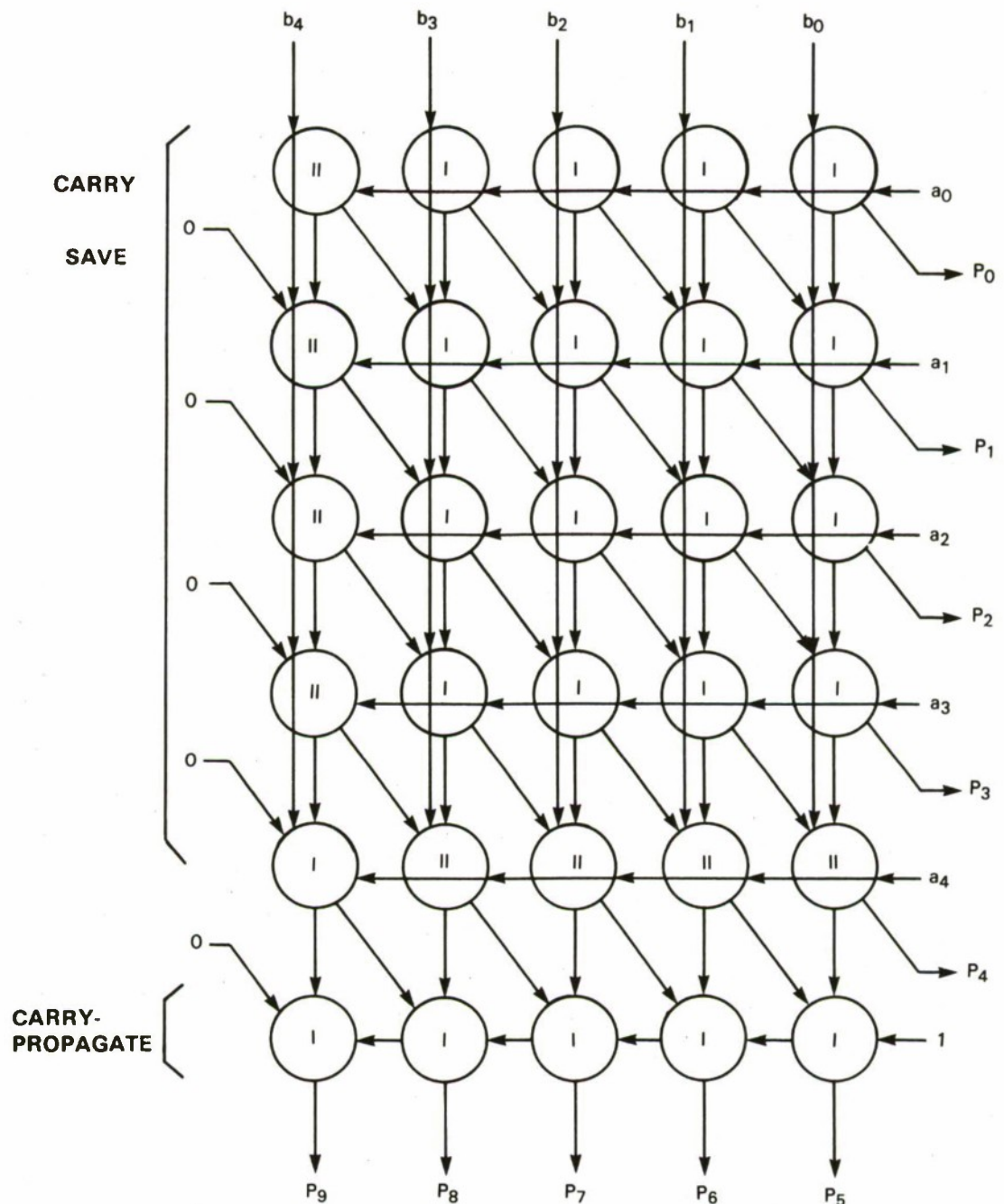


Figure 4-8. A 5×5 Baugh-Wooley array multiplier.

4.3 DESIGN OF AN E-BEAM TESTABLE AND RESTRUCTURABLE ARRAY MULTIPLIER

As the size and complexity of very large scale integration (VLSI) increases, the testability of the circuit becomes challenging and the yield of the circuit decreases. The electron-beam programmable floating gate device is used to increase the the testability and to improve the fault tolerance of a Baugh-Wooley two's-complement array multiplier.⁹ The electron-beam programmable FETs are conventional floating-gate MOS devices that can be programmed using focused electron beams. The p-channel FETs are initially off, but can be programmed to the on-state by using a scanning-electron-beam-lithography system to deposit electrons directly on the floating polysilicon gates.

The Baugh-Wooley two's-complement array multiplier is a very important building block for ALUs and numerous digital signal processing architectures. In two's-complement number system, integer A with $(m + 1)$ bits represents a decimal value of

$$A = -2^m a_m + \sum_{i=0}^{m-1} 2^i a_i .$$

A multiplication of two integers A with $(m + 1)$ bits and B with $(n + 1)$ bits in two's-complement representation is then

$$\begin{aligned} P_{AB} &= A * B \\ &= \left(-2^m a_m + \sum_{i=0}^{m-1} 2^i a_i \right) * \left(-2^n b_n + \sum_{j=0}^{n-1} 2^j b_j \right) \\ &= \left(2^{m+n} a_m b_n + \sum_{i=0}^{m-1} \sum_{j=0}^{n-1} 2^i 2^j a_i b_j - 2^m a_m \sum_{j=0}^{n-1} 2^j b_j - 2^n b_n \sum_{i=0}^{m-1} 2^i a_i \right) . \end{aligned}$$

A straightforward implementation of the above equation will require both addition and subtraction, but it is more convenient to add two's-complement forms for the negative summands

$$2^m a_m \sum_{j=0}^{n-1} 2^j b_j \quad \text{and} \quad 2^n b_n \sum_{i=0}^{m-1} 2^i a_i$$

with appropriate correction terms, which results in the multiplier configuration as shown in Figure 4-8 (see Reference 10). The Type I cells represent the adders with input $a_i b_j$, while the Type II cells represent the adders with input $a_i b_j$. The last carry-propagate row is included because it is necessary to add the carry-outs from the previous row.^{9,10}

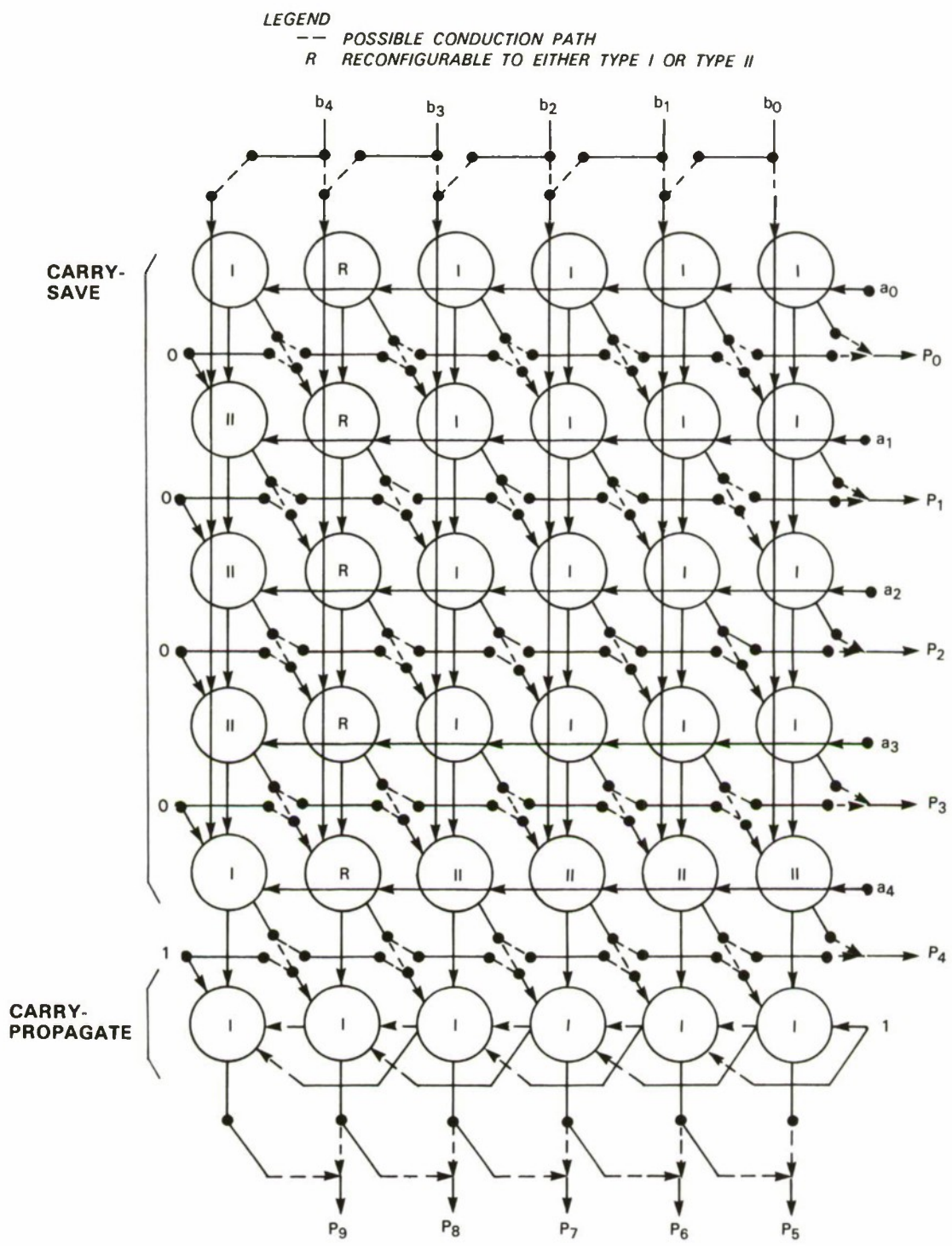


Figure 4-9. Column replacement scheme for an array multiplier.

To achieve a fault-tolerant array multiplier, each multiplier module must be completely tested and any faulty modules must be identified. Then, the faulty modules must be disconnected from the array and replaced using the redundant modules. Given the Baugh-Wooley array multiplier of Figure 4-8, a cell-by-cell replacement is very difficult because of special interconnection requirements that assure the summands to be added correctly. Unlike the memory circuits where each row or column is identical, special information is processed through the interconnections of the multiplier. Therefore, to keep the cell-to-cell relationship, a column replacement of faulty cells is implemented. The column replacement scheme is simpler to implement than row replacement because it requires fewer switches, and it exploits the symmetry of the columns to reduce the need for redundant cells. When a faulty cell is identified, the left column of the array will be redirected, skipping the column containing the faulty cell. Moreover, to have the same input and output terminals regardless of the use of redundant columns, the vertical inputs and outputs are programmable to two adjacent input or output lines. From the cell arrangement shown in Figure 4-8, the two types of cells must be interchangeable. This reconfigurability of the basic cell types can be obtained easily using floating-gate MOS transistors, since the only difference between the two types is that one requires an AND gate while the other requires a NAND gate. The weak point of a column replacement scheme is that a break in the horizontal busses is not correctable. Thus, a conservative design has been employed for any horizontal bus lines, and the number of horizontal busses is minimized. Figure 4-9 shows the restructurable multiplier with one redundant column for a 5×5 array.

To achieve the complete testability of the array multiplier, e-beam programmable flip-flops and e-beam readable output nodes are inserted at different points of the array to access the internal input and output nodes. These use the parasitic diodes present in the regular MOS structures. Several different array multipliers with different testing approaches have been designed in the MOSIS 3- μm scalable CMOS process.

S. Oliver

4.4 PACKAGING JIG FOR WHISKER-CONTACTED, SUBMILLIMETER-WAVE DEVICES

We have designed, built, and tested a small, inexpensive jig for the rapid packaging of whisker-chip diodes and quantum well (QW) devices. It is precise enough to permit whisker contacting of mesa-geometry devices having diameters down to about 1 μm . Either cylindrical or waveguide wafer-geometry cartridges may be assembled, useful to the present limit of waveguide technology of 325 GHz. The jig is small and portable so as to be usable with any nondedicated 160-500X microscope. We are now in a position to interchange QW devices and electromagnetic coupling structures at will; this flexibility is essential for the development of QW oscillators at higher frequencies.

C.D. Parker
E.R. Brown

REFERENCES

1. D.J. Ehrlich, J.Y. Tsao, D.J. Silversmith, J.H.C. Sedlacek, R.W. Mountain, and W.S. Graber, IEEE Electron Device Lett. **EDL-5**, 32 (1984).
2. K.Y. Tsao and H.H. Busta, J. Electrochem. Soc. **131**, 2702 (1984).
3. H.H. Busta and T.H. Tang, "Film Thickness Dependence of Silicon Reduced LPCVD Tungsten on Native Oxide Thickness," Meeting of Electrochemical Society, Toronto, Ontario, Abstract 281, May 1985.
4. E.K. Broadbent and C.L. Ramiller, J. Electrochem. Soc. **131**, 1427 (1984).
5. J.M. Shaw and J.A. Amick, RCA Review **31**, 306 (1970).
6. W.T. Stacy, E.K. Broadbent, and M.H. Norcott, J. Electrochem. Soc. **132**, 444 (1985).
7. S. Sachdev and R. Castellano, Semiconductor International **8**, 306 (1985).
8. C.L. Chen, L.J. Mahoney, M.C. Finn, R.C. Brooks, A. Chu, and J.G. Mavroides, Appl. Phys. Lett. **48**, 535 (1986).
9. K. Hwang, *Computer Arithmetic: Principles, Architecture and Design* (Wiley, New York, 1979).
10. C.E. Hauck *et al.*, "The Systematic Exploration of Pipelined Array Multiplier Performance," VLSI Memo No. 85-218, MIT, Cambridge, MA (January 1985).

5. ANALOG DEVICE TECHNOLOGY

5.1 SUPERCONDUCTIVE ANALOG SIGNAL CORRELATOR

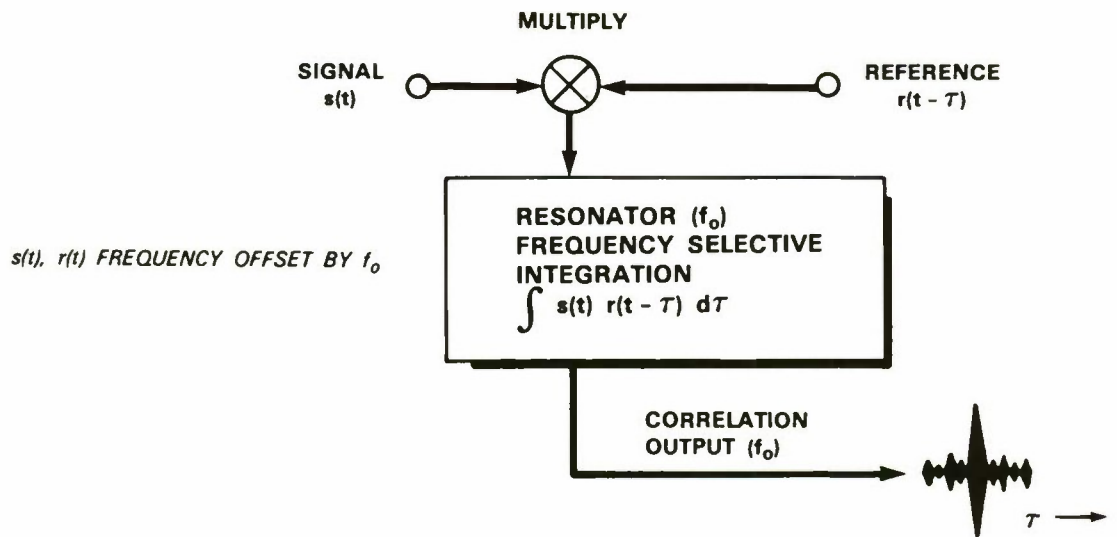
The correlation of wideband analog signals has many applications in advanced communication systems and radar systems. We have designed, fabricated, and tested a wideband time-integrating signal correlator using superconductive integrated components.

The analog time-integrating correlator architecture is shown schematically in Figure 5-1. The correlator takes two time-varying input signals and multiplies them in a mixer. The output of this mixer is then integrated over a fixed period of time (the correlation interval), after which the integrator's content is read out. For the device recently demonstrated, the integration is performed in a high-Q resonator, and the two signal inputs to the correlator are frequency offset by an amount equal to the resonator's center frequency.

Figure 5-2 shows the electrical schematic of the correlator. The mixing of the two signals $s(t)$ and $r(t)$ occurs in the series arrays of SIS tunnel junctions. These junctions are biased to a point near the knee of the quasiparticle I-V characteristic in order to maintain high mixing efficiency. The mixer junctions are $8 \mu\text{m}$ square and are integrated into a series array of 25 junctions in order to provide higher output levels and the relatively high output impedance ($\approx 200 \Omega$) needed to avoid loading the input of the following lumped-element L-C resonator. During the correlation interval, this resonator integrates the product of the two input signals and, for long integration times, must have a large Q. The lumped-element inductor was fabricated out of a superconductive niobium thin film, as was the bottom electrode of the lumped-element capacitor. The capacitor dielectric was formed by electrolytically anodizing the top surface of this bottom electrode to form a 44-nm layer of Nb_2O_5 . Capacitor fabrication was completed by the evaporation of a Pb counterelectrode. The measured Q of 600 for our 20-MHz resonant circuit implies a linear integration time greater than $2 \mu\text{s}$, allowing the processing of analog waveforms with time-bandwidth products in excess of 5000.

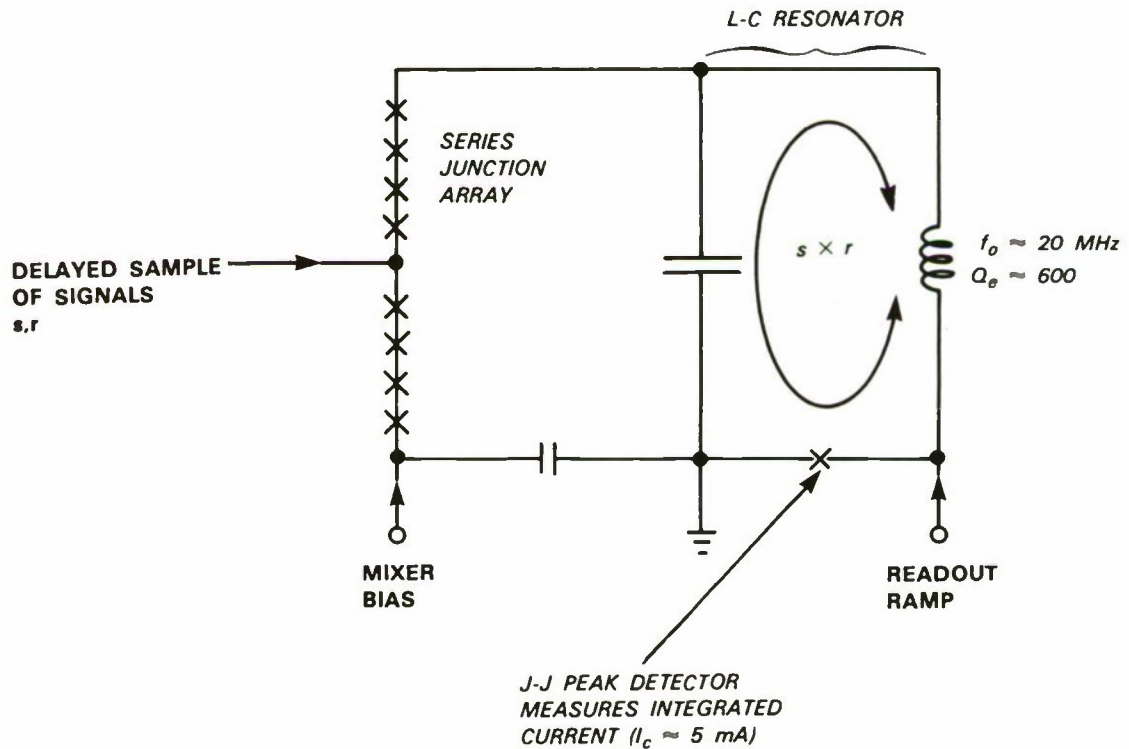
As can be seen in Figure 5-2, there is a large-area tunnel junction embedded in the L-C resonant circuit. This junction functions as a variable-threshold comparator, used for determining the integrator's contents at the end of the integration (correlation) time. This, as well as the mixer junctions in this analog correlator, consists of a $\text{Nb}/\text{Nb}_2\text{O}_5/\text{Pb}$ trilayer. The readout tunnel junction is designed to be $20 \times 80 \mu\text{m}$ with a critical current of 5 mA. Since the readout tunnel junction operates in the zero-voltage state during the integration period, the large critical current of this junction is needed to support the maximum integrated output of the correlator.

In order to detect the integrated signal stored in the high-Q resonator, a linearly increasing current ramp is applied to the Josephson-junction peak detector. When the sum of the oscillating current flowing in the L-C circuit and the instantaneous value of the readout ramp reaches the critical current of the junction, the junction will switch to the voltage state. The instantaneous value of the readout ramp, or the measured time at the moment of switching, is an indication of the magnitude of integrated current stored in the resonator and thus measures the correlation of the two input signals.



75607-44

Figure 5-1. Schematic drawing of single-channel time-integrating correlator.



75607-45

Figure 5-2. Electrical schematic of mixer-integrator peak-detector correlation cell.

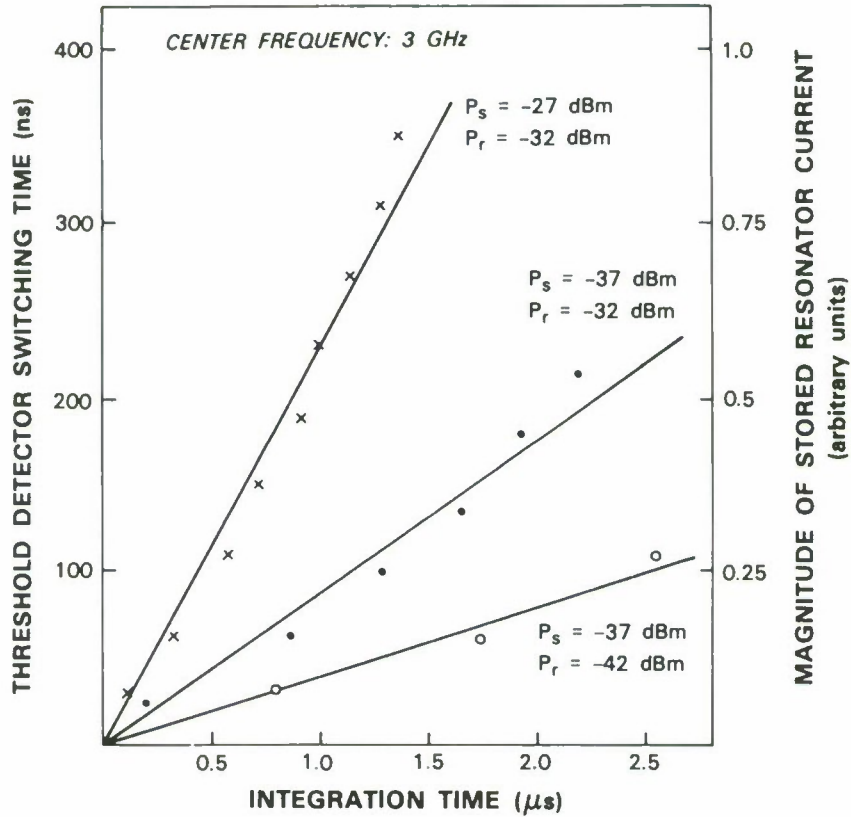


Figure 5-3. Plot of integrated resonator current as a function of input power levels and integration time.

Figure 5-3 shows a plot of the switching time of the Josephson-junction peak detector as a function of the duration of the input signals for different combinations of input power levels. The switching time is measured as an offset from the time the junction would switch if there were no RF signal stored in the L-C resonator. Therefore, an increase in switching time represents an increase in integrated mixer output. As expected, Figure 5-3 reveals a linear dependence of the inferred integrator contents on the integration time. Additionally, we observe a proportional increase in integrator stored energy as the input power to the mixer arrays is increased.

In order to compute the correlation of signal and reference at multiple values of time offset, we are currently fabricating a multi-cell version of this time-integrating correlator incorporating long delay lines and digital output-processing circuits.

J.B. Green
L.N. Smith
A.C. Anderson

S.A. Reible†
R. S. Withers

† MICRILOR, Wakefield, MA.

5.2 BULK-ACOUSTIC-WAVE HOLOGRAPHIC-GRATING RESONATORS

Previous reports¹⁻³ have introduced the concept of holographic-grating acoustic-wave devices that are based upon the interaction of bulk acoustic waves (BAW) with an optically generated hologram in iron-doped lithium niobate (Fe:LiNbO_3). This class of devices holds the potential for realizing wide-bandwidth filters and very high frequency resonators. We project that resonators with fundamental frequencies between 2 and 5 GHz with Q values as large as 10^5 are possible.

Three boules of LiNbO_3 with iron doping concentrations of 0.005, 0.015, and 0.05 percent by weight were grown in order to measure grating reflection coefficients and acoustic propagation loss as a function of iron doping. The results are summarized in Table 5-1. The reflection coefficients were determined by measuring the bulk-acoustic reflection from a uniform grating at the resonant frequency (at which the incident acoustic wavelength is equal to twice the grating period). The data indicate that the reflection coefficient increases monotonically with iron concentration. At 0.05-percent iron doping, the reflection coefficient (2×10^{-4}) is large enough that practical devices can be fabricated. In fact, because of the large number of reflectors in a grating, the overall grating reflection can approach unity.

TABLE 5-1 Characteristics of Bulk-Acoustic Holograms		
Iron Doping (percent)	Grating Element Reflection Coefficient	Propagation Loss at 1 GHz (dB/ μs)
0.005	$<10^{-5}$	<1.0
0.015	10^{-4}	$<1/2$
0.05	2×10^{-4}	<0.7

The values of propagation loss shown in Table 5-1 are very encouraging and are low enough to be acceptable in practical devices. These loss values are upper bounds to the true material loss since they were inferred from the decay in amplitude of an acoustic pulse as it makes multiple passes through the sample. The loss figure obtained by this method includes losses due to misalignment of the front and back faces of the sample, and losses upon reflection from the front and back faces.

An important potential application for holographic-grating acoustic-wave devices is as high-frequency, high-Q resonators for use in stable low-noise signal sources. To demonstrate the achievable Q, we have made single-port resonators with uniform gratings. Figure 5-4 shows the magnitude of the reflected acoustic wave (time-gated so that only a single pass of the crystal is measured) as a function of frequency in a typical experimental device. This was obtained with a

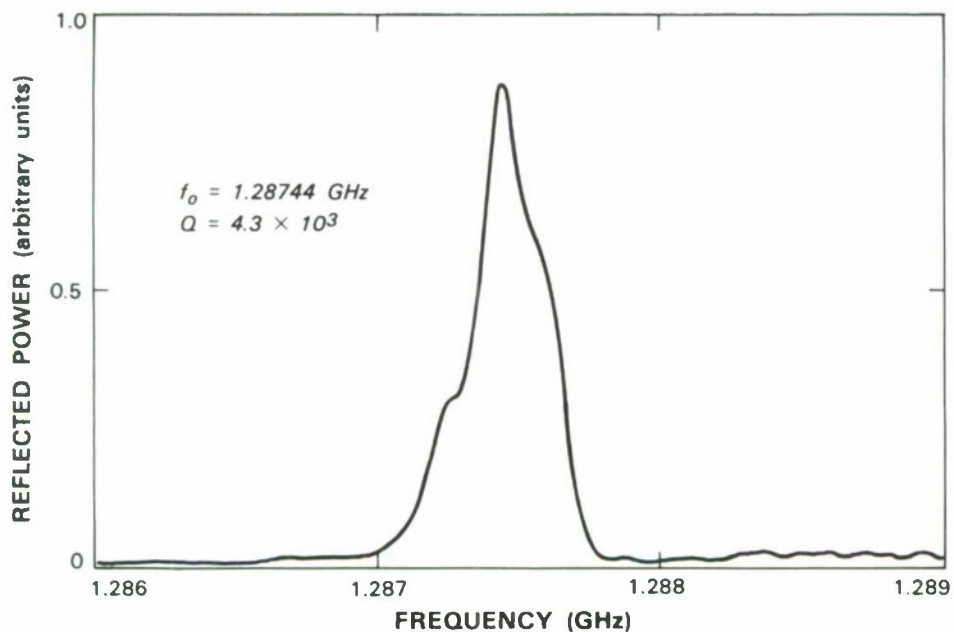


Figure 5-4. Frequency response of holographic acoustic grating.

1.5-in-long piece of 0.05-percent Fe:LiNbO₃. The measured center frequency is $f_0 = 1.29$ GHz and the bandwidth is $\Delta f = 300$ kHz, implying a quality factor $Q = f_0/\Delta f = 4.3 \times 10^3$. The reflection coefficient of the grating was nearly unity. The overall insertion loss, however, is about 50 dB because no attempt has been made to properly match the transducer impedance.

In this single-pass measurement the Q is limited by the length of the grating and the measured value is smaller than that predicted for a grating that fills the sample. Deficiencies in the optical components used to form the two optical beams which interfere to create the hologram caused the grating written into the crystal to be less than 0.5 in long. The observed grating length as measured by the device impulse response is consistent with the measured Q value. The limiting optical component is the beam splitter, and improvements in the optics are under way which will result in longer gratings and higher Q values.

Figure 5-5 shows projected limits to resonator Q values as a function of frequency for two different implementations of the device. The lines which show a Q increasing with frequency represent limits imposed by the device geometry (as for the device of Figure 5-4), while the lines which depict a Q decreasing with frequency represent limits resulting from the inherent material propagation losses which increase as the square of the frequency. Any real device must lie below both lines. Two different values of propagation loss are shown; loss of 0.1 dB/ μ s at 1 GHz is the lowest value reported in the literature for pure LiNbO₃ at room temperature, whereas loss of 1 dB/ μ s at 1 GHz is the approximate upper limit to Fe:LiNbO₃ loss as we have measured it. It should be pointed out also that the loss limits are independent of resonator structure and, thus,

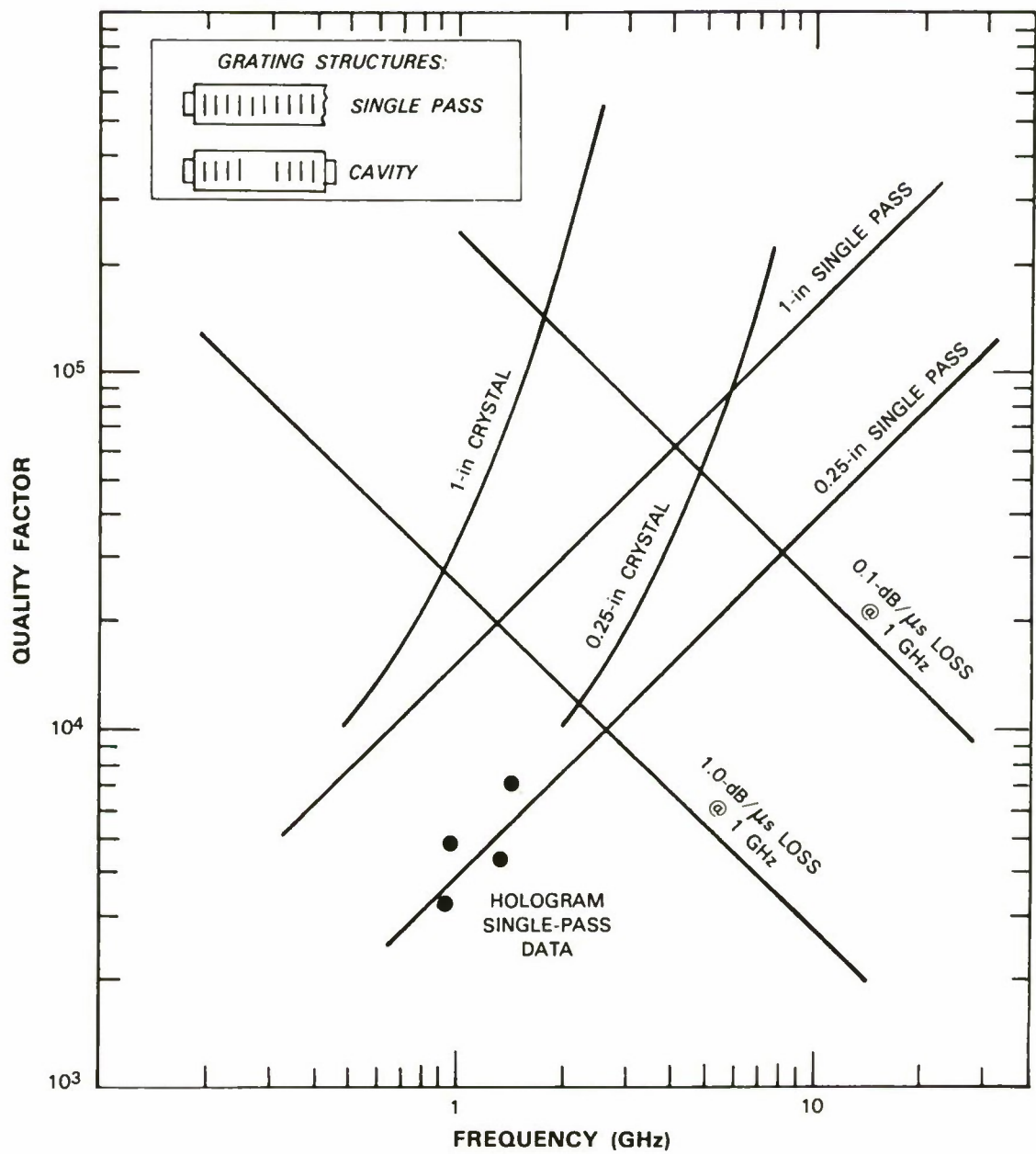


Figure 5-5. Limits on quality factor Q of a holographic acoustic-grating resonator imposed by propagation loss (descending lines), length of grating (for single-pass resonator), and cavity length of resonator (a grating-element reflectivity of 2×10^{-4} was assumed).

75607-48

are a fundamental limit. The figure shows the Q factors for two different structures: a single-port device with weak reflectors, such that the device impulse response is essentially limited to a single acoustic pass; and the two-port cavity resonator structure, similar to that used in SAW resonators, in which two arbitrarily strong gratings enclose a central cavity. The Q of the single-pass device is limited by the number of grating lines which can be placed within the length of the crystal, whereas the cavity device can, with sufficiently strong gratings, effectively confine the acoustic energy for multiple passes of the cavity. Qs are limited by the reflectivity of the gratings and the length (in wavelengths) of the cavity which can be formed in the crystal. Also shown on Figure 5-5 are some of the Q values that we have measured to date, as discussed above. For 1-dB/ μ s loss in a 1-in cavity resonator, the loss limits the Q above approximately 1.3 GHz.

The line established by 0.1-dB/ μ s loss is not a fundamental limit. Acoustic propagation losses can be substantially decreased by cooling the material; e.g., reduction of loss by a factor of nearly 10 has been reported at 2 GHz by cooling to liquid-nitrogen temperatures.⁴

We have successfully demonstrated that high-Q resonators with fundamental frequencies above 1 GHz are possible using holographic-grating bulk-acoustic wave devices. Results to date have been limited by the optics and not the acoustic properties of the devices. Better optics are being installed presently, and we should be able to demonstrate even higher Q factors. We are also making efforts to raise the fundamental operating frequencies to 5 GHz.

D.E. Oates
J.Y. Pan

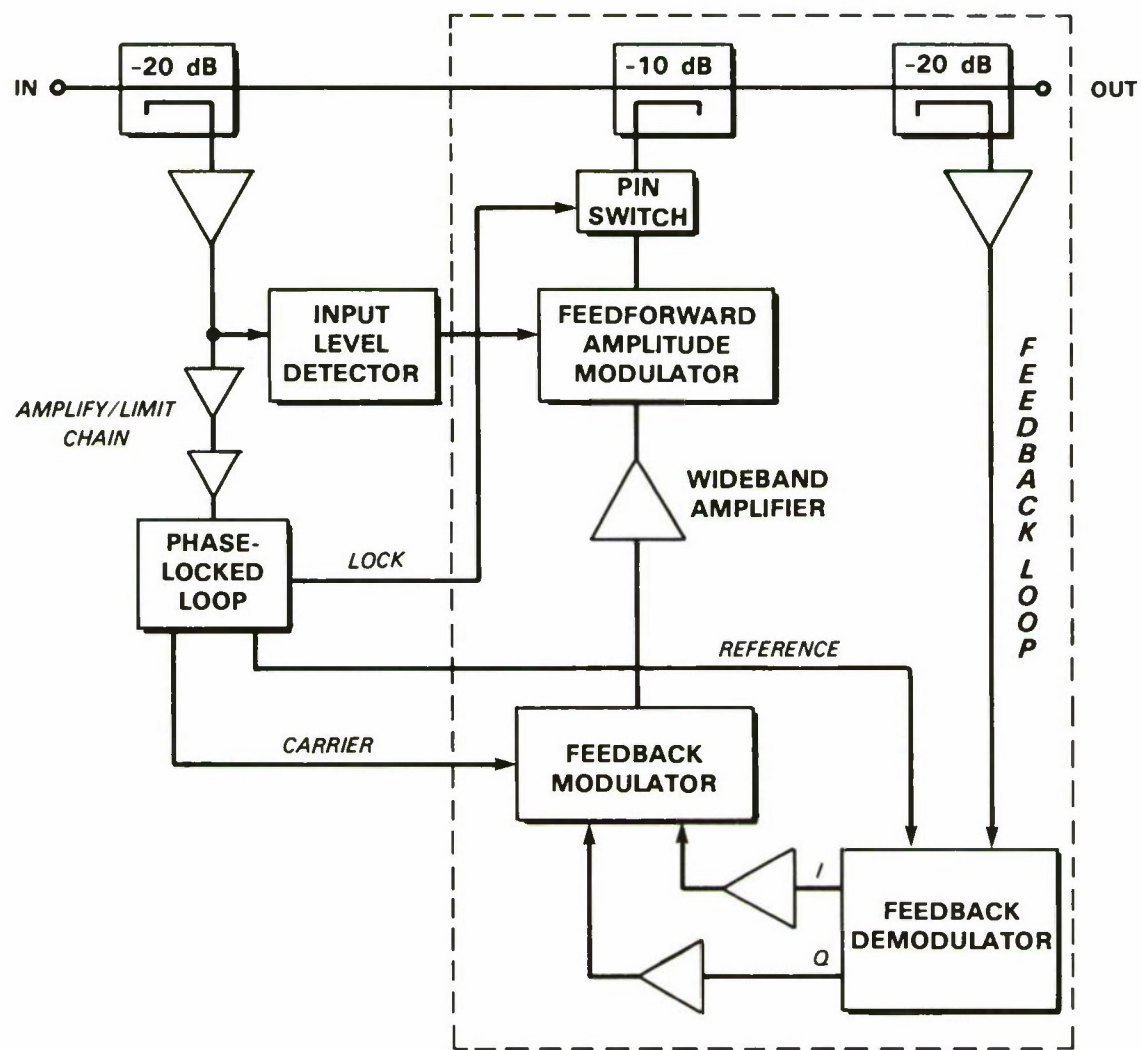
5.3 CANCELER FOR HIGH-LEVEL NARROWBAND INTERFERENCE IN A WIDEBAND CHANNEL

A narrowband canceler system for removal of interference was described previously (see p. 38 in Reference 3) and has since been completed as a functioning unit at the brassboard prototype level. The system, illustrated in the block diagram of Figure 5-6, operates by tracking and regeneration of the interference with a phase-locked loop (PLL). The PLL output is then subtracted from the main channel, thus removing the interference. To achieve 40 dB of cancellation, it is necessary that the replicated signal match the amplitude of the interference to within 0.06 dB and the phase to within 0.4°. To accomplish this, a feedback loop which samples the residue after subtraction is used. The residue is coherently demodulated using the PLL output as the reference, and the resulting in-phase and quadrature components are used to control remodulation of the PLL output so as to drive the residue to zero.

The replicated signal contains some components of narrowband phase noise as well as wideband noise, which become part of the residue after subtraction. The narrowband noise is the PLL phase noise; this is within the bandwidth of the feedback loop and, hence, is reduced by about 10 dB over the raw PLL level. This noise could be reduced further by improvements to the PLL. On the other hand, the wideband noise is generated by the wideband amplifier which follows the feedback modulator, is outside the bandwidth of the loop, and, hence, is not reduced by the feedback. These noise components tend to degrade the overall noise figure of the receiver.

However, in the presence of large interference, the low end of the sensitivity is dominated by the interference residue resulting from errors in the amplitude and phase of the PLL output and not the (enhanced) thermal noise floor. In order to assure that this remains true over the full operating range of the canceler, a first-order open-loop feedforward amplitude modulator (as explained later) minimizes the wideband thermal noise. Further, when the noise level drops below -40 dBm the injected signal is disabled.

As shown in Figure 5-6, a sample of the input is passed through an amplifier/limiter chain to a fast set-on PLL which acts as a narrowband tracking filter for the largest narrowband component. A portion of the signal is coupled off to a detector before limiting to control the feed-forward modulator, which provides a coarse amplitude control so that no more than 6 dB of



76607-49

Figure 5-6. Block diagram of the narrowband canceler.

further attenuation must be provided by the feedback modulator. By placing the bulk of the attenuation after the wideband amplifier, the input level to the amplifier is maximized and the thermal noise added by the amplifier is minimized. (The design complexity of the feedforward modulator could have been avoided if a high-level feedback modulator was available.)

The overall effect of cancellation with feedforward and feedback control is an improvement in signal-to-interference ratio of better than 40 dB at an input interference of +10 dBm, which gradually reduces to 20-dB improvement with an interference level of -40 dBm. Over this range, the residual interference is always significantly higher than the degraded noise floor. Below this level, the circuit is disabled and the chirp-transform exciser⁵ is used to remove any remaining narrowband interference.

Figure 5-7 is a plot of the predicted cancellation ratio vs input interference level based on typical performance characteristics taken from data sheets for the components used in the system. Figure 5-8(a-b) is a spectrum analyzer trace showing the output of the circuit with a +10-dBm input slowly swept from 250 to 350 MHz. Figure 5-8(a) is with the PLL disabled, thus showing the insertion loss, and (b) with the PLL enabled shows a minimum of 40-dB cancellation. The circuit performance is slightly less than that predicted, primarily because of parasitic circuit elements which would be significantly reduced in a packaged design.

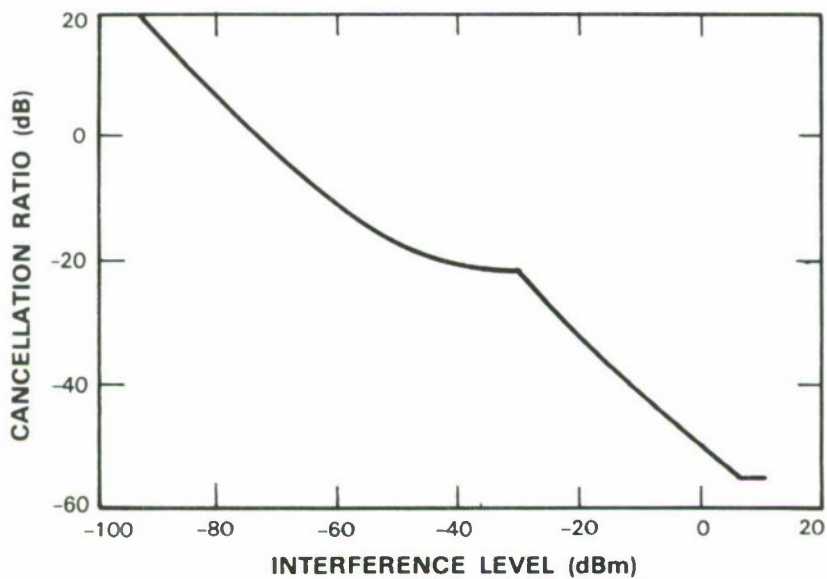


Figure 5-7. Predicted cancellation ratio vs interference level.

Figure 5-9 is an oscilloscope trace of an RF signal in and out of the canceler, which dramatically demonstrates the dynamic performance. The signal is stepped 70 MHz in frequency and

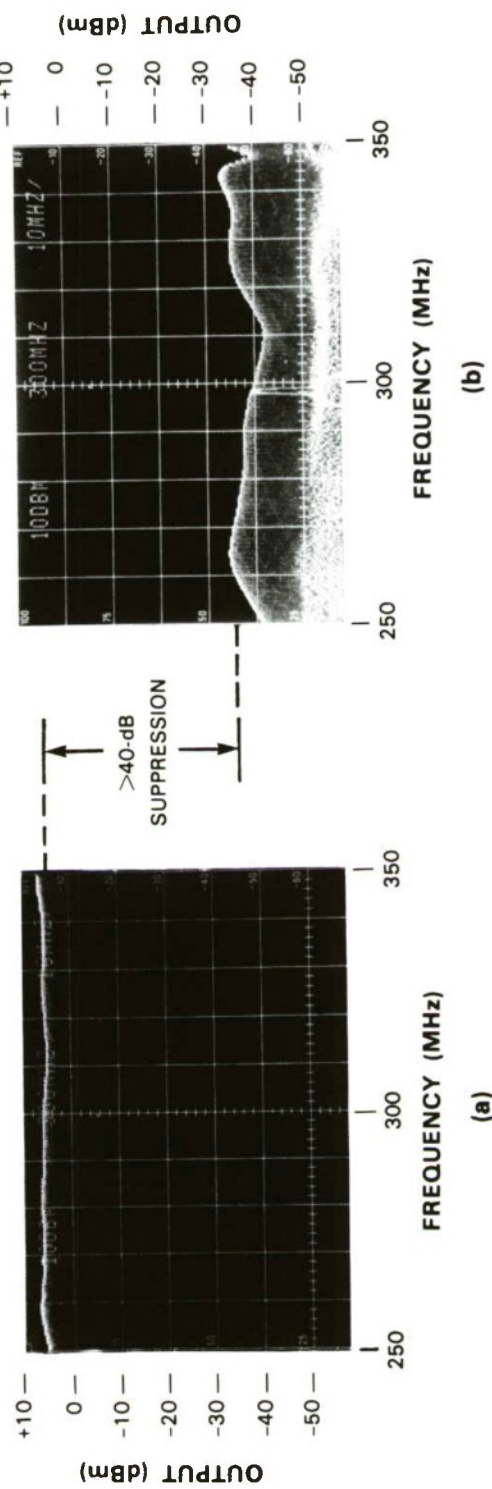


Figure 5-8. Power output of system with a 10-dBm CW input, slowly swept in frequency: (a) cancellation loop disabled; (b) loop enabled.

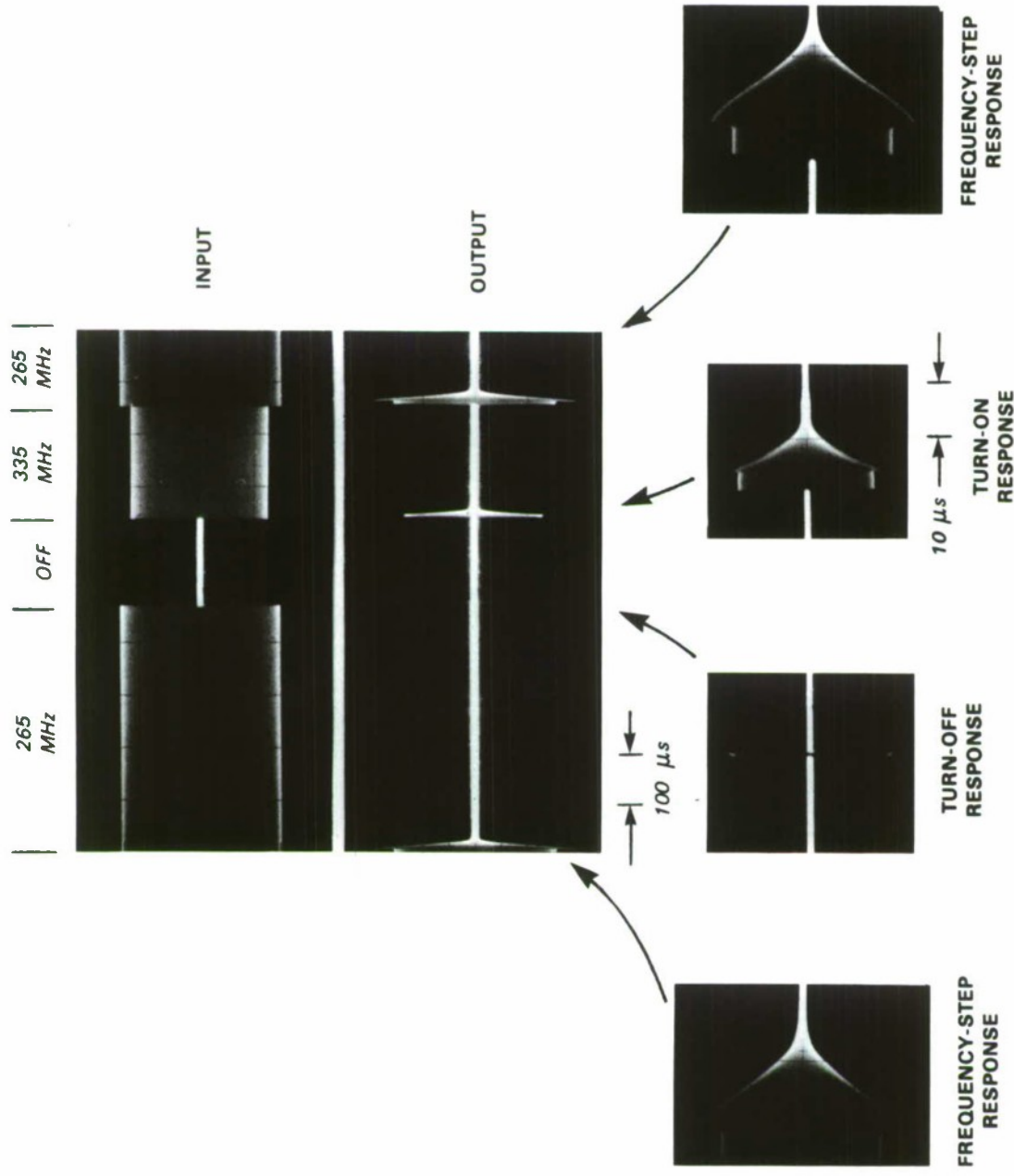


Figure 5-9. Narrowband canceler response to steps in frequency and amplitude (+10-dBm maximum input level).

turned off for a short duration to demonstrate the transient response to both a step in frequency and amplitude. The expanded view of the transients shows that the system settles to 40-dB cancellation in response to transients in both frequency and amplitude in 20 μ s or less, which means it is capable of tracking a frequency hopper.

G.T. Flynn

REFERENCES

1. Solid State Research Report, Lincoln Laboratory, MIT (1984:1), p. 73, DTIC AD-A147429.
2. *Ibid.* (1984:2), p. 68, DTIC AD-A147640.
3. *Ibid.* (1985:3), p. 32.
4. M.I. Grace, R.W. Kedzir, M. Kestigan, and A.B. Smith, *Appl. Phys. Lett.* **9**, 155 (1966).
5. D.R. Arsenault, in *1985 Ultrasonics Symposium Proceedings* (IEEE, New York, 1985), p. 102.

UNCLASSIFIED

SECURITY CLASSIFICATION OF THIS PAGE (When Data Entered)

REPORT DOCUMENTATION PAGE		READ INSTRUCTIONS BEFORE COMPLETING FORM															
1. REPORT NUMBER ESD-TR-86-069	2. GOVT ACCESSION NO.	3. RECIPIENT'S CATALOG NUMBER															
4. TITLE (and Subtitle) Solid State Research		5. TYPE OF REPORT & PERIOD COVERED Quarterly Technical Report 1 February — 30 April 1986															
		6. PERFORMING ORG. REPORT NUMBER 1986:2															
7. AUTHOR(s) Alan L. McWhorter		8. CONTRACT OR GRANT NUMBER(s) F19628-85-C-0002															
9. PERFORMING ORGANIZATION NAME AND ADDRESS Lincoln Laboratory, MIT P.O. Box 73 Lexington, MA 02173-0073		10. PROGRAM ELEMENT, PROJECT, TASK AREA & WORK UNIT NUMBERS Program Element No. 63250F Project No. 649L															
11. CONTROLLING OFFICE NAME AND ADDRESS Air Force Systems Command, USAF Andrews AFB Washington, DC 20331		12. REPORT DATE 15 May 1986															
		13. NUMBER OF PAGES 96															
14. MONITORING AGENCY NAME & ADDRESS (if different from Controlling Office) Electronic Systems Division Hanscom AFB, MA 01731		15. SECURITY CLASS. (of this Report) Unclassified															
		15a. DECLASSIFICATION DOWNGRADING SCHEDULE															
16. DISTRIBUTION STATEMENT (of this Report) Approved for public release; distribution unlimited.																	
17. DISTRIBUTION STATEMENT (of the abstract entered in Block 20, if different from Report)																	
18. SUPPLEMENTARY NOTES None																	
19. KEY WORDS (Continue on reverse side if necessary and identify by block number) <table style="width: 100%; border-collapse: collapse;"> <tr> <td style="width: 33%;">solid state devices</td> <td style="width: 33%;">photodiode devices</td> <td style="width: 33%;">infrared imaging</td> </tr> <tr> <td>quantum electronics</td> <td>lasers</td> <td>surface-wave transducers</td> </tr> <tr> <td>materials research</td> <td>laser spectroscopy</td> <td>charge-coupled devices</td> </tr> <tr> <td>microelectronics</td> <td>imaging arrays</td> <td>acoustoelectric devices</td> </tr> <tr> <td>analog device technology</td> <td>signal processing</td> <td></td> </tr> </table>			solid state devices	photodiode devices	infrared imaging	quantum electronics	lasers	surface-wave transducers	materials research	laser spectroscopy	charge-coupled devices	microelectronics	imaging arrays	acoustoelectric devices	analog device technology	signal processing	
solid state devices	photodiode devices	infrared imaging															
quantum electronics	lasers	surface-wave transducers															
materials research	laser spectroscopy	charge-coupled devices															
microelectronics	imaging arrays	acoustoelectric devices															
analog device technology	signal processing																
20. ABSTRACT (Continue on reverse side if necessary and identify by block number) <p>This report covers in detail the solid state research work of the Solid State Division at Lincoln Laboratory for the period 1 February through 30 April 1986. The topics covered are Solid State Device Research, Quantum Electronics, Materials Research, Microelectronics, and Analog Device Technology. Funding is provided primarily by the Air Force, with additional support provided by the Army, DARPA, Navy, SDIO, NASA, and DOE.</p>																	